**ISTANBUL TECHNICAL UNIVERSITY ★ GRADUATE SCHOOL OF SCIENCE ENGINEERING AND TECHNOLOGY**

# RANDOM FOREST CLASSIFICATION OF TOMATO FIELDS WITH PLANET SATELLITE IMAGE DATA AND ACCURACY ASSESSMENT

**M.Sc. THESIS**

**Betül ŞALLI**

**Department of Geomatics Engineering**

**Geomatics Engineering Programme**

**JULY 2020**

**ISTANBUL TECHNICAL UNIVERSITY ★ GRADUATE SCHOOL OF SCIENCE ENGINEERING AND TECHNOLOGY**

# RANDOM FOREST CLASSIFICATION OF TOMATO FIELDS WITH PLANET SATELLITE IMAGE DATA AND ACCURACY ASSESSMENT

**M.Sc. THESIS**

**Betül ŞALLI**
**(501171608)**

**Department of Geomatics Engineering**

**Geomatics Engineering Programme**

**Thesis Advisor: Prof. Dr. A. Filiz SUNAR**

**JULY 2020**

**İSTANBUL TEKNİK ÜNİVERSİTESİ ★ FEN BİLİMLERİ ENSTİTÜSÜ**

# PLANET UYDU GÖRÜNTÜ VERİLERİYLE YÜKSEK DOĞRULUKLU DOMATES ÜRÜN TİPİ SINIFLANDIRMASINDA RASTGELE ORMAN SINIFLANDIRMA YÖNTEMİNİN KULLANIMI VE DOĞRULUK ANALİZİ

**YÜKSEK LİSANS TEZİ**

**Betül ŞALLI**
**(501171608)**

**Geomatik Mühendisliği Anabilim Dalı**

**Geomatik Mühendisliği Programı**

**Tez Danışmanı: Prof. Dr. A. Filiz SUNAR**

**TEMMUZ 2020**

Betül ŞALLI, a M.Sc. student of ITU Graduate School of Science Engineering and Technology student ID 501171608, successfully defended the thesis entitled "RANDOM FOREST CLASSIFICATION OF TOMATO FIELDS WITH PLANET SATELLITE IMAGE DATA AND ACCURACY ASSESSMENT", which he/she prepared after fulfilling the requirements specified in the associated legislations, before the jury whose signatures are below.

| | | |
|---|---|---|
| **Thesis Advisor :** | **Prof. Dr. A. Filiz SUNAR**<br>Istanbul Technical University | ..... |
| **Jury Members :** | **Prof. Dr. Nebiye MUSAOĞLU**<br>Istanbul Technical University | ..... |
| | **Prof. Dr. Füsun BALIK ŞANLI**<br>Yıldız Technical University | ..... |

**Date of Submission : 15.06.2020**
**Date of Defense : 16.07.2020**

***To my nephew,***

## FOREWORD

This thesis is the final work of my Master study at Istanbul Technical University. The basis of this research withstand our passion for better agriculture. As the population is increasing and the world is moving further in the digital age, there is a higher need to make agriculture more sustainable and productive with emerging technology.

Indeed, I could not have achieved my current level of success without a strong support group. First of all, I would like to thank Professor Filiz Sunar, my supervisor, who supported me with helpful discussions, provided advice with patience, and teaching me how to do high-quality science in a short time. It was an honor for me to have the opportunity to work with her. Secondly, I wish to thank my supportive and pathfinder managers, Tanzer Bilgen and Selim Uçer, and Doktar, due to pave the way for this unique work. Then, I owe a big thank to Batuhan Kavlak, my colleague at Doktar, for his efforts to help me and improve my thesis. It is a great chance for me to work with the Doktar team. I am grateful to my family for their unwavering supports with love, patience, and understanding. I also with great thanks to my friends and colleagues for their hidden but effective supports with lighting up my way.

I would like to thank Tat Gıda, the greatest tomato paste company in Turkey, for providing supports to conduct this work. Finally, I am thankful to Benjamin Trigona-Harany and the Planet team for providing satellite imagery of this research and guiding me on the data.

July 2020

Betül ŞALLI
(Geomatics Engineer)

**TABLE OF CONTENTS**

**Page**

## ABBREVIATIONS

**FAO** : Food and Agriculture Organizations of the United Nations
**RF** : Random Forest
**NDVI** : Normalized Difference Vegetation Index
**ASM** : Angular Second Moment
**MOC2** : Information Measures of Correlation 2
**CV** : Cross-Validation
**GLCM** : Gray Level Co-occurrence Matrix
**EVI** : Enhanced Vegetation Index
**SVM** : Support Vector Machine
**DT** : Decision Tree
**ML** : Maximum Likelihood
**NDWI** : Normalized Difference Water Index
**VI** : Vegetation Index
**ES** : Electromagnetic Spectrum
**IR** : Infrared
**GIS** : Geographic Information Systems
**PS** : PlanetScope
**GSD** : Ground Sampling Distance
**GCP** : Ground Control Point
**DEM** : Digital Elevation Model
**WGS84** : The World Geodetic System 1984
**UTM** : Universal Transverse Mercator
**SR** : Surface Reflectance
**LUT** : Lookup Tables
**6S** : Second Simulation of a Satellite Signal in the Solar Spectrum
**MODIS** : Moderate Resolution Imaging Spectroradiometer
**NRT** : Near-Real-Time
**FLAASH** : Fast Line-of-sight Atmospheric Analysis of Spectral Hypercubes
**NIR** : Near-Infrared
**RVI** : Ratio Vegetation Index
**SAVI** : Soil-Adjusted Vegetation Index
**TVI** : Transformed Vegetation Index
**PVI** : Perpendicular Vegetation Index

## LIST OF TABLES

**Page**

## LIST OF FIGURES

**Page**

## RANDOM FOREST CLASSIFICATION OF TOMATO FIELDS WITH PLANET SATELLITE IMAGE DATA AND ACCURACY ASSESSMENT


### SUMMARY

The importance of agriculture is significant since the foods produced by agriculture are the fundamental source of human and animal life. However, due to the rapidly increasing population growth, reliable and sustainable agricultural planning is required for sufficient production. Otherwise, food wars that will occur with loss of life due to hunger cannot be prevented.

The most effective way to ensure sustainability and reliability in agriculture is to provide developed and emerging technologies to all stakeholders in the agricultural chain and integrate them into each production step. Remote sensing is one of the most suitable technologies that can be integrated into agricultural production. Remote sensing technology, which enables to monitor large areas using imaging sensors, provides a broader perspective to decision-makers by giving them a chance to plan local, regional, and even global production. One of the most important outputs of remote sensing technologies that will contribute to the plans is crop type maps. There are lots of studies in the literature about this topic.

Tomato has a vital role around the world with the amount of fresh consumption and industrial production. Turkey ranks fourth place across the globe at tomato production, according to FAO's (Food and Agriculture Organizations of the United Nations) latest 25-year averages. Its fertile soil and favorable climate with having four seasons are the most significant factors of Turkey's share in the tomato production. Considering both the contributions of remote sensing technology to the agricultural chain and the position of tomato in agricultural production, seasonal tomato cultivation maps with several regional breakdowns are of great importance for production planning and will be an inevitable necessity soon. Despite these requirements, it is challenging to detect tomato plantations with satellite imagery due to the similar spectral signatures of tomato and various horticultural products grown together. Therefore, there are not enough studies in the literature regarding the highly-accurate detection of tomato cultivation areas with satellite data. In this context, this thesis study is a research conducted to make more accurate thematic mapping required in tomato production.

The main purpose of the study is to make highly-accurate tomato cultivation area detection with satellite images. To this end, classifications and accuracy assessments were done with the Planet images, which is one of the world's largest satellite constellations, having high temporal and spatial resolution. The study area was in Karacabey, which is one of the most significant tomato growing regions of Turkey. A total of 18 satellite images were utilized in the study from March to August. Based on the general sowing and harvesting dates of open-field tomato plant growing in Karacabey, the period from the beginning of the sowing to the peak of tomato

plant greenness was taken into consideration. This is the growing period that covers approximately 80% of tomato crops' phenological development. In this period, the attention was paid to the selection of cloudless (not having any atmospheric effects) images. In the classification, Random Forest (RF), which is one of the most preferred methods by many researchers due to its more accurate results, was used. A fieldwork has been conducted to create a training set for the RF classification, which is a supervised machine learning method that can operate lots of DTs (decision trees). The training set includes ten different crops grown in the region during the relevant period. However, in order to increase the classification accuracy, different image features are integrated into the original image dataset as new variables. The features are NDVI (Normalized Difference Vegetation Index), one of the most common vegetation indices and ASM (Angular Second Moment), Entropy, and MOC2 (Information Measures of Correlation 2) GLCM (Gray Level Co-occurrence Matrix) texture parameters. The contributions of features to the classification accuracy were analyzed independently, considering the classification of single and/or different multiple combinations of these features. On the other hand, as well as image features, the use of mono-temporal and multi-temporal satellite images were evaluated in the tomato crop classification. In order to achieve this, single/multiple feature combinations were created and added as variables to both mono-temporal and multi-temporal datasets. Finally, the classification results were compared.

One of the most critical steps in the classification of satellite images is the accuracy assessment. This is because the accuracy assessment gives different results depending on the method chosen and how closely the data used to test accuracy represent the region. Several statistical methods are available in the literature to obtain the most accurate accuracy results with a limited number of available data. In this study, besides the accuracy assessment of the RF classification, the Bootstrapping method was used to determine the reliability of the test data collected by both fieldwork and visual interpretation. This method performs a considerable number of accuracy assessments with different combinations of test data, preventing biased results associated with a single data set and also determining a confidence interval for the obtained accuracy.

On the other hand, collecting precise and reliable data with fieldwork is a challenging, time-consuming, and costly process. Therefore, in this study, if sufficient test data could not be collected, how the tomato classification results would be evaluated and how they would differ in the accuracy assessments made with the test data were analyzed. Based on this, Stratified K-Fold Cross-Validation (CV) was performed with RF classification. The training and test data used before were combined, and a single data set was created. The data set was divided into five equal folds, and the classification was iterated until each fold was used for the test. The classification accuracy was determined by averaging the results of each fold.

When all classification and accuracy assessment results with single/multiple feature combinations of mono-temporal/multi-temporal datasets were examined, it was seen that the combination of NDVI, ASM, and Entropy with multi-temporal 4-band satellite image gave the highest accuracy. On the other hand, it was concluded that the MOC2 texture feature has not contributed to the classification results. For the results of all single/multiple feature combinations, the accuracy of mono-temporal classifications was found to be 10% to 15% lower than multi-temporal classifications.

The accuracy analysis results showed that the reliability of the test data used was most likely within the 5% confidence interval. Finally, it is emphasized in the results section that the CV method is reliable and can be used when there is no test data because it has been found that the same combination of data and features gives the highest accuracy even if there is not enough test data.

# PLANET UYDU GÖRÜNTÜ VERİLERİYLE YÜKSEK DOĞRULUKLU DOMATES ÜRÜN TİPİ SINIFLANDIRMASINDA RASTGELE ORMAN SINIFLANDIRMA YÖNTEMİNİN KULLANIMI VE DOĞRULUK ANALİZİ

## ÖZET

Günümüzde, insan ve hayvan yaşamının devamlılığı tarımla üretilen besinlerle sağlandığından tarımın önemi son derecede büyüktür. Ancak hızla artan nüfus artışı nedeniyle, yeterli üretimin yapılabilmesi için doğru ve sürdürülebilir tarım planlamasına gereksinim vardır. Aksi halde açlık sebebiyle yaşanabilecek can kayıplarının beraberinde ortaya çıkacak gıda savaşlarının önüne geçilemez.

Tarımda sürdürülebilirliği sağlamanın en etkili yolu, gelişen ve gelişmekte olan teknolojileri, tarımsal üretim sürecindeki tüm paydaşlara ve her bir aşamaya entegre etmektir. Uzaktan algılama, tarımsal üretime entegre edilebilecek en uygun teknolojilerden biridir. Tek seferde görüntü alımı ile oldukça geniş alanların izlenmesine imkan sağlayan bu teknoloji, lokal, bölgesel ve hatta küresel ölçekte üretim planlamasını mümkün kılarak karar vericilere daha geniş bir perspektif sunar. Uzaktan algılama teknolojilerinin bu planlamalara katkı sağlayacak en önemli çıktılarından biri ürün deseni haritalarıdır. Bunun için literatürde birçok çalışma mevcuttur. Özellikle hasattan önce elde edilen bölge bazlı ürün tipi haritaları ile ilgili ürünlere ait üretim durumu belirlenerek pazar hakimiyeti sağlanabilir, piyasadaki fiyat dalgalanmalarının önüne geçilebilir ve fabrikaların sezon sonu kapasiteleri için bir öngörü elde edilebilir. Bununla birlikte bakanlıklar ve tarımsal sigorta şirketleri için beyan kontrolü sağlanarak güven ortamı oluşturulabilir ve haksız uygulamaların önüne geçilebilir.

Dünya genelinde domates, sofralık tüketim ve endüstriyel üretimde önemli bir paya sahiptir. Türkiye ise FAO'nun (Gıda ve Tarım Örgütü) son 25 yıllık ortalamalarına göre dünya genelindeki domates üretiminde Çin, Amerika ve Hindistan'dan sonra dördüncü sıradadır. Dört mevsimi yaşayan elverişli iklimi ve verimli toprak yapısı, Türkiye'nin domates üretimindeki bu payının en önemli etkenidir. Hem uzaktan algılama teknolojisinin tarım zincirine katkıları hem de domatesin tarımsal üretimdeki payı düşünüldüğünde, farklı bölge kırılımlarında sezonluk domates ekim alanlarının tespitiyle oluşturulan ürün deseni haritaları, üretim planlamaları için büyük bir öneme sahiptir ve yakın gelecekte bu teknoloji kaçınılmaz bir gereklilik olacaktır. Bu gerekliliğe karşın domates bitkisinin aynı bölgelerde yetiştiği çeşitli meyve ve sebzelerle gösterdiği benzer spektral özellikler, uydu görüntüleri ile tespitini zorlaştırmaktadır. Bu nedenle literatürde, uydu görüntüleri ile yüksek doğruluklu domates ekim alanı tespiti konusunda yeterli sayıda çalışma yoktur. Farklı iklim ve toprak yapısına sahip bölgelerde otomatik/yarı otomatik çalışabilecek ürün tipi sınıflandırma algoritmalarının geliştirilmesine ihtiyaç vardır. Geliştirilebilecek yöntemlerin özellikle domates bitkisi için de yüksek doğruluklu sonuç vermesi

önemlidir. Bunun için öncelikle domates bitkisinin tespit edilebileceği en uygun veri setleri ile bunların kombinasyonları değerlendirilmeli, yersel çalışmalardan elde edilen veriler ile en uygun sınıflandırma algoritması belirlenmelidir. Bu bağlamda bu tez çalışması, domates üretiminde ihtiyaç duyulan daha doğruluklu tematik harita üretimine yönelik yapılmış olan bir araştırma çalışmasıdır.

Çalışmanın temel amacı, uydu görüntüleri ile yüksek doğruluklu domates ekim alanlarının tespitinin yapılmasıdır. Bu amaçla, Türkiye'nin domates yetiştiriciliğinde en önemli bölgelerinden biri olan Karacabey'de, dünyanın en büyük uydu takımlarından biri olan Planet'in yüksek zamansal ve mekansal çözünürlüklü görüntüleri kullanılarak sınıflandırma ve doğruluk değerlendirmesi yapılmıştır. Türkiye'de açık tarla domates üretiminin yapıldığı başlıca bölgeler Bursa, Balıkesir, Manisa ve İzmir'dir. Bursa, domates içerikli işlenmiş ürünlerin üretildiği fabrikalara ev sahipliği yaptığından Türkiye için stratejik bir konumdadır. Karacabey ise Mustafakemalpaşa Ovası ile birlikte Bursa'daki önemli tarımsal üretim bölgelerinden biridir ve bu sebeple çalışma alanı olarak tercih edilmiştir. Diğer yandan yörüngedeki birçok uydusu nedeniyle bitkilerin fenolojik gelişmelerini bilgi kaybı olmadan izlenmesine olanak sağlayan Planet uydu görüntüleri, günümüz tarımsal çalışmalarda ön plana çıkmaya başlamıştır. Aynı zamanda mekansal çözünürlüğü de tarımsal alanların izlenmesi ve takibi için uygundur. Çalışmada Mart ayından Ağustos ayına kadar toplamda 18 uydu görüntüsü göz önüne alınmıştır. Açık alanda yetiştirilen domates bitkisinin Karacabey'deki genel ekim ve hasat tarihleri baz alınarak, ekim öncesinden bitki yeşilliğinin en yoğun olduğu evrenin sonuna kadarki dönem, yani domatesin fenolojik gelişim sürecinin yaklaşık %80'ini kapsayan gelişme periyodu dikkate alınmıştır. Bu tarih aralığında bulutsuz (atmosferik etki içermeyen) görüntülerin seçimine dikkat edilmiştir. Sınıflandırmada günümüzde çoğu araştırmacı tarafından daha doğruluklu sonuçlar vermesi nedeniyle tercih edilen Rastgele Orman yöntemi kullanılmıştır. Kontrollü bir makine öğrenmesi yöntemi olan Rastgele Orman uygulaması için yersel çalışma yapılarak eğitim veri seti oluşturulmuştur. Eğitim veri seti, bölgede ilgili dönemde yetişen on farklı ürünü içermektedir. Bununla birlikte sınıflandırma doğruluğunu arttırmak amacıyla farklı görüntü özellikleri birer değişken olarak orjinal görüntü veri setine eklenmiştir. Bu özellikler, en yaygın bitki indekslerinden biri olan NDVI ile ASM, Entropy ve MOC2 GLCM doku parametreleridir. NDVI, genel olarak biyokütlenin miktarı ve durumu hakkında bilgi veren spektral bir indekstir. Farklı ürün cinslerinin spektral özelliklerine bağlı olarak indeks değerleri değiştiğinden, NDVI'ın ürün tipi sınıflandırmalarında sıklıkla tercih edilmektedir. Bunun yanı sıra GLCM doku parametrelerinden biri olan ASM, homojenliğin ve tekdüzeliğin ölçüsüdür. Homojen bölgelerde ASM değeri yüksektir. Diğer bir doku olan Entropy ise rastgelelik hakkında bilgi sağlar ve görüntüdeki özelliklerin karmaşıklık durumunu belirler. Son olarak MOC2, korelasyonun ölçüsüdür. Yani dağılım fonksiyonundaki ilişkileri değerlendirerek dokunun karmaşıklığını ve ilgili bölgeden elde edilen bilginin bağımlılığını ölçer. Çalışmada kullanılacak doku özelliklerinin belirlenmesi için öncelikle görüntü veri setindeki 18 görüntüde 13 farklı özellik hesaplanmıştır. Eğitim veri setindeki her bir poligon için içerdiği tüm piksellerin doku değerlerinin ortalaması alınmış, böylece poligon başına ortalama doku değerleri belirlenmiştir. Ardından eğitim setindeki ürünlere ait tüm poligonların doku değerlerinin ortalaması alınarak her bir ürün için bir doku değeri hesaplanmıştır. Son olarak her ürün için tüm tarihlerde hesaplanan doku değerleri, doku değeri-zaman grafiğinde gösterilerek, ürünlerin 13 özellik için zamansal değişimleri karşılaştırılmıştır. Bölgedeki on ürünün zaman

içerisinde farklı davranışlar gösterdiği üç özellik belirlenmiş, böylece sınıflandırmaya katkı sağlayabilecek özellikler birer değişken olarak çalışmaya dahil edilmiştir. Aynı zamanda bu özelliklerin tekli ve farklı çoklu kombinasyonları sınıflandırmada göz önüne alınarak, sınıflandırma doğruluğuna olan katkıları ayrı ayrı irdelenmiştir. Diğer yandan domates ekim alanlarının tespitinde görüntü özelliklerinin yanı sıra, tek-zamanlı ve çok-zamanlı uydu görüntülerinin kullanımı da değerlendirilmiştir. Literatürde çeşitli ürünler için farklı veri setleri ile yapılmış çalışmalar mevcuttur. Bu çalışmalarda tek-zamanlı ve çok-zamanlı verilerin kullanıldığı görülmüş, domates ürün sınıflandırması için en uygun olanın belirlenmesi amacıyla her iki veri setiyle de sınıflandırma yapılmıştır. Bunun için birer değişken olarak eklenen görüntü özellikleri ile oluşturulan tekli/çoklu parametre kombinasyonları, hem tek-zamanlı hem de çok-zamanlı veri setlerine uygulanarak, sınıflandırma sonuçları karşılaştırılmıştır. Tek-zamanlı sınıflandırma için 30 Haziran 2019 tarihli görüntü kullanılmıştır. Bu tarihin seçiminde, çalışmada kullanılan üç doku özelliğinin zamansal grafiklerinden yararlanılmıştır. Bunun için domates ile diğer ürünlerin, özellikle en benzer spektral özelliklere sahip olan biber, karpuz ve mısır bitkilerinin farklı değerlere sahip olduğu tarihler belirlenmiş, en yüksek farkın gözlendiği en uygun fenolojik tarih seçilmiştir.

Uydu görüntülerinin sınıflandırılmasındaki en önemli aşamalardan biri de doğruluk değerlendirmesidir. Bu ise, seçilen yönteme ve doğruluğun test edilmesinde kullanılan verilerin bölgeyi ne kadar gerçeğe yakın temsil ettiğine bağlı olarak doğruluk değerlendirmesinin farklı sonuçlar vermesinden kaynaklanmaktadır. Sınırlı sayıdaki mevcut veri ile gerçeğe en yakın doğruluk sonucunu elde edebilmek için literatürde çeşitli istatistiksel yöntemler mevcuttur. Bu çalışmada, Rastgele Orman sınıflandırmasının doğruluk değerlendirmesinin yanı sıra hem yersel çalışma hem de görsel yorumlama ile toplanan test verilerinin güvenilirliğini belirlemek için Önyükleme (Bootstrapping) yöntemi tercih edilmiştir. Bu yöntem, çok sayıda doğruluk değerlendirmesini test verisinin farklı kombinasyonları ile yaparak, tek bir veri setine bağlı yanlı sonuçların oluşmasını önler ve aynı zamanda elde edilen doğruluk için bir güven aralığı belirler. Önyükleme yöntemi, test verisini dikkate alır ve yalnızca doğruluk değerlendirmesinde kullanılarak sınıflandırma modelinin çalışmasında etki etmez. Bu çalışmada bu yönem için alt örneklem sayısı test veri setinin sayısına eşit ve tekrar sayısı 1000 olarak alınmıştır.

Diğer yandan yersel çalışma ile doğru ve güvenilir veri toplamak zorlu, zaman alıcı ve maliyetli bir süreçtir. Bu yüzden bu çalışmada, yeterli sayıda test verisi toplanamadığı durumda elde edilecek domates ürün sınıflandırması sonuçlarının nasıl değerlendirileceği ve yeterli test verisi olduğu durumda elde edilen doğruluk sonuçlarıyla ne kadar fark göstereceği ortaya konmuştur. Bunun için Katmanlı K-Katlamalı Çaprak Değerlendirmeli (Stratified K-Fold Cross-Validation) Rastgele Orman sınıflandırması yapılmıştır. Çapraz Değerlendirme, istatistikte yaygın olarak kullanılan bir yöntemdir ve farklı çeşitleri mevcuttur. Bu çalışmadaki veri setinin her bir üründen farklı sayıda poligon verisi içermesi sebebiyle orantılı bir dağılım yapılması, yani modelin herhangi bir sınıfa fazla veya az ağırlık verilmesini önlemek için Çapraz Değerlendirme'nin Katmanlı K-Katlamalı alt yöntemi seçilmiştir. Uygulamada, başlangıçta kullanılan eğitim ve test verileri birleştirilerek tek bir veri seti oluşturulmuş, bu veri seti beş eşit parçaya bölünerek her bir parça, test için kullanılana kadar sınıflandırma tekrar edilmiştir. Beş sınıflandırmanın doğruluk değerlendirme sonuçlarının ortalaması alınarak sınıflandırma doğruluğu belirlenmiştir.

Tek zamanlı/çok zamanlı veri setlerinin tekli/çoklu parametre kombinasyonları ile yapılan tüm sınıflandırma ve doğruluk değerlendirmesi sonuçlarına bakıldığında, çok-zamanlı 4-bantlı uydu görüntülerine NDVI, ASM ve Entropy özelliklerinin eklendiği kombinasyonun en yüksek doğruluğu verdiği görülmüştür. Diğer yandan MOC2 doku özelliğinin sınıflandırmaya katkısının olmadığı saptanmıştır. Tüm tekli/çoklu kombinasyonlar için yapılan doğruluk değerlendirmelerinde, tek-zamanlı sınıflandırmaların doğruluğu, çok-zamanlı sınıflandırmalardan %10 ila %15 daha düşük bulunmuştur. Doğruluk analizi sonuçları ile kullanılan test verisi güvenilirliğinin, en yüksek ihtimalle %5 güven aralığı içerisinde olduğu görülmüştür. Son olarak, yeterli test verisi olmadığında da aynı veri seti ve değişken kombinasyonunun doğruluğu yüksek bulunduğundan, Çapraz Değerlendirme yönteminin güvenilir olduğu ve test verisi olmadığında da kullanılabileceği sonuçlar bölümünde vurgulanmıştır.

# 1. INTRODUCTION

Remote sensing technology allows us to monitor what is happening on Earth and what has changed over time. Taking advantage of this, many kinds of research are available so far, and new researches with advanced algorithms and tools are being developed to tackle more complex topics. Agriculture is one of the significant industries having complex issues waiting to be overcome. This sector is important because food is one of the primary sources of life for animals and humans. Therefore, it is imperative to ensure food safety and sustainability in parallel with significant population growth.

Cereals and horticultural products are the leaders of food consumption. Tomato is one of the most widely consumed horticultural products around the world as it can be consumed as fresh, dried, and processed. The growing demand for processed tomato products (e.g., tomato paste, ketchup, sauce) around the world offers resource-rich countries to sell their products to resource-poor countries [1]. Turkey has a favorable climate and soil structure for tomato cultivation. Therefore, it is a resource-rich country for tomato-based products but needs optimization in production processes to raise its position in the global market. To meet this requirement, decision-makers and stakeholders should make the right decisions. Also, price volatility in the industry should be reduced. Hence satellite images can be integrated into the food industry to meet these needs. Using satellite data, it is possible to monitor the total amount of cultivation, estimate the yield, and monitor harvesting activities in agricultural areas. However, the information is not valuable unless the remotely sensed data is fast, dynamic, and real-time.

With the developing technologies, satellite constellations have emerged that provide daily images today. However, there are still limitations to monitor crop status. For example, using only remote sensed data, it is still difficult to estimate yield or determine the product type with high accuracy, and besides, it may not be applied to all product types. However, obtaining accurate and reliable field data is the most significant challenge due to its cost. In order to overcome, advanced machine learning

algorithms are adapted to the classification applications with the advantage of their learning capabilities from limited field data. In addition to the limitations in the field data, the use of mono-temporal images to differentiate vegetable crops will not yield satisfactory results due to spectral similarities. In this context, the use of multi-temporal images for time series analysis is becoming popular to distinguish vegetative plants from their phenological behavior.

Due to the high demand for fresh foods, some studies have been conducted in the literature on this subject. However, since there are still limitations on remote sensing in agricultural applications, the number of studies on fresh foods (e.g., vegetables, fruits) is less than cereals (e.g., wheat, barley, rice). In order to examine the above limitations and shortcomings in the literature, this study was carried out using a machine-learning algorithm (Random Forests) in the detection of tomato cultivated areas. The effectiveness of image features such as texture or features extracted by NDVI (Normalized Difference Vegetation Index) was also evaluated, and comparisons of the use of mono- and multi-temporal satellite image datasets were outlined.

## 1.1 Purpose of Thesis

Accurate crop type detection from remote sensing imagery is valuable for decision-makers to understand the dynamics in the agricultural industry, manage agricultural practices, and ensure food security and sustainability. Due to the reason for being a challenging task, there are not many significant studies on the detection of tomato cultivated fields by using only the satellite imagery in the literature yet. Based on this gap, this study aimed to;

- map tomato cultivation parcels with desired accuracy,
- prove the importance of fieldwork on precise classification results,
- evaluate the necessity of test data,
- compare mono- and multi-temporal image classification approaches,
- analyze the efficiency of multi-temporal image classification,
- examine the effectiveness of various spectral and textural features,

- determine the best-performed features and indices for tomato field classification,
- assess the performance of RF (Random Forest), a widespread machine-learning classification method,
- demonstrate the advantages of affordable and high spatio-temporal resolution PS (PlanetScope) CubeSat Constellation.

## 1.2 Literature Review

There are lots of studies about crop type classification in the literature. Some used machine-learning-based algorithms, while others addressed the importance of spectral and textural features, and they achieved satisfactory results. There are also some studies, specifically on mapping tomato parcels. This section provides brief information about these studies.

In the study performed by Vaglio Laurin et al., (2018), the early mapping of planted tomato parcels (before harvest) was done. This study was carried out for seven different locations in Italy using the ML (Maximum Likelihood) Supervised classification algorithm. In the classification step, train and test sets were selected using field surveys and Sentinel-2 satellite images. Aerial photographs were used in a visual analysis to validate and improve classification accuracies. In general, higher than 80% of both producer's and user's accuracies were obtained. This study indicated that the accuracy of early tomato cultivated field estimations are mainly related to the crop type heterogeneity of a region, and agricultural practices used by farmers [2].

Ok, Akar, Gungor, (2012) studied to compare the performances of RF and ML classifications based on both pixel- and parcel-based approaches using mono-temporal SPOT-5 image (10m, four bands) for crop type mapping. The study area used covers agricultural (i.e., corn, tomato, pepper, wheat, sugar beet, and rice) parcels on an area about 95 km2 located in Bursa-Karacabey region, Turkey. Field boundaries were extracted from 1:5000 cadastral maps and used for the object-based classification. Due to similar spectral characteristics of tomato and pepper, these classes were mixed and therefore taken as a mixed class named "Tomato/Pepper" class. This study showed that the highest overall accuracy (85,89%) obtained in the parcel-based RF Classification [3].

The performance of the RF classification algorithm was evaluated by Tatsumi, Yamashiki, Torres, Taipe, (2015) using a four-year Landsat 7 ETM+ time-series. The monthly time series of Enhanced Vegetation Index (EVI) variables (e.g., mean, mode, min, diversity) were integrated into the classification process and evaluated. Eight crops, including alfalfa, asparagus, avocado, cotton, grape, corn, mango, and tomato, were classified, and 81% of the overall accuracy was achieved in the crop classification. Cotton had the highest producer accuracy, with 98%, while the lowest accuracy was obtained from tomato and avocado. The results showed that two variables (mode and sum) of EVI time series data increased accuracy. Besides, although the number of variables has little effect, it has been demonstrated that the number of training data has a significant impact on RF classification [4].

Hao et.al., (2015) performed NDVI time-series based crop type classification with single- and hybrid-classifiers and compared the results. In the analysis, cotton, grape, wheat, watermelon, corn, and tomato crops were taken into consideration. Multiple-voting (M-voting) and probabilistic fusion (P-fusion) were selected for hybrid classification, RF, Support Vector Machine (SVM), and See 5 (C 5.0) were preferred for single classification. When the classification results were compared using both pixel- and object-based samples, it was demonstrated that object-based samples do not significantly improve the accuracy but provide better visual results. It was also revealed that the increase in the number of samples significantly increase the accuracy of all classifiers [5].

In contrast, hybrid classifiers performed better when the sample size was low. However, when large number of samples were used, single classifiers have also been found to give quite accurate results.

Conrad et al., (2014) studied on per-field crop mapping over heterogeneous agricultural regions in West-Uzbekistan. This study aimed to detect the optimum number of images (as acquisition dates and windows) for better classification accuracy. In this way, 9 RapidEye (6.5 m, five bands) mosaics of the area were classified into nine classes using the RF algorithm, and 85.7% of overall accuracy was achieved. As a result, the selection of the optimum image dates for winter to summer transition period has been shown to increase mapping accuracy [6].

The applicability of pre-harvest classification with satisfactory accuracies was tested by Maponya, Van Niekerk, Mashimbye, (2020). Five machine-learning-based classification algorithms, namely SVM, DT (Decision Tree), k-Nearest Neighbor, RF, and ML were performed using Sentinel-2 time-series. Spectral bands, vegetation indices, principal components, and texture features were integrated into the classification. Four experiments with different image combinations were performed to test machine-learning-based algorithms. The results were evaluated with ground truth data, and it was revealed that pre-harvest classification could be obtained with reasonable accuracies. Also, SVM and RF showed the highest accuracy among the five machine-learning-based classification algorithms. Finally, it was emphasized by the authors that image selection is not required for the automatic classification procedure, since it is satisfactory to use all images from the beginning of the season to the pre-harvest, without image selection [7].

Inglada et al., (2015) aimed to evaluate the performance of different machine-learning-based classification algorithms in crop type mapping. RF, SVM, DT, and gradient boosted trees were evaluated by applying to SPOT-4 (20m, four bands) and Landsat-8 (30m, 11 bands) time series in 12 different regions worldwide. RF revealed the highest accuracy results among the four algorithms. NDVI, NDWI (Normalized Difference Water Index), and brightness were found as the best performing features [8].

Balasubramanian, (2017) conducted a research to identify the most essential spectral and textural features in crop-type mapping. Various feature selection algorithms were used to classify a particular crop using Worldview-2 (0.46m, eight bands) images. Single and multi-date classification results were compared for each crop. Corn, millet, peanut, sorghum, and cotton are classified to create single crop maps. In this study, the combination of features selected by Fisher's and Multiple-Kernel-Learning algorithms with the SVM classification method showed the highest classification accuracy for five different crops. As a result, the GLCM (Gray Level Co-occurrence Matrix) textures of VIs (vegetation index) were the essential textures for single crop type mapping. Besides, the multi-date classification increased the overall accuracy for millet and cotton by 4% but did not significantly affect other crops. Overall accuracy for various plant species ranged from 77 to 90% [9].

Gallaun et al., (2015) proposed a two-stage sampling methodology to accurately estimate the changed areas and to evaluate its accuracy. For this purpose, they used Bootstrapping method. In other words, it is aimed to reveal accuracy uncertainty and confidence intervals with Bootstrapping. In the study, it has been shown that Bootstrapping can be preferred to obtain confidence intervals without using the complex assumptions of the normal distribution. Additionally, the importance and the necessity of confidence intervals for area reporting were highlighted [10].

# 2. REMOTE SENSING TECHNOLOGY

## 2.1 Remote Sensing

Remote Sensing is the acquisition of information about the Earth without being in physical contact. The sensing is done with images obtained by recording energy that is reflected or emitted from the surface in one or more regions of the ES (electromagnetic spectrum) [11]. The term "Remote Sensing" was first used by Evelyn Pruitt from the United States Marine Research Office in the 1950s [12]. Gaspard Felix Tournachon's photographing Paris from balloons in 1859 is considered the beginning of remote sensing [13]. For the first time during World War I, mounting cameras on aircraft and using aerial photographs for various purposes can be considered as an essential step in the development of remote sensing technology. Finally, the World War II photographs taken from rockets mounted cameras can be seen as the beginning of space-based remote sensing [12].

Today, with the wealth of data obtained from remote sensing sensors, it is possible to observe the current situation of the entire Earth and to decide on the future by extracting information from the images [14]. For example, weather and hazard prediction, monitoring of erupting volcanoes, and dust storms are possible using remote sensing technology and based on this information; a decision-maker can take precautions for natural disasters. Also, mapping large forest fires, monitoring urban growth, and changes in agricultural areas are other examples of common remote sensing applications [15].

Remote sensing technology provides several significant advantages. Satellite imagery allows up-to-date information over large areas without having to be there. It is also possible to monitor areas that are inaccessible or difficult to visit. Satellite data offers global and regional observations at a glance. On digital platforms, analysis and interpretations are possible for a simultaneously captured image or a series of images covering a specified period. Also, providing a recurring coverage area enables

regions to be monitored and changes to be observed over time. Various spatial, spectral, radiometric, and temporal resolutions offer data selection for different purposes. Due to having several spectral bands of remotely sensed imageries, different band combinations reveal the information which could not be possible to discern with human eyes.

There are two types of sensors in remote sensing technology [16]. Active sensors provide their source of illumination and record the magnitude of energy reflected or emitted from the target. Passive sensors use sunlight as an illumination source and record the energy reflected or emitted from the target in different regions of the ES [14]. The fundamental process of passive remote sensing occurs between incident radiation coming from the Sun and the target (Figure 2.1) [17].

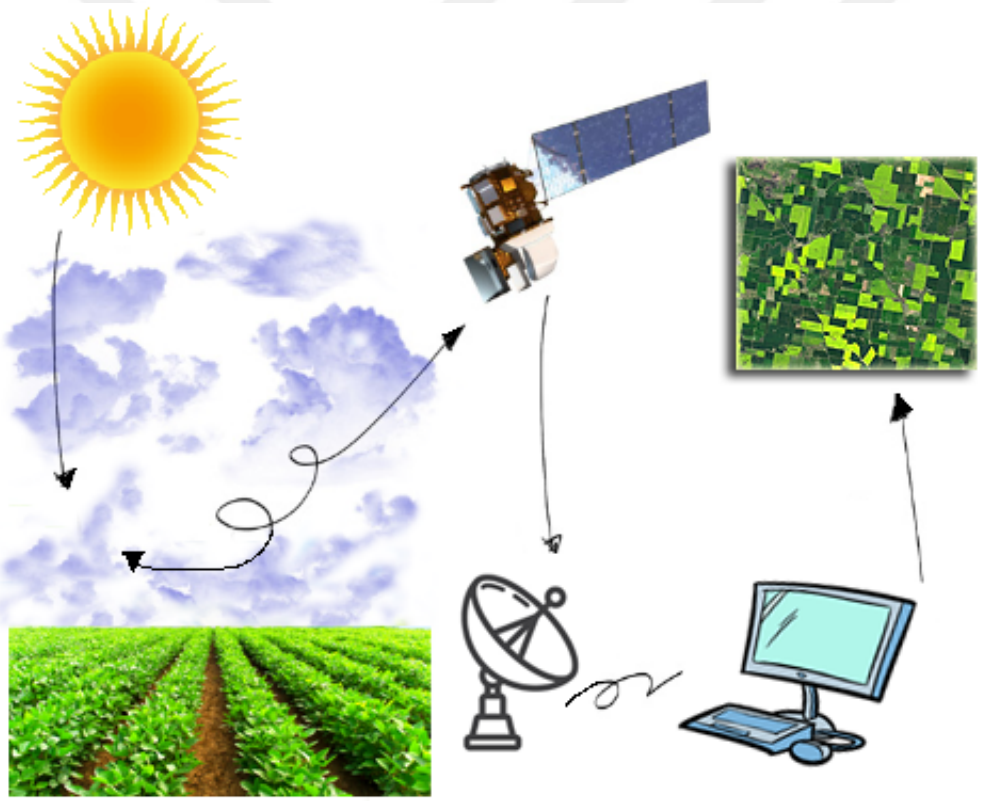

**Figure 2.1 :** Passive remote sensing procedure.

## 2.2 Electromagnetic Spectrum (ES)

Electromagnetic radiation is coming from the Sun and illuminating the Earth [18]. Radiation is called electromagnetic because it consists of both electrical and magnetic waves [12]. These electromagnetic waves involve ES. ES includes regions from short

wavelengths (high frequency, high energy) to long wavelengths (low frequency, low energy). Wavelength and frequency intervals of each region are shown in Figure 2.2.

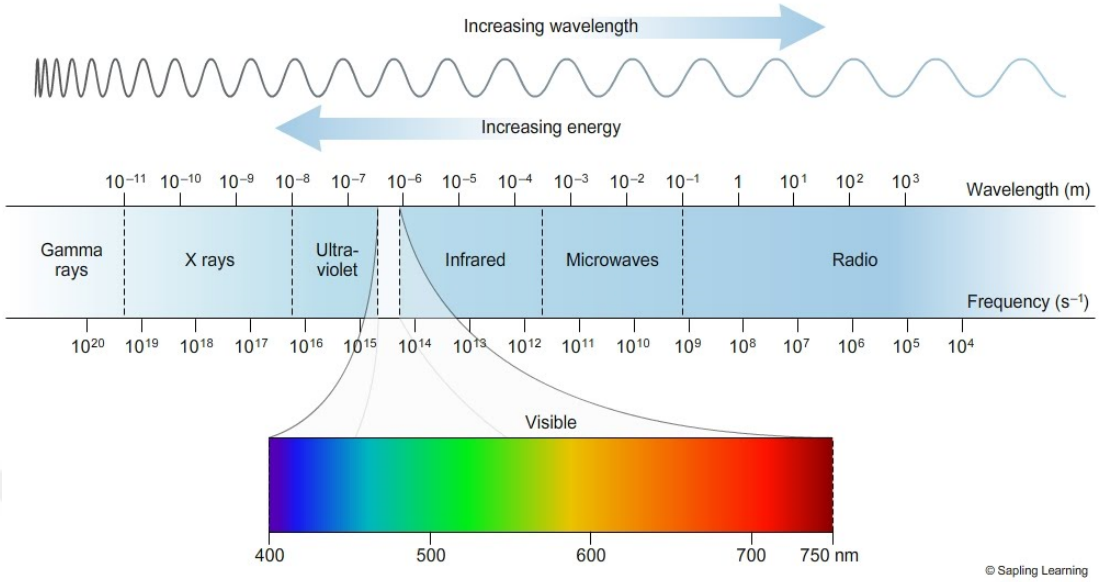


**Figure 2.2 :** Regions of the ES [19].

Human eyes can detect visible light, which is a small portion of the entire ES [17]. However, the peak values of solar radiation come up with the visible portion of ES [18]. Even though the remaining regions are invisible for human eyes, these are useful for remote sensing applications and provide valuable information for Earth.

Passive sensors are generally used for radiation coming from visible and infrared (IR) portions, active sensors for microwaves. The IR region can be divided into two categories, which are reflected in IR and thermal IR. In the first category, sensors acquire the radiation reflected from the target. In the second category, sensors acquire the radiation re-emitted from the target [17]. IR radiation is crucial due to revealing the distinctive properties of Earth objects.

## 2.3 Atmospheric Interactions

Energy is travelling in the atmosphere before reaching the target and the sensor. While travelling, incoming light is affected by the particles and gases in the atmosphere [18]. These atmospheric interactions called scattering and absorption (Figure 2.3).

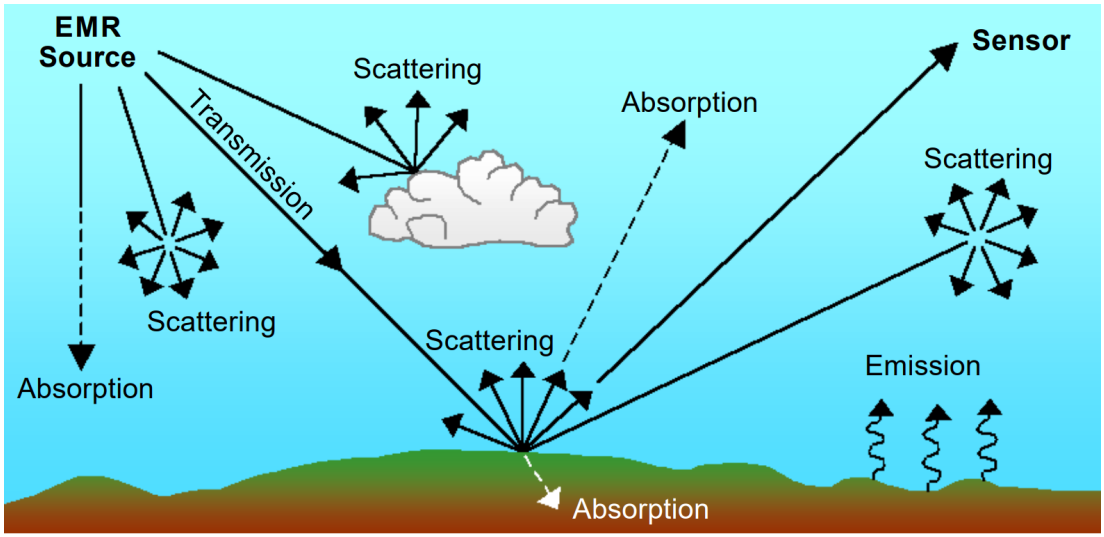


**Figure 2.3 :** Atmospheric interactions during the travelling of energy in the atmosphere [18].

Large gas molecules and particles cause scattering in all directions. Electromagnetic radiation deviated from its actual path and scattered somewhere around the atmosphere. There are three types of scattering in the atmosphere [17, 20]:

1. Rayleigh Scattering: Usually happens in the upper atmosphere. Rayleigh Scattering is caused by tiny particles, for example, small specks of dust or nitrogen and oxygen molecules. Shorter wavelengths are strongly affected by much more than longer wavelengths.

2. Mie Scattering: Usually happens in the lower atmosphere. When the particles in the atmosphere and the wavelength of radiation have the same size, Mie Scattering occurs. In comparison with the Rayleigh Scattering, longer wavelengths more effected by Mie Scattering. Dust, pollen, smoke, and water vapor are the examples causing Mie Scattering.

3. Non-selective Scattering: Particles much larger than the wavelength; for example, water droplets and large dust particles cause Non-Selective Scattering.

Absorption occurs in the atmosphere when molecules absorb the energy at several wavelengths. Ozone, carbon dioxide, and water vapor are the main components causing the absorption [17].

Some regions in the ES do not affect by the atmospheric interactions and called atmospheric windows. It is essential to know the atmospheric windows when designing a new remote sensing sensor [17] and interpreting the images [18].

## 2.4 Spectral Reflectance

The modified solar radiation from atmospheric scattering and absorption reaches the Earth's surface and interacts with the target. The interaction varies depending on the structure of the target. The main types of interactions are transmission, absorption, and reflection (Figure 2.4). Optical sensors, which are sensitive to the ultraviolet, visible, NIR (near-infrared), and mid-IR regions of the ES, receive and record the reflected energy [18].

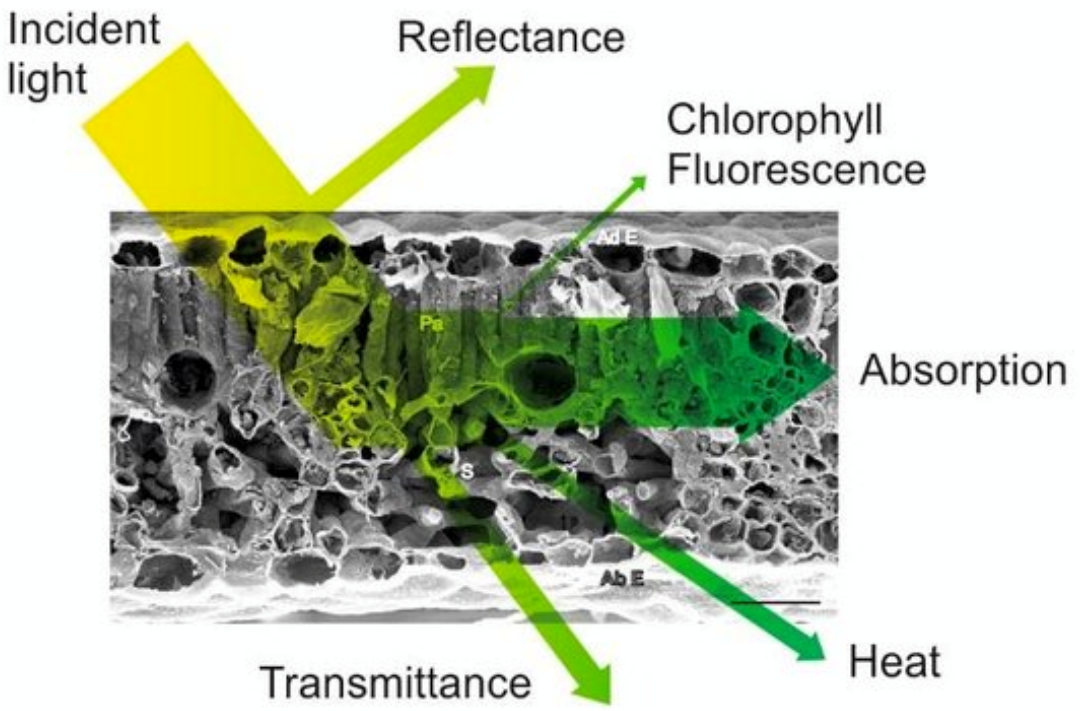


**Figure 2.4 :** Interactions of the incident light with the leaf [21].

Each object shows different responses to different wavelengths [17]. Using reflected solar radiation sensors, it is possible to distinguish different patterns with different responses and understand the materials. When these responses are recorded as the ratio of reflected energy to the incoming energy for each wavelength, spectral signatures can be obtained for each object. As seen in the spectral reflectance graph in Figure 2.5, water, green vegetation, and soil reflect different amounts of radiation in each region

of the ES. Using the differences, it is possible to distinguish them from each other. For example, water does not reflect the IR energy so that it can be easily distinguished, and green plants can be easily separated from the soil at various points of the IR region. Spectral response or spectral reflection can be recorded in the laboratory or field [18].

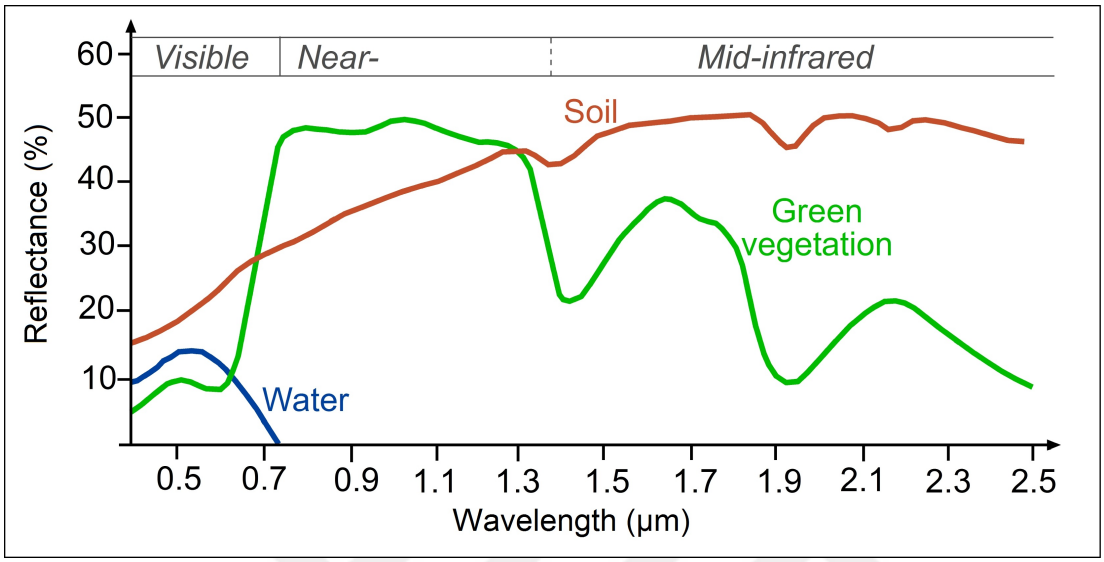


**Figure 2.5 :** Spectral reflectance curves of water, green vegetation, and soil [22].

### 2.4.1 Vegetation reflectance

In remote sensing applications, vegetation studies are directly related to the spectral reflectance properties of leaves and plants [11], but their spectral properties are one of the most critical and challenging tasks because the reflectance properties of plants are complicated. This difficulty is due to living organisms affected by time-varying biochemical and biophysical activities [23].

Plants have low reflectance values for visible lights than other parts of the ES because pigments absorb the visible wavelengths more [24]. NIR wavelengths are highly reflected and absorbed less [23]. Thus, green areas can be easily distinguished in this region.

Chlorophyll is produced from photosynthesis and is one of the most important pigments for leaves [20]. The high chlorophyll content causes the leaves to appear green because the chlorophyll pigment absorbs the red and blue wavelengths and reflects the green wavelengths. When the chlorophyll concentration decreases, less absorption and higher reflection occurs for the red wavelength. For this reason, the

colors of the leaves appear yellowish or reddish. Also, healthy vegetation with high chlorophyll concentration distributes IR wavelengths [17]. The spectral reflectance curve of a healthy green vegetation is shown in Figure 2.6. The absorption of chlorophyll in the visible region is indicated on the graph. The highest reflectance values in the region NIR originate from the cell structure of the plant. Using this significant difference between visible and NIR regions, healthy vegetation can be easily detected. The low values on the graph represent the water absorption of the plant, as water is absorbed very much in the short-wave IR [25].

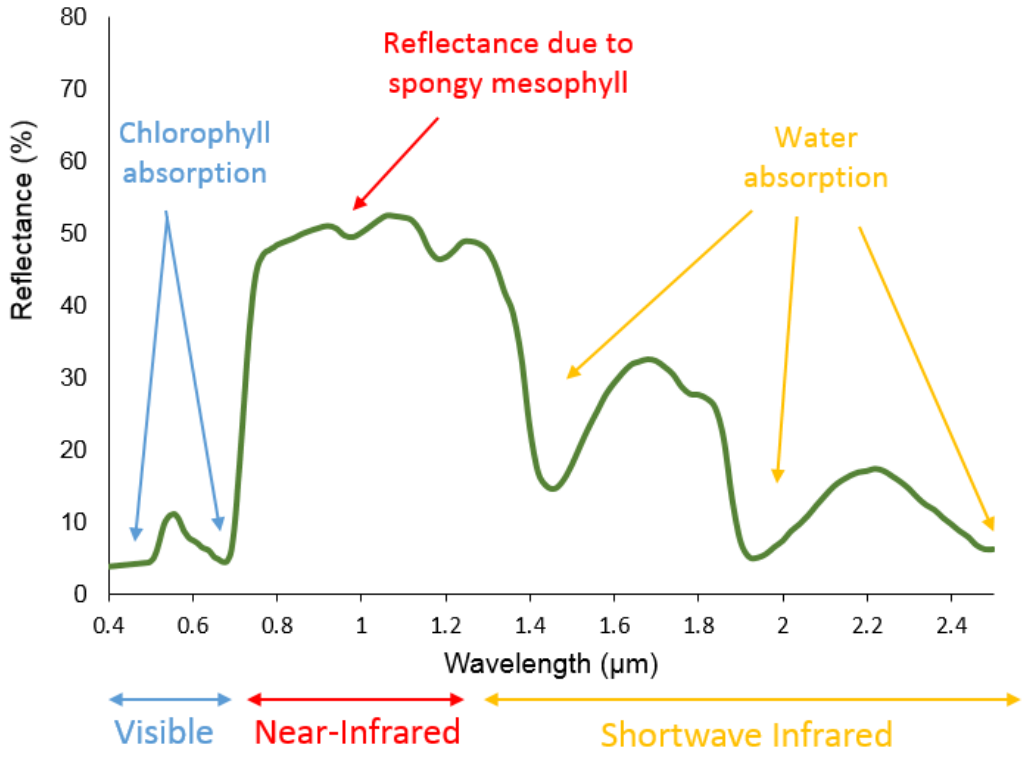


**Figure 2.6 :** Spectral reflectance curve of green vegetation [25].

### 2.4.2 Factors affect the vegetation reflectance

In the remote sensing process, several factors affect the spectral reflectance of objects. As shown in Figure 2.7, factors such as sun angle, topography, atmosphere, and phenology cause changes in spectral reflectance values of different objects [23].

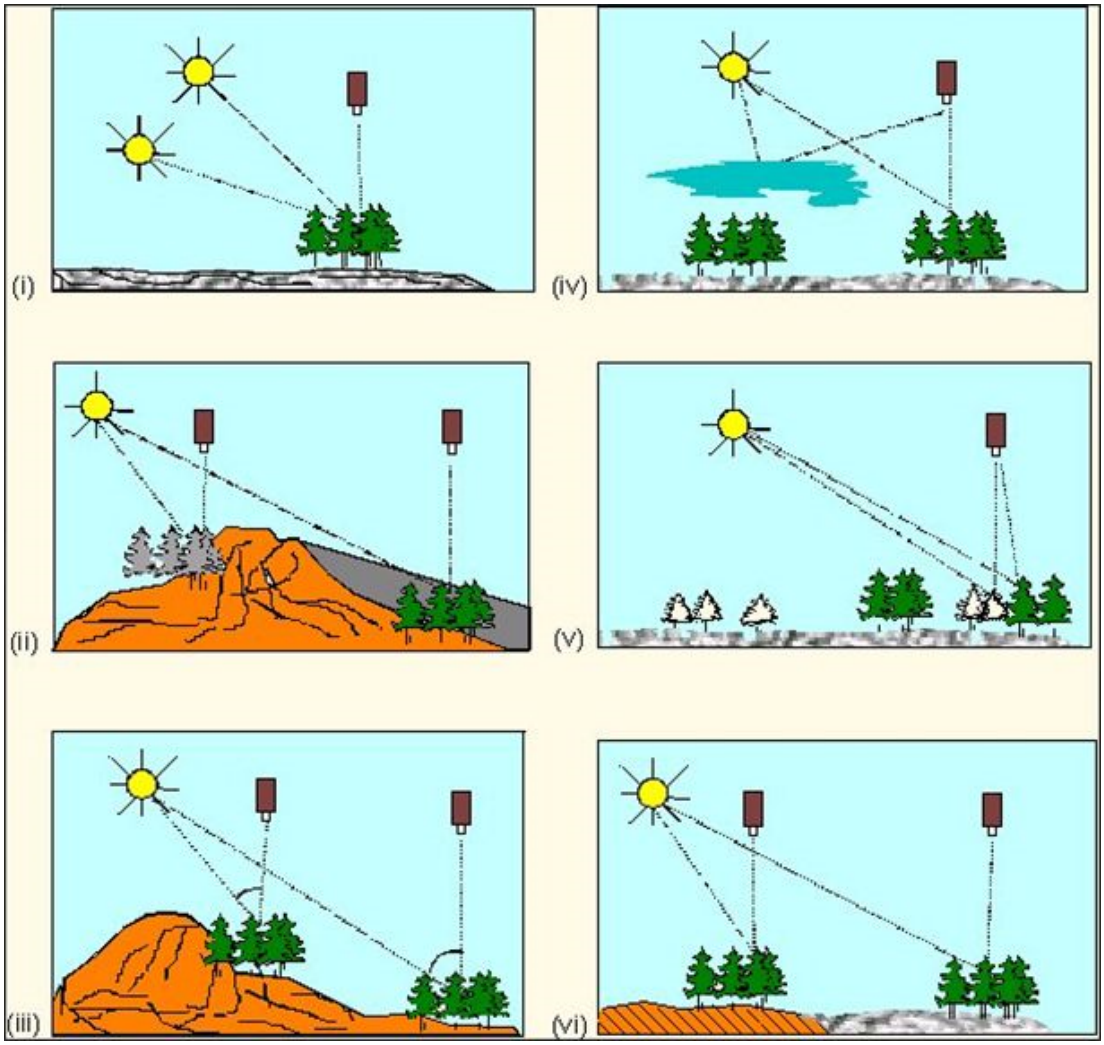


**Figure 2.7 :** Factors affecting spectral reflectance of objects. (i) solar elevation, (ii) aspect, (iii) slope, (iv) atmosphere, (v) phenology, (vi) soil background [23].

Factors affecting plant health, such as plant maturity, diseases, insects, and low humidity also affect the reflection properties of leaves. For example, as the plant ages, its photosynthetic activity decreases, so the amount of chlorophyll decreases, causing a change in the color of the leaf. For this reason, old leaves appear yellowish and have different reflections in satellite images as their reflection properties change. While this effect is observed in both visible and NIR regions, the change is more noticeable in the NIR region [11].

Regardless of the plants and leaves, the spectral reflection of the upper part of the vegetation called the canopy detected by the sensor is critical. Depending on the acquisition angle, the canopy can be seen, but the canopy detection prevents

information from the bottom. Also, shadows cause the leaf to show less reflection than usual. However, this reduction is much higher in the NIR region [11]. At the same time, the sensor also records the reflection of different areas, such as spaces between plants. Therefore, the reflectance values of vegetation may have misleading or different results than expected. The vegetation canopy reflectance values are influenced by factors such as the size, shape, orientation of the vegetation, the areal extent of the canopy, and the characteristics of the ground cover under the vegetation.

### 2.4.3 Spectral reflectance of tomato

The phenological period of a tomato crop varies between 90 to 150 days, depending on the type of seed. Tomato growing cycle consists of 5 stages (early growth, vegetative, flowering, fruit formation, and ripening) shown in Figure 2.8. Each stage takes 20 to 30 days, depending on seed type, temperature, soil structure, soil moisture, and nutrition.

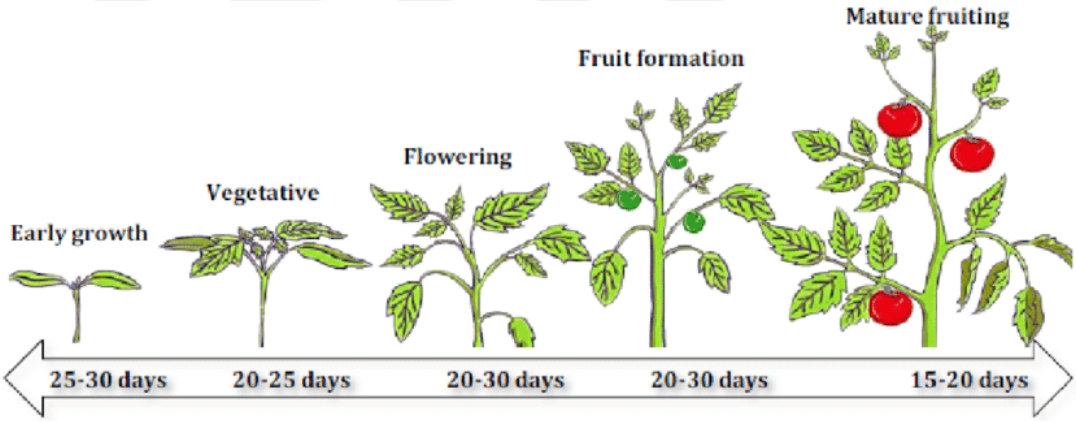


**Figure 2.8 :** Tomato growing cycle [26].

The life cycle begins from the seeds, and the flowers develop as the plant grows and matures. After pollination and fertilization, fruits containing seeds develop and allow the life cycle to begin again (Figure 2.9). Hence, tomato seedlings consist of 3 main parts: green plant, flower, and fruit. Spectral reflectance of a tomato field may be affected by these three parts during the growing period.

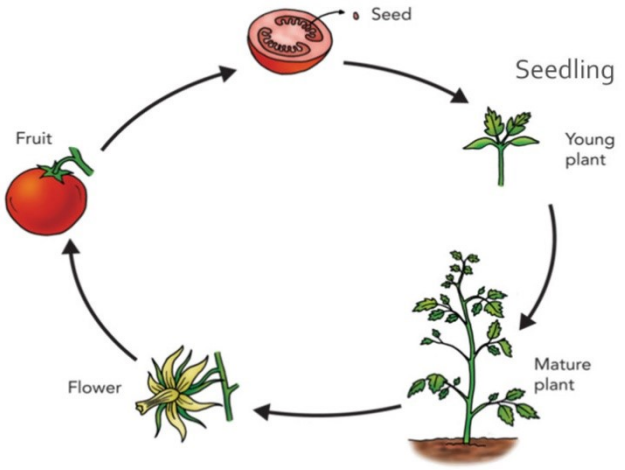


**Figure 2.9 :** Diagram of the tomato life cycle [27].

The green vegetation of the seedling forms the tomato plant. While growing, vegetation covers the field first, and canopy looks green. In image bands with wide wavelength ranges, spectral reflections of various crop plants look similar because they all have the green plant parts, and these similarities cause spectral overlaps. Therefore, it is challenging to distinguish crops from each other, using only multi-spectral information. For example, as seen in Figure 2.10, tomato shows quite similar spectral properties with cotton and sorghum.

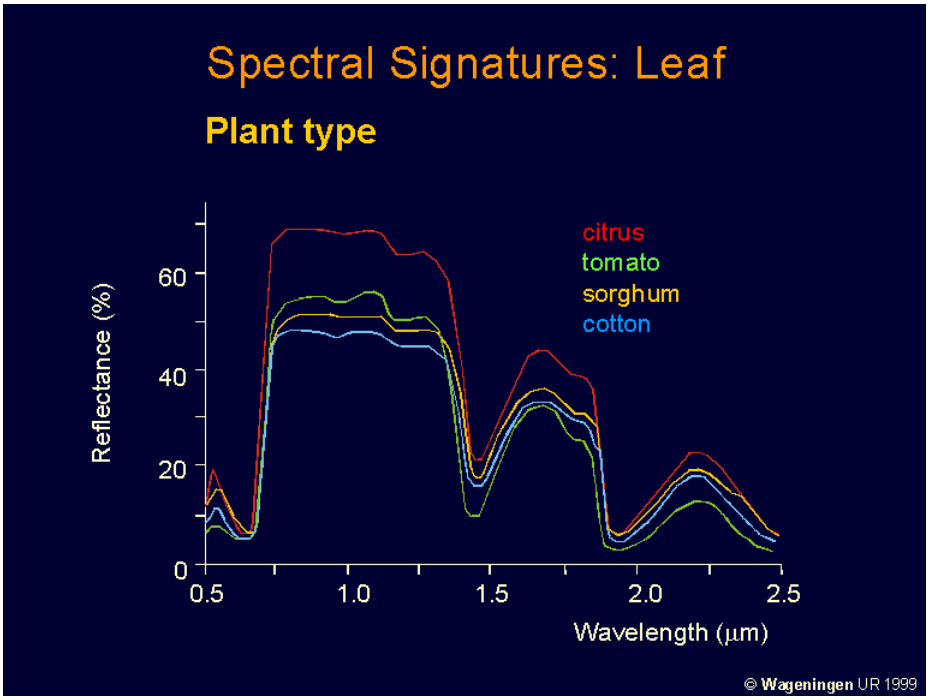


**Figure 2.10 :** Spectral signatures of citrus, tomato, sorghum, and cotton [28].

Tomato fruits begin to emerge after the flowering period. As seen in Figure 2.11, tomato fruit has six stages and turns its color from green to red during the ripening. Each stage has different spectral reflectance values, and it is possible to differentiate between 500-600 nm wavelengths.

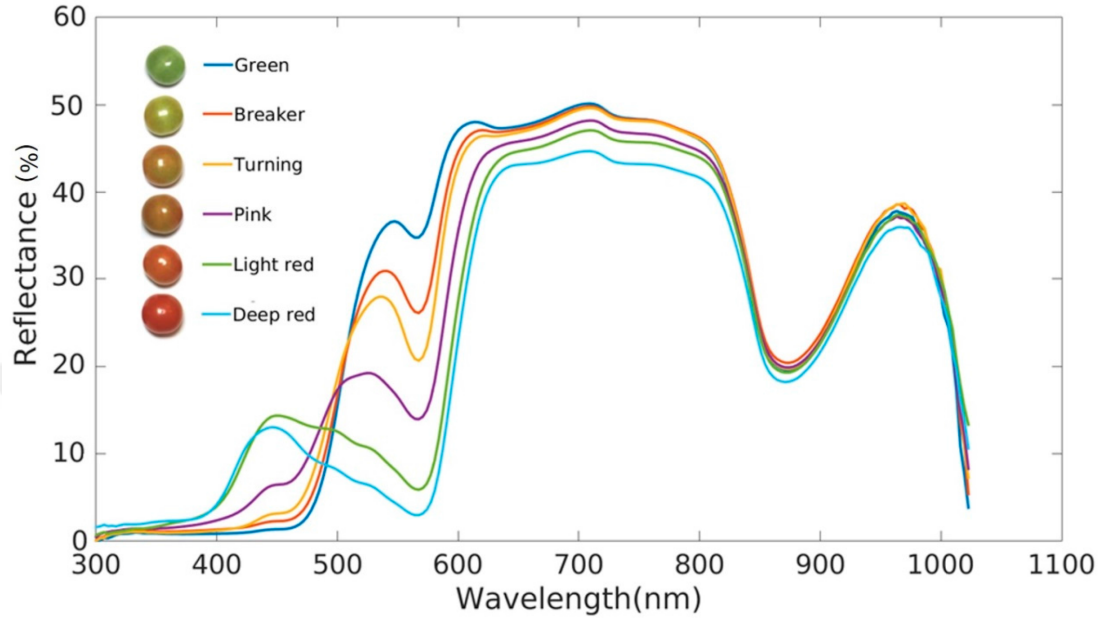


**Figure 2.11 :** Spectral reflectance characteristics of different tomato fruit stages [29].

Healthy and diseased plants can also be detected by using remote sensing technologies based on their different spectral properties. For example, as shown in Figure 2.12, tomato plants that are healthy and having early and late blight diseases can be distinguished between 750 to 970 nm wavelengths. Early and Late Blight diseases are the most common diseases in Turkey after Downey Mildew. Two main reasons for encountering these diseases are warm temperatures or prolonged periods of wetness [30].

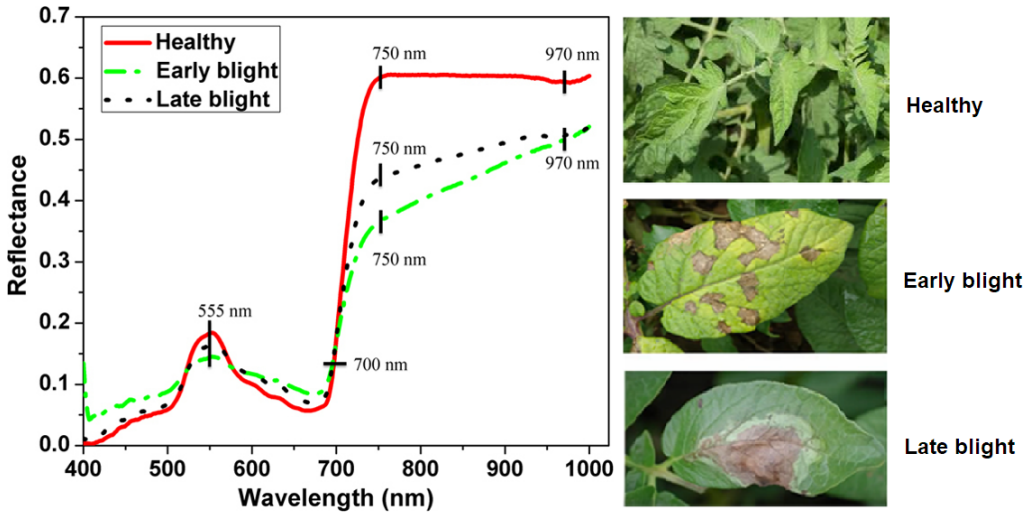


**Figure 2.12 :** Spectral characteristics of healthy and diseased with early and late blight tomato crops [31].

In addition to all these factors, nutrient deficiency of tomatoes can be determined by analyzing satellite data due to the effects of nutrients on productivity. Since nitrogen deficiency is responsible for the production of chlorophyll A, nitrogen deficiency causes a color change in crop plants [32]. Spectral reflectance changes when the amount of chlorophyll pigments decreased. Figure 2.13 shows the spectral differences between soil, healthy, unhealthy, and nitrogen-deficient crops. NIR is the region where these differences are most clearly observed.

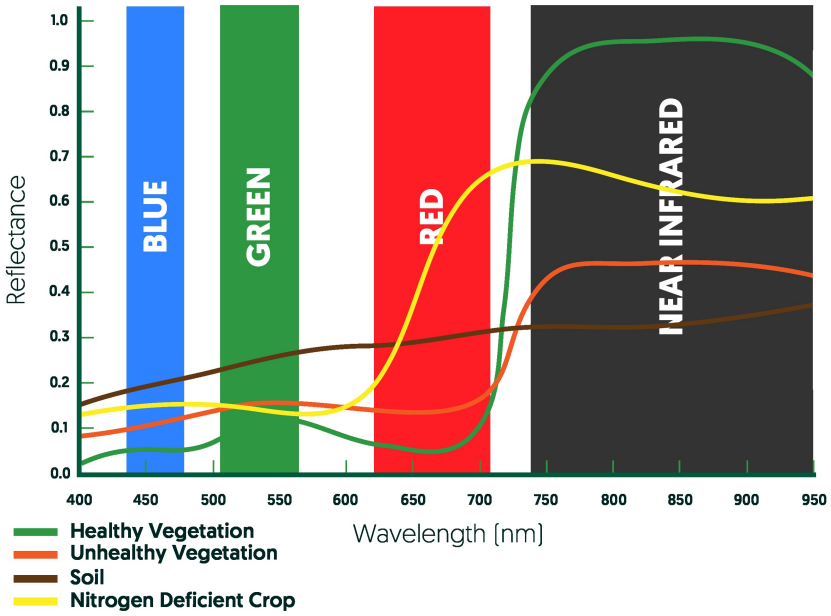


**Figure 2.13 :** Spectral characteristics of soil, healthy, unhealthy, and nitrogen-deficient crops [33].

# 3. USE OF REMOTE SENSING TECHNOLOGY IN AGRICULTURE

## 3.1 Importance of Remote Sensing Technology in Agriculture

Food necessity on Earth is increasing day by day and will continue to increase more rapidly in the future. It is emphasized by agronomists and international food organizations that food production must grow in order to meet this increasing necessity [1]. Traditional systems used to manage food production and to organize food storage and transportation for fulfilling the adequate food supply have limitations [34]. Therefore, it was required to integrate technologies from other disciplines into the system to ensure food security and continuity of production.

With the new and reliable information obtained during the growing period, stakeholders and decision-makers can optimize crop processing and to assess the increase/decrease in food production in the short term. In the long term, they can also rearrange agricultural policies, change investment plans, and assess the impacts [35]. However, crop cultivation status needs to be provided for agricultural monitoring systems in near real-time throughout the season because the information becomes meaningless when it is obtained too late [1].

In agricultural management, it is the most challenging task to accomplish, keeping the costs low and yield high while preventing environmental pollution. With this goal, several techniques have been used for many years. All techniques have various limitations and difficulties. For example, field surveying is a costly and time-consuming technique, especially for large areas because qualified surveyors have to carry out field check periodically on the growing season. To meet all these necessities, land managers started to benefit from Earth Observation and GIS (Geographic Information Systems) technologies.

Remote sensing applications has a widespread usage in agriculture, and are becoming more and more popular because it provides substantial information and helps users to

understand better what is happening on arable lands. Also, cost-efficient and repetitive information can be gained from hard-to-reach regions and large areas. Ongoing and completed studies have shown that it is possible to provide early, satisfactory and accurate information for large areas with remote sensing systems. Hence, periodic and unbiased information with high accuracies are possible with today's remote sensing technologies [35]. In this way, sustainability can be achieved in the food and agriculture chain.

## 3.2 Applications of Remote Sensing Technology in Agriculture

A top-rated application in agricultural remote sensing studies is crop type mapping with crop identification [34]. Using these maps, cultivated crop acreage can be estimated for each type of crop. Also, by estimating crop production, the number of crops expected to be produced for a particular region can be determined. It is possible to identify sowing and harvesting dates and to determine the number of crops that will be harvested over a given time. Crop yield, one of the essential information, has financial benefits for the country because it allows budget planning for the import and export of food products. Estimation and prediction of crop yield studies with remote sensing data is trendy, but a challenging task [36].

Remotely sensed data is crucial for precision agriculture, which is a concept that uses information technologies to observe step-by-step whether the field can get what it needs for health and productivity. This way is opposed to more traditional practices where various crop treatments, such as irrigation, fertilizers, pesticides, are applied equally across the field, ignoring variability in the field. With the use of different sensors, the environment can also be protected by precision agriculture that knows which area needs what and which treatment (e.g., the amount of chemical used). In this technology, it is possible to detect crop conditions by monitoring crop health and growth in a field with the periodic VI maps. Also, crop damages can be determined, and crop quality can be assessed with the detection of crop stress. Diseases and pest infestations can also be detected, and then, control mechanisms can be developed. Also, by using satellite images, the determination of nutrition deficiency and water content is possible for various crops [37]. With routinely analyzed imageries, farmer

compliance monitoring is possible and useful both for private companies and public institutions.

These applications can be used for all types of crops which are cereals, vegetables and melons, fruits and nuts, oilseed crops, root/tuber crops with high starch or inulin content, beverage and spice crops, leguminous crops, sugar crops and other crops [38]). However, this study focuses on crop type identification and acreage determination of a particular vegetable crop, which is tomato.

### 3.3 Tomato Cultivation

Tomato is a vegetable crop that is widely consumed all over the world. On a global basis of horticultural products, tomato ranks at third after potato and sweet potato for volumes of production and ranks at first for processing volumes [1]. Based on the 2017 statistical data of the FAO (Food and Agriculture Organizations of the United Nations), annual tomato production is about 240 million tones on a global scale [39].

Tomato usually grows in tropical, subtropical, and temperature climates [1] because of the necessity of high temperatures and long sunshine duration. Due to its suitable climate and soil structure for growing tomatoes, Turkey has a vital role for tomato production among all countries, as shown in Figure 3.1.

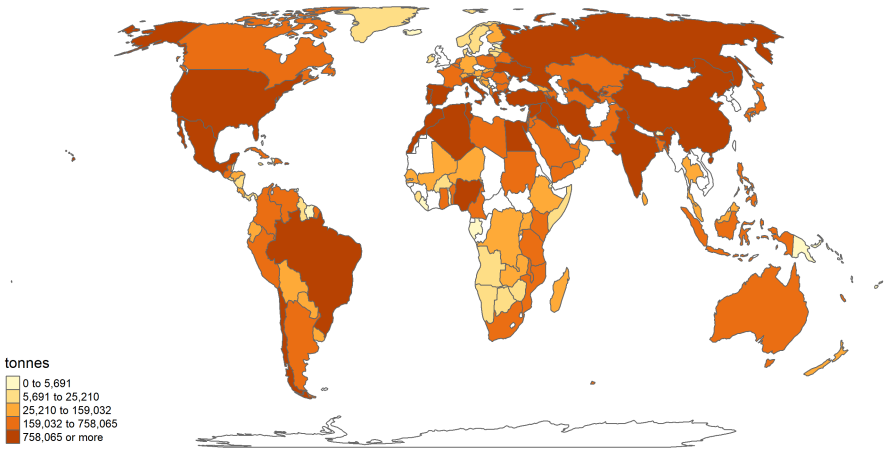


**Figure 3.1 :** Production quantities of tomato, average between 1992 to 2017 [39].

According to the average of the last 25 years, Turkey ranks fourth place in the top ten producers, as shown in Figure 3.2.

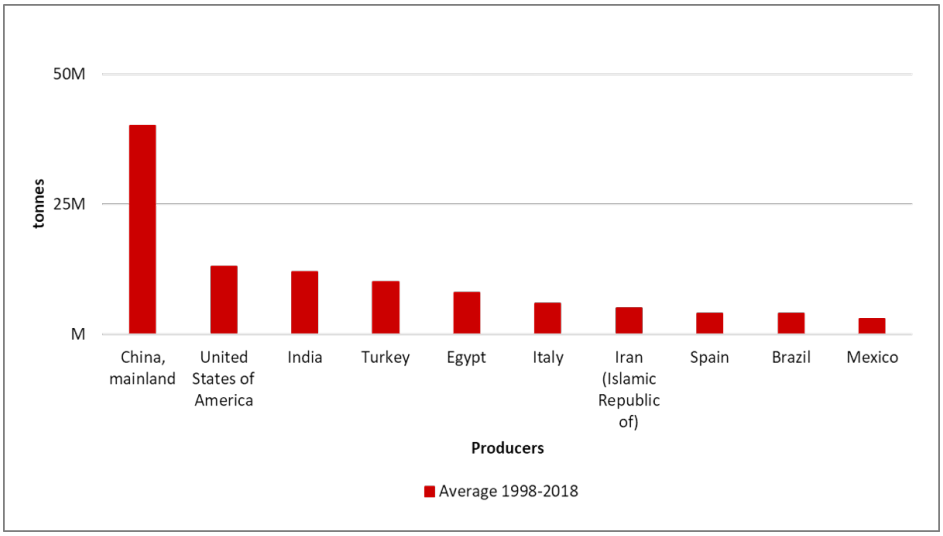


**Figure 3.2 :** Average tomato production of the top 10 producers in global tomato production between 1998-2018 [39].

Ten districts shown in Figure 3.3 are the most common tomato growing regions across Turkey. However, tomatoes are grown in the greenhouses in Muğla, Antalya, Mersin; and Çanakkale is famous for table tomato growing. The leading provinces in tomato paste production are Bursa, Balıkesir, Manisa, and İzmir [40].


**Figure 3.3 :** The most common tomato growing districts and their volumes across Turkey [40].

Estimating tomato-cultivated parcels and calculating cultivation areas are still difficult issues, as they play an essential role in global production and processing. In order to overcome this, this study focuses on identifying tomato cultivated areas using remote sensing technology.

## 4. SATELLITE DATA USED

Planet is a commercial company operating the PS constellation, which consists of 190+ satellites in a CubeSat form factor with the names of "Dove." Due to a large number of satellites in the constellation, daily acquired images cover the entire Earth (Figure 4.1) [41].

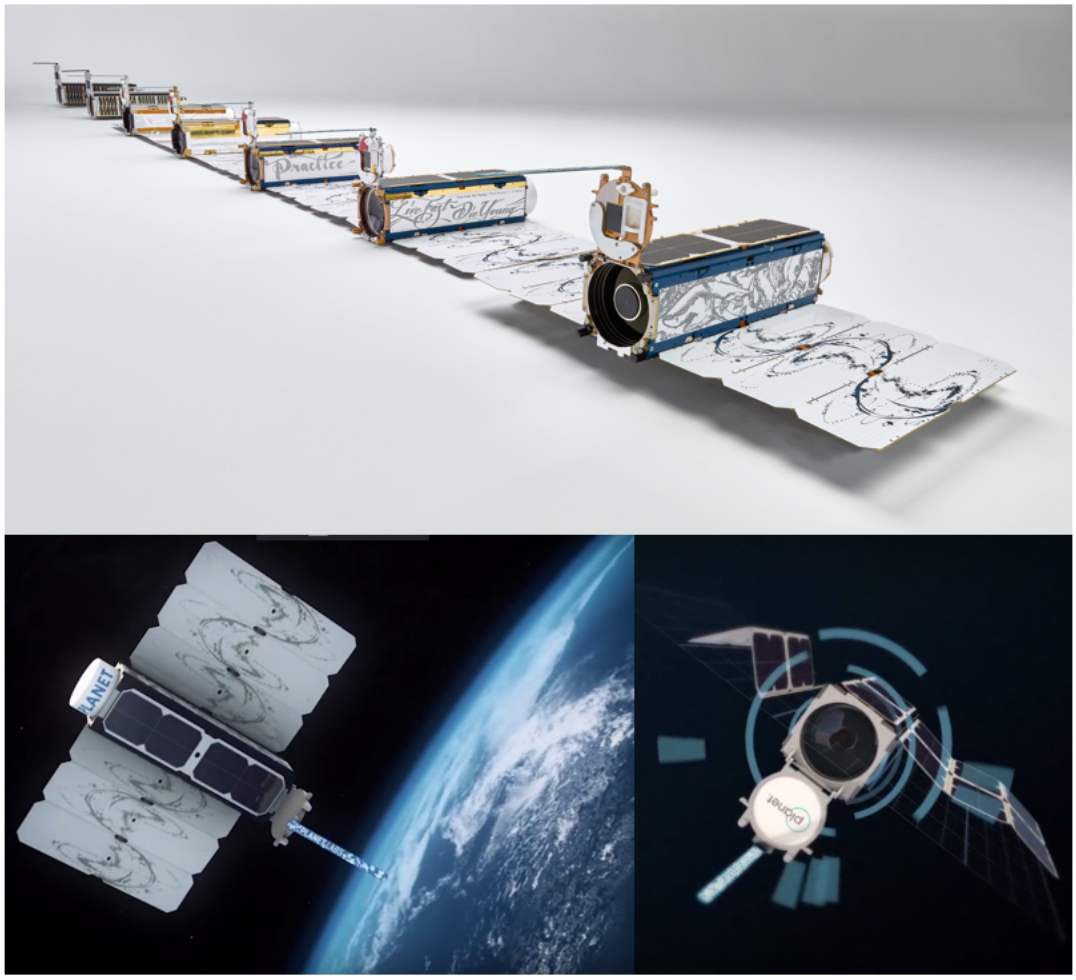


**Figure 4.1 :** Planet's Dove Satellites [42–44].

Satellite images of Planet are prevalent in various industries with different applications. Defense is the most advantageous and the most preferred sector as it provides continuous global monitoring with low latency. Agriculture is the second most widespread sector preferred for sustainability in continuous field coverage. High

resolution and historical data provide the chance to identify opportunities to tap into new markets, so it is preferable for the Insurance industry. It is also preferred in the Energy and Infrastructure sector as it provides the opportunity to manage risks and evaluate activities with its real-time image capacity. Civil governments prefer Planet imagery to map land use, monitor urbanization, and manage resources. Emergency management, forestry, and educational researches are the other application areas [41].

PS images consist of 4 spectral bands with the spectral resolutions shown in Table 4.1 Each Dove satellite acquires images at nadir from 475 km reference orbit altitude. GSD (ground sampling distance) is approximately 3.7 m [41].

**Table 4.1 :** Spectral resolutions of Planet satellite images.

| Spectral Bands | Spectral Resolution (nm) |
|---|---|
| Blue | 455-515 |
| Green | 500-590 |
| Red | 590-670 |
| NIR | 780-860 |

PS imagery products are available as either individual Ortho Scenes, Basic Scenes, or Ortho Tile products. Specifications of each product are shown in Table 4.2.

**Table 4.2 :** Processing levels of PS satellite image products [41].

| Product Name | Description | Product Level |
|---|---|---|
| PS Basic Scene Product | Sensor corrected, scaled Top of Atmosphere (at sensor) radiance product. They were designed for users with advanced image processing and geometric correction capabilities. The product has scene based framing and is not projected to a cartographic projection. Radiometric and sensor corrections are applied. | Level 1B |
| PS Ortho Scene Product | Orthorectified, scaled Top of Atmosphere (at the sensor) radiance image product suitable for analytic and visual applications. The product has scene based framing and projected to a cartographic projection. | Level 3B |
| PS Ortho Tile Product | Radiometric and sensor corrections are applied. Imagery is orthorectified and projected to a UTM projection. | Level 3A |

While Basic Scene Products have only Analytic Data, Ortho Scenes and Ortho Tiles have both Visual and Analytic Data, as shown in Figure 4.2. Visual Products are created as 8-bit natural color images with various image processing techniques and might be used for visual applications. Analytic Products are provided as 16-bit images to be used for calculations and analysis for different purposes [41].

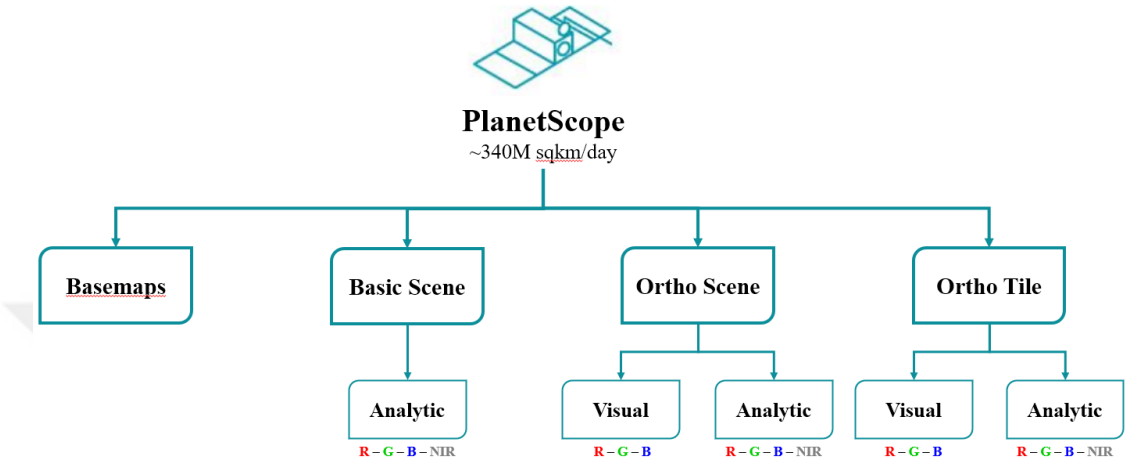


**Figure 4.2 :** PS product offerings [41].

PS Ortho Scenes are overlapping frames with a size of approximately 24 km x 7 km. Since these scenes are not set to a particular grid system, it is easy to mosaic and to clip them in multiple sizes. The scenes are in cartographic projection, and the terrain distortions are fixed. It is orthorectified using GCPs (ground control points). Meanwhile, radiometric and geometric corrections are performed, sensor-related distortions are removed. Geometric corrections are done using 30 to 90 m DEM (Digital Elevation Models). Finally, scenes are resampled with Cubic Convolution kernel and are in WGS84 (The World Geodetic System 1984) horizontal datum, UTM (Universal Transverse Mercator) map projection. For each scene, the spatial resolution is resampled to 3 m, and the radiometric resolution is resampled to 16-bit as a standard. It is also possible to obtain atmospherically corrected products from PS Ortho Scenes, which are called SR (surface reflectance) Products [41].

SR is unitless due to being a ratio of surface radiance to surface irradiance and gives how much light is reflected from the surface. Generally, SR values are range between 0 to 1; however, Planet SR Imagery values are scaled by multiplying 10,000. Radiance values of Analytic Ortho Scene Products are used to offer SR imagery. After preparing

ToA (top-of-atmosphere) reflectance, atmospheric corrections are performed to obtain SR (bottom-of-atmosphere) imageries (Figure 4.3) [45].

**Figure 4.3 :** Comparison of Planet's SR (at the top) and ToA (at the bottom) images [45].

SR is generated with a pixel-by-pixel calculation by using LUT (lookup tables), which comes from the 6S (Second Simulation of a Satellite Signal in the Solar Spectrum) version 2.1 radiative transfer code [45]. 6S version 1.0 is a fundamental radiative transfer code in order to calculate LUTs for MODIS (Moderate Resolution Imaging Spectroradiometer) atmospheric correction algorithm. It simulates the solar radiation reflectance and designed for varying atmospheric, spectral, and geometric conditions. V2.1 is the latest version of the 6S code and available since June 2015 [46]. LUTs are used individual spectral responses of each satellite sensor type, so they are unique for each sensor type. In the conversion to SR, MODIS NRT (near-real-time) data of the same day is used to obtain water vapor and ozone information. Based on the FLAASH (Fast Line-of-sight Atmospheric Analysis of Spectral Hypercubes) atmospheric correction procedure, the 6S atmospheric model with the same image

acquisition time and local latitude is used if overlapping MODIS NRT data is not found [45].

Usually, tomatoes are grown in small fields in Turkey. The spatial resolution of free satellite images is insufficient to distinguish these small fields clearly. Due to the large number of small areas in the study area, the use of high-resolution data was a requirement. Planet provides persistent imaging with high resolutions at affordable prices, and this is the reason why PS images were preferred as a dataset. In this study, 20 multi-temporal images belonging to the cultivation season were selected [47]. In the selection, the "Ortho Scene Products" were chosen due to their suitability for both analytic and visual applications. It is also orthorectified and scaled to SR to eliminate atmospheric effects.

# 5. METHODOLOGY

## 5.1 Pre-Processing

In order to analyze and evaluate satellite images of specific areas, some corrections must be made. These corrections are called pre-processing, which aims to correct sensor- and platform-specific distortions and decrease signal-to-noise ratios. Pre-processing of multispectral images includes geometric and radiometric corrections, and they vary depending on the sensor, platform, and conditions during data acquisition [17].

- Radiometric correction is applied for the different appearances of the same images caused by the viewing geometry, scene illumination conditions, and sensor noise and response [17].
- Geometric correction is performed to remove differences caused by the viewing angle of satellite sensors and terrain roughness. By applying geometric corrections, images from different sensors or different times can be analyzed and evaluated together [48].

As mentioned in Section 2.3, electromagnetic radiation interacts with the atmosphere during its travel. Therefore, it is necessary to apply atmospheric corrections to eliminate the scattering and absorption effects of the atmosphere (Figure 5.1) and to get the real surface properties as much as possible. After atmospheric correction, the radiance values become the SR values.

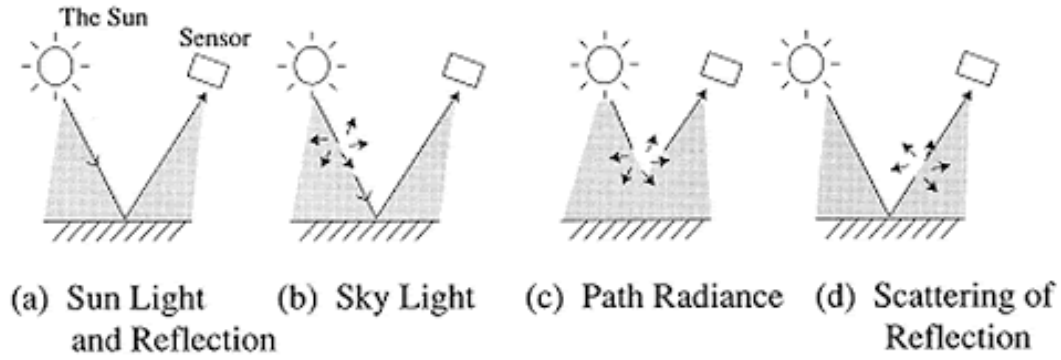


**Figure 5.1 :** Atmospheric effects on incident and reflected energy [49].

In order to provide uniform geometry and homogenous radiometry throughout large areas, individual images have to be mosaicked. Image mosaicking is a method of combining multiple images of the same area to form one large radiometrically balanced image so that the boundaries between the original images are not seen. The output of the image mosaic will be the union of all images (Figure 5.2).

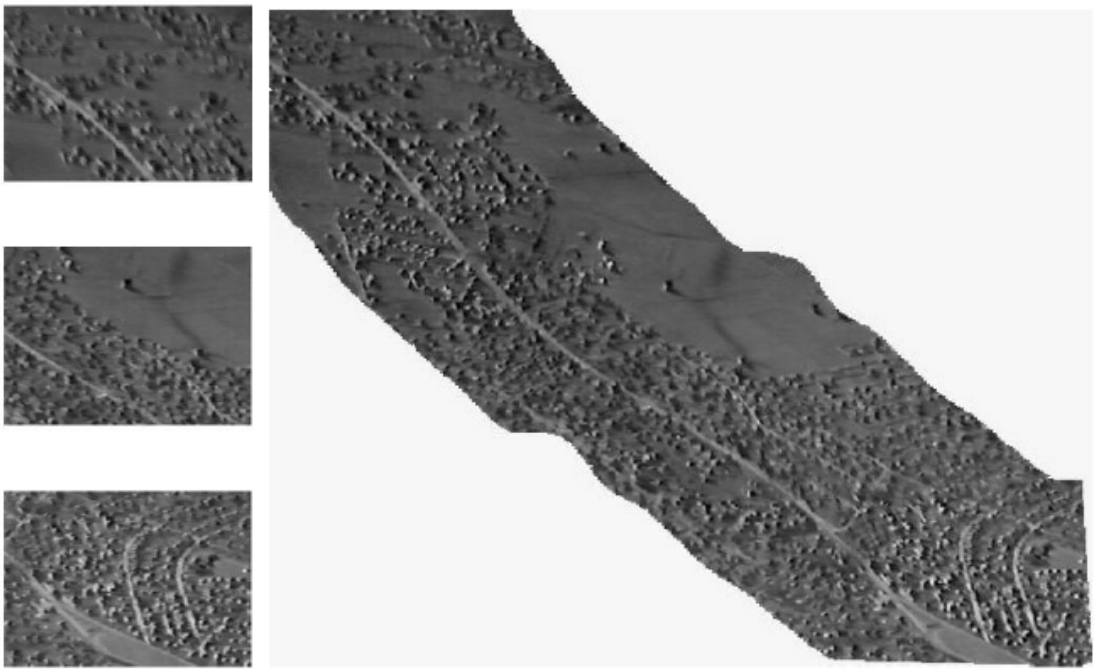

**Figure 5.2 :** Example of image mosaicking [50].

## 5.2 Spectral Indices

Spectral indices are based on simple or complex expressions, such as the ratio of image bands or multiplication of the ratios by coefficients [51]. Indices highlight spectral [25] differences and invisible properties of objects based on their reflections of electromagnetic waves. Many spectral indices have been used to emphasize different surface properties such as impervious surfaces, built-up areas, wetlands, water contents, and vegetation covers, etc.

VIs aim to increase vegetation signatures while minimizing the soil background effects [52]. The principle behind this is the high absorption of healthy green vegetation in the red wavelength due to the leaf pigments such as chlorophyll and high reflectance of vegetation due to internal leaf structure in NIR wavelength (Figure 5.3). On the other hand, unhealthy or sparse vegetation reflects more in red wavelength than healthy vegetation.

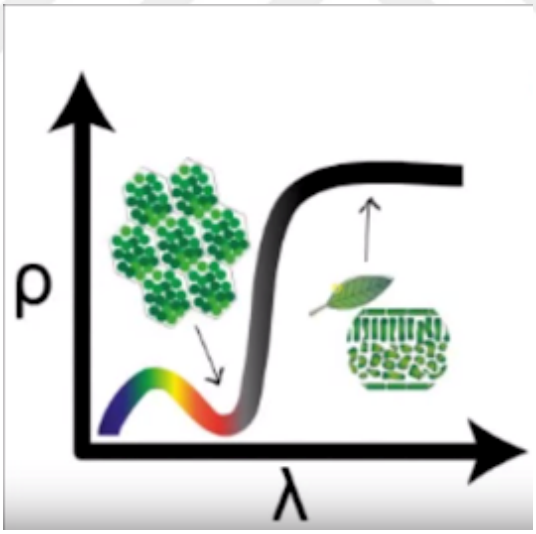


**Figure 5.3 :** Vegetation indices principle [53].

VIs are widely used in agricultural studies since vegetation indices are sensitive to the spectral changes and behaviors of vegetation covers such as forests, arable lands, pastures. Using vegetation indices, it is possible to determine the density of vegetation, to monitor vegetation growth grades, and to assess the vigor by vegetation indices [54]. These features can be detected at a particular time, or their changes can be monitored over time. Growth problems due to nutrition deficiency, irrigation channel congestion,

diseases, or insects can also be monitored by the changes of index values. Also, the use of vegetation indices for crop identification and crop-type mapping has been proven to improve classification performance due to discrete spectral reflections of different crops.

By this time, many vegetation indices have been developed using various image bands. One of the earliest ones is the RVI (Ratio Vegetation Index), which indicates the vegetation with the ratio of NIR and Red bands [55]. NDVI is the most popular one with the ratio of the subtraction of NIR and Red bands to the sum of them. Additional vegetation indices were empirically developed due to the sensitivity of NDVI to external factors, which are canopy background and atmosphere. SAVI (Soil-Adjusted Vegetation Index) was created to minimize the index sensitivity to soil background reflections. In order to reduce the atmospheric effects, the EVI was developed [55]. In the literature, there are hundreds of vegetation indices derived from different expressions such as the TVI (Transformed Vegetation Index), PVI (Perpendicular Vegetation Index). Table 5.1 shows the formulas and descriptions of some of the frequently preferred vegetation indices.

**Table 5.1 :** List of the most common vegetation indices [56–58].

| Index | Formula | Decsription | References |
|---|---|---|---|
| RVI | $\frac{NIR}{Red}$ | General evidence of vegetation. | Pearson and Miller, 1972 [59] |
| NDVI | $\frac{NIR-Red}{NIR+Red}$ | Monitoring the amount of vegetation concentration, greenness, biomass, and pigment content. Enables to track vegetation dynamics and phenological changes. | Rouse et al., 1974 [60] |
| SAVI | $\frac{NIR-Red}{NIR+Red+l} \times (1+L)$ | Corrects and minimizes the soil brightness effects especially for the low vegetation cover. | Huete, 1988 [61] |
| EVI | $2.5 \times \frac{NIR-Red}{NIR+C_1 \times Red-C_2 \times Blue+L}$ | Sensitive to changes for high biomass areas. Reduces the atmospheric effects. Corrects and minimizes the canopy background signals. | Huete et al., 2002 [62] |
| TVI | $\sqrt{(NDVI)+0.5}$ | Removes negative values of NDVI and provides normally distributed histograms. | Rouse et al., 1974 [60] |
| PVI | $\frac{NIR-aRed-b}{\sqrt{1+a^2}}$ | Eliminates the soil brightness effects. | Richardson and Wiegand, 1977 [63] |

NDVI is the most widely used VI in agricultural studies since NDVI offers more photosynthetic capacity of plants. At the same time, SAVI reflects more the canopy structure, and EVI is more suitable for high biomass areas (such as dense forests) where NDVI reaches saturation and is insensitive to variations [64]. NDVI is widely used to monitor and compare the behavior, change, and development of crops over time since it is more stable and easy to calculate [65]. Figure 5.4 shows the NDVI profile of a tomato crop during the growing period. Depending on the increase of foliage, NDVI starts to rise after the sowing day. Following the peak reached, NDVI values

falling with the emergence and maturity of tomato fruits. When irrigation is stopped at a particular time before harvest, fruits turn red, and NDVI values decrease even more.

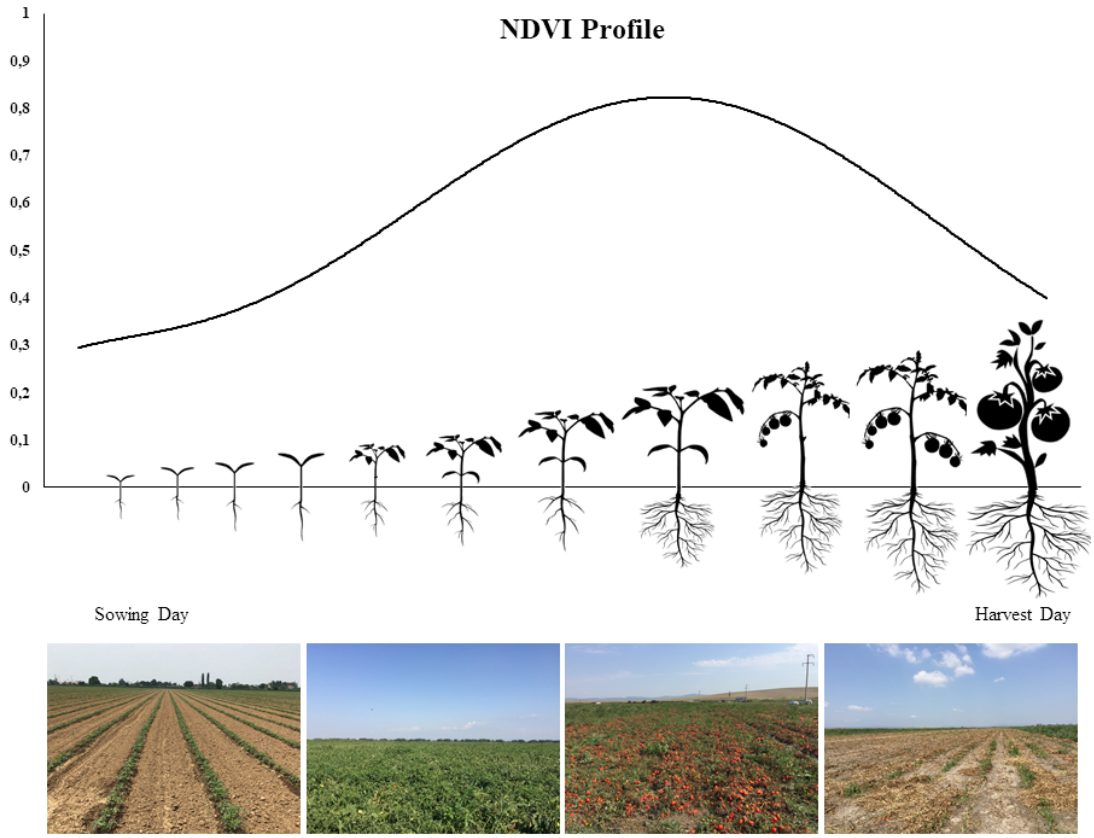


**Figure 5.4 :** NDVI profile of tomato crop from sowing to harvest date.

Besides, indices using Red-Edge bands perform better for vegetation-based studies [66–68]. However, due to the lack of Red-Edge bands of PS images, these indices could not be used in this study. Therefore, NDVI was preferred and used in the classification algorithm to increase the performance of the crop type identification and separability.

## 5.3 GLCM Texture Features

As mentioned in the previous section, vegetation indices provide information about crop growth, canopy, planting patterns, and soil background. However, structural and textural patterns of the fields are also significant factors to improve classification results [69].

Texture is a feature used to identify and distinguish different objects based on variations of the shades of gray. There are various texture calculations, which are statistical, spectral, and structural in the literature [70]. Initially, Haralick, Robert M., Shanmugam. K Dinstein, [71] proposed 14 different texture parameters based on grey-tone spectral dependencies for remote sensing applications. In the following times, additional texture parameters were developed gradually by researchers [9]. All of the second order statistical texture parameters that consider the spatial relationships of the pixels are called the GLCM (Gray Level Co-occurance Matrix) [72] and can be calculated for four directions as shown in Figure 5.5. GLCM values are calculated from a matrix that measures how often a pixel appears in neighboring pixels within a specified direction and distance [51]. However, in many studies, a single "invariant" spatial direction, which is the average of four instead of different directions, is preferred [73].

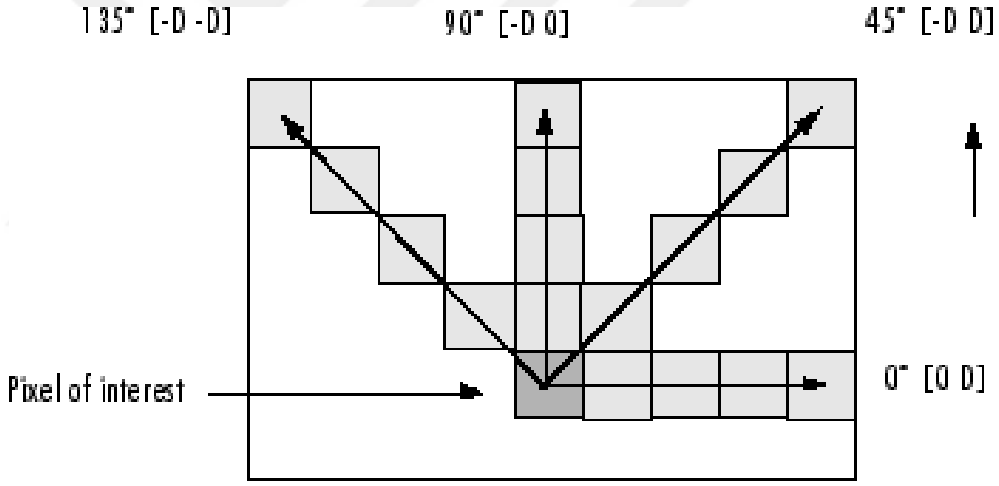


**Figure 5.5 :** GLCM directions [74]

GLCM texture parameters are significant for providing distinctive information for agricultural studies because, unlike spectral indices, texture parameters provide crop density and shape properties [70]. Some of the most preferred GLCM texture features in the literature are shown in Table 5.2. Generally, the use of texture parameters in vegetation indices significantly contributes to better crop discrimination [9]. In this context, NDVI, one of the most popular vegetation indices, was chosen to apply textural parameters, thereby expanding the variability of the feature space.

Based on the evaluation of different GLCM results, ASM (Angular Second Moment), Entropy, and MOC2 (Information Measures of Correlation 2), which respectively

**Table 5.2 :** Some of the most popular GLCM texture features [75–77].

| Texture Feature | Formula | Explanation |
|---|---|---|
| Homogeneity | $\sum_{i=1}^{N_g}\sum_{j=1}^{N_g}\frac{p(i,j)}{1+\lvert i-j\rvert^2}$ | Measures the uniformity |
| Dissimilarity | $\sum_{i=1}^{N_g}\sum_{j=1}^{N_g}\lvert i-j\rvert p(i,j)$ | Measures the variation |
| Entropy | $-\sum_{i=1}^{N_g} p(i)log_2(p(i)+\varepsilon)$ | Measures the randomness |
| Correlation | $\frac{\sum_{i=1}^{N_g}\sum_{j=1}^{N_g} p(i,j)ij-\mu_x\mu_y}{\sigma_x(i)\sigma_y(j)}$ | Measures the linear dependency |
| Energy | $\sum_{i=1}^{N_p}(X(i)+c)^2$ | Measures the uniformity (homogeneity) |
| Variance | $\frac{1}{N_p}\sum_{i=1}^{N_p}(\mathbf{X}(i)-\overline{X})^2$ | Measures the global variation and heterogeneity |
| Angular Second Moment | $\sum_{i=1}^{N_g}\sum_{j=1}^{N_g}(p(i,j))^2$ | Measures the local uniformity (homogeneity) |
| Contrast | $\sum_{i=1}^{N_g}\sum_{j=1}^{N_g}(i-j)^2p(i,j)$ | Measures the variations |
| Information Measures of Correlation 2 | $\sqrt{1-e^{-2(HXY_2-HXY)}}$ | Measures the local homogeneity |

emphasizes homogeneity, randomness, and correlation of crops grown in the region, were taken into account.

## 5.4 Image Classification

Using remote sensing images, land use, and land cover information can be obtained through image interpretation and classification process. For this reason, many image classification techniques have been developed to obtain updated land use and land cover information at different scales since the 1980s. Most of the previous classification techniques are pixel-based, where each pixel is labelled as a single land use and land cover class [20]. In this context, there are some classification approaches such as unsupervised (i.e., K-Means and ISODATA), supervised (i.e., ML, Artificial Neural Network, DT, SVM, RF), and hybrid classification (i.e., semi-supervised

and fusion of supervised and unsupervised learning). However, these pixel-based classification approaches have limitations when applied to heterogeneous regions, since the size of an object can be much smaller than the size of a pixel [78].

In this study, a supervised RF classifier was used, and therefore more detailed information is given in the following section.

### 5.4.1 Random forest (RF)

The reason for choosing RF as a classifier in this study is to map crop types with better classification performance and processing speed [79]. RF is a supervised machine learning classification and regression algorithm that grows with an ensemble of DTs that combine predictions from multiple trees and provide better results than a single tree [80]. In the supervised classification, the training data set is created by predefining and labelling the input data classes and then is given to the algorithm [81, 82]. Thus, the classification algorithm can learn the properties of target classes from training data and use them to classify data that has not yet been defined [79].

Although it consists of ensemble DTs, RF differs from DT due to the randomly running processes: finding the root nodes and splitting the internal nodes [83]. Besides, RF can overcome the disadvantages associated with a single DT while maintaining its advantages [80]. Each tree in the RF algorithm is created by the values of randomly collected input variables to estimate the value of the output variable through supervised learning [84, 85].

The components of a single DT are shown in Figure 5.6. Nodes represent possible attributes associated with an event; the first node called root represents the most significant information gain, branches represent attribute values, and finally, leaves represent classes [81, 86]. Variable and split value to divide in a node, decision to stop or split again, and assigning leaf nodes to a class are determined when creating a tree [87].

RF has many advantages that are being non-parametric and having the ability to deal with outliers in training data [80]. RF also prevents overfitting if a sufficient number of trees would be found. There is no need to apply a variable selection or data reduction before using the algorithm because RF automatically identifies the best predictors of a large number of data. Also, pre-processing is not required for the input dataset.

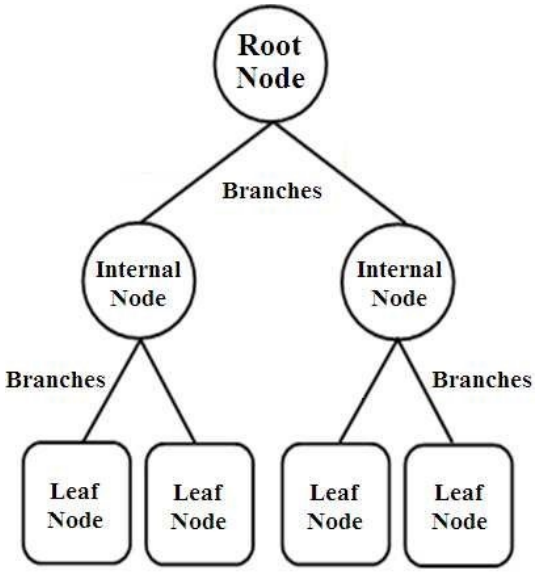


**Figure 5.6 :** The components of a DT [86].

Randomness in ensemble trees makes RF more reliable because it enables the ability to handle automatically with missing data [88]. The structure of RF gives it a calculation capability of classification error and variable importance [80]. Compared to other machine learning algorithms such as SVM, RF is not very sensitive to the parameters used, but on the other hand, it is easier to determine the parameters to be used, which is an advantageous feature [80, 89]. Figure 5.7 shows the structure of an RF model with a large number of DTs.

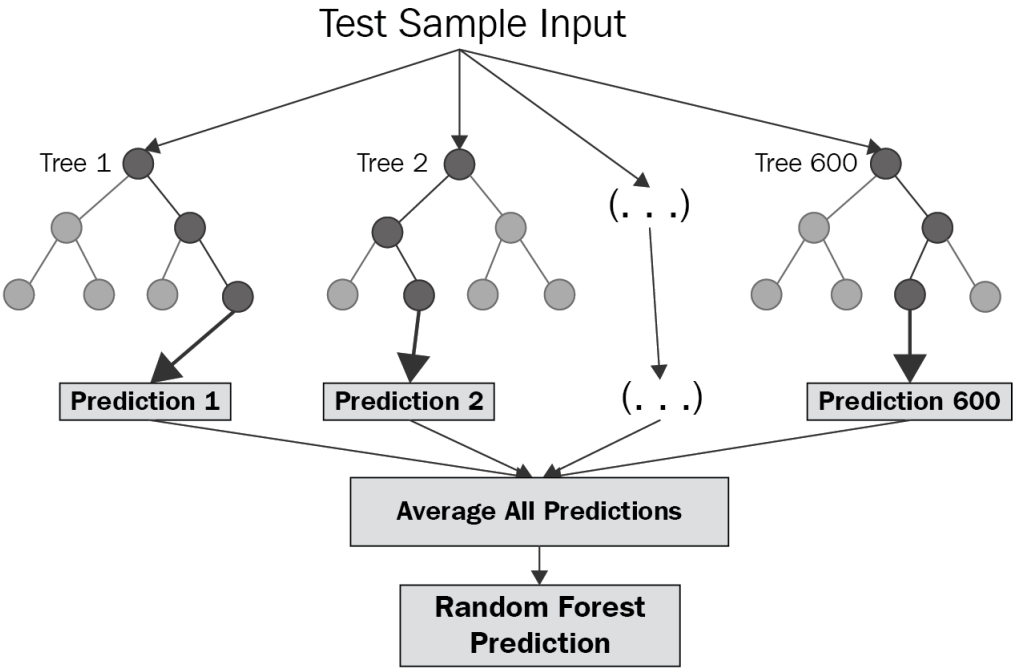


**Figure 5.7 :** RF structure [90].

There is a direct proportion between the number of trees and the accuracy of estimation results because RF is an ensemble method that utilizes the results of all trees to make decisions. RF classification generally evaluates the responses from hundreds of different DTs to decide which class a pixel or object belongs. It looks at the classes predicted by all trees, and the class predicted by the majority becomes the class assigned to that pixel or object [80,89]. For example, in a pixel-based RF classification with 500 trees, if 350 trees estimate that the pixel is tomato, 80 tree peppers, and 20 tree watermelons, this pixel is ultimately assigned to the tomato class.

There are two steps to creating trees. In the first step, RF makes random selections from training data to develop the models of each DT. That is, each tree randomly selects different variables from the input dataset. However, one-third of the training data (out-of-bag samples) is used by the algorithm for model testing. In the second step, the condition to leave each node of trees to create the binary rule is randomly selected. The user can determine the number of random selections, or it can be left to the algorithm. In this way, the correlation between trees and the error rate is reduced. The critical thing in this process is to choose the right number of variables to provide a low correlation with sufficient predictive power [80, 89].

RF algorithm includes specific parameters [80, 91]:

1. Prediction variables (such as image bands), and response variables (such as land cover type) as input training data,
2. Number of trees,
3. Number of prediction variables for binary rules of each split/decision,
4. Parameters for calculating error and variable significance.

Some variables have significant effects on classification results, while some have low importance. Therefore, the determination of these variables, in other words, the variable significance is important [92], and RF is successful in this regard. Thus, it is possible to remove variables that provide less information to the analysis, and the model can be rerun without them. This detection is particularly important in the classification of multi-band satellite images because training sets may contain

insignificant data. Also, outliers in the training data that differ from other data in the class to which they belong can be evaluated with RF. Thus, the classes with outliers can be identified, and the training set can be revised [80].

### 5.4.2 Stratified k-fold cross-validation (CV)

The most critical issues related to classification models are model assessment based on the question "How good is the model?" and model selection based on the question "Which model is the best?". One of the strategies for evaluating the model is to apply CV (cross-validation), one of the statistical approaches, to select the best performing models in the literature [93]. CV evaluates the reliability and stability of the classification results [94] and presents the information about the robustness of the model [95].

Adequate and reliable ground-truth data is essential in the supervised image classification of satellite data. The most common way is to do fieldwork. However, it is often problematic because it is expensive, difficult to manage, error-prone, and time-consuming. Also, the reliability of the data collected depends on the person working in the field. For these reasons, it may not always be possible to gather sufficient data required for both training and validation. In this case, it is possible to train and validate the classification model with a single and limited set of data; and the CV gives outstanding results in this regard.

There are several types of CVs in the literature, and Spatial CV, K-Fold CV, Stratified K-Fold CV, and Leave One Out CV are some examples. The model performance is directly related to the data selected for training and validation. However, it causes the model to underperform because most of the data cannot be homogeneous.

The Stratified K-Fold CV was selected in this study as it was developed to remove the uncertainties of the data partition [95] and is described in more detail in this section. The K-Fold CV validation process is shown in Figure 5.8.

Firstly, in n K-Fold CV, data is divided into predefined k parts. One of the k parts is selected to assess the model, and the remaining (k-1) parts are used to train the model. Each part is called fold, and this process is repeated until all folds are used for the validation [96]. However, it is possible to occur an imbalance in the dataset. For example, the number of some of the crop classes might be higher than others. In this

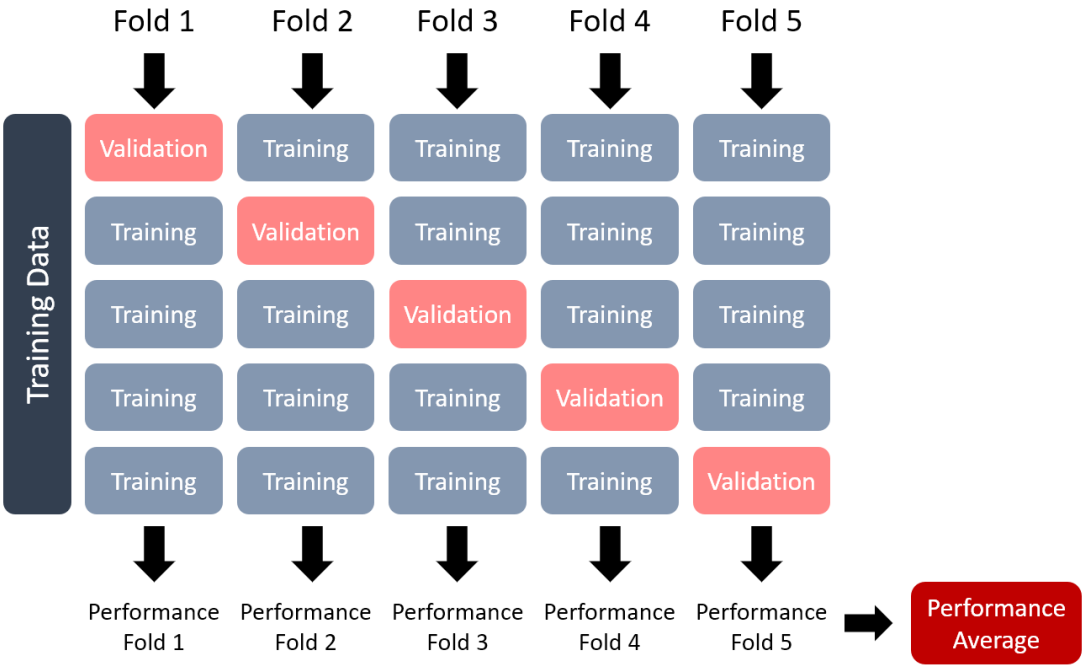


**Figure 5.8 :** Illustration of the K-Fold CV process.

case, with the use of a stratified k-fold CV, each fold contains the same percentage of samples of each class [97]. Figure 5.9 shows a comparison between the validation and training data partitions of k-fold and stratified k-fold CVs. As shown in the Figure 5.9, K-Fold divides the data equal to the predefined number. However, Stratified K-Fold divides proportionally to the number of samples in the class. Thus, the same percentage of samples appears in each set [98]. The data partition is the advantage of Stratified K-Fold CV.

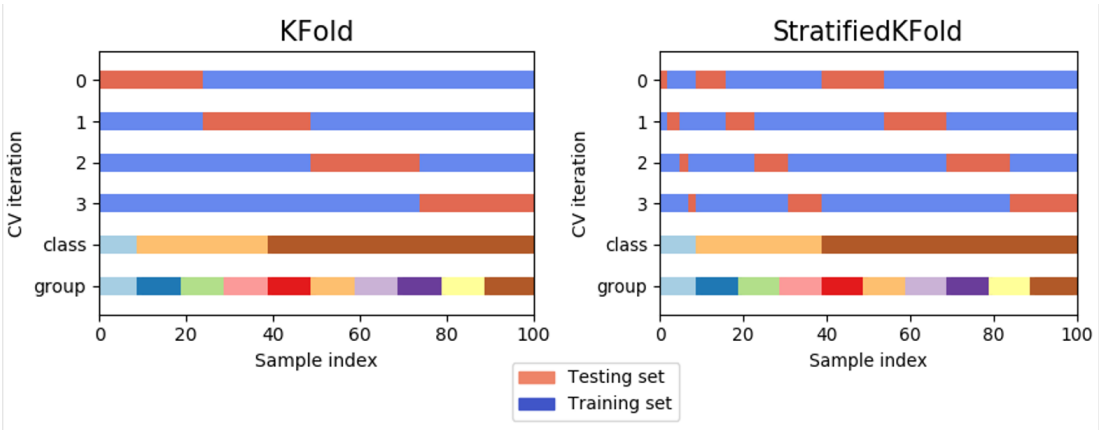


**Figure 5.9 :** Sampling methodologies of K-Fold and Stratified K-Fold CVs [98].

After model assessment, the best performing model should be determined in model selection. In order to select the best performing model, errors of each model can be evaluated with CV results, and the best performing model with the least estimation error may be selected [93].

### 5.4.3 Accuracy assessments

It is essential to evaluate the image classification performance and to determine how reliable the results can be, especially for actions to be taken based on the classification results. Although there are various approaches in the literature, Bootstrap and error matrix are highly recommended and widely used methods to evaluate the reliability of test data, and the accuracy of classification results, respectively.

#### 5.4.3.1 Accuracy assessment with error matrix

It is possible to evaluate how proximate the classification results to the real-world values, and for this purpose, the error matrix is a common technique used in remote sensing to perform this assessment. In the accuracy assessment with an error matrix, the classification and reference data are compared [99, 100]. In other words, the error matrix shows where confusion occurred during classification [101]. Meanwhile, it is an advantageous way to understand what is correctly done as a result of the classification and what kinds of errors are made. According to the error matrix, all the differences between classification results and reference data are due to classification and / or identification error since the reference data is considered to be "true" [102].

Error matrix consists of columns and rows. In general, reference data are shown in columns, and the predicted classes are shown in rows [99]. Figure 5.10 shows an example of an error matrix with the calculations of different types of accuracies.

Total accuracy is calculated by dividing the number of correctly classified pixels (the sum of the diagonal) by the total number of pixels in the error matrix. Likewise, the correctly classified number of pixels might be divided by the total number of pixels in the reference data (in a column) or classified data (in a row). The producer of a classification is concerned with how well it can classify the relevant area. Accordingly, the Producer's Accuracy might be obtained by dividing the total number of correct pixels in a class by the total number of pixels as coming from the reference data (in the

| | | Reference Data | | | | |
|---|---|---|---|---|---|---|
| | Classes | A | B | C | D | Row Total |
| Classified Data | A | 65 | 4 | 22 | 24 | 115 |
| | B | 6 | 81 | 5 | 8 | 100 |
| | C | 0 | 11 | 85 | 19 | 115 |
| | D | 4 | 7 | 3 | 90 | 104 |
| | Column Total | 75 | 103 | 115 | 141 | 434 |

| Poducer's Accuracy | |
|---|---|
| A | 65/75 = 87% |
| B | 81/103 = 79% |
| C | 85/115 = 74% |
| D | 90/141 = 64% |

| User's Accuracy | |
|---|---|
| A | 65/115 = 57% |
| B | 81/100 = 81% |
| C | 85/115 = 74% |
| D | 90/104 = 87% |

$$Overall\ Accuracy = \frac{65 + 81 + 85 + 90}{434} = \frac{321}{434} = 74\%$$

**Figure 5.10 :** Example error matrix [102].

column). As a result, an omission error is obtained, which indicates the probability of how accurately classified of the pixel in the reference data. Meantime, the division of the number of correctly classified pixels of a class to the number of total pixels of that class gives the User's Accuracy. It provides the commission error, which indicates the probability that a classified pixel represents its class on the ground [99].

#### 5.4.3.2 Accuracy assessment with bootstrapping

It is crucial to determine how well test data represents the region since it is not possible to collect the data of the whole region when evaluating the classification results. To achieve this, there are lots of techniques in the literature. One of these is Bootstrap, a resampling method that randomly samples the dataset with replacement [103]. The Bootstrap method can also be used to evaluate the performance and statistical properties of the model (estimator) because a model might be hypersensitive to noise in a dataset [104]. It also yields on the assessment of classification uncertainty and discovering how sample bias affects the results [105].

In order to evaluate the classification accuracy by Bootstrapping, a sample population must be determined. Then, the determined number of samples will be repeatedly selected from the test set with different combinations, and all the evaluations will be averaged for the final assessment [106, 107]. The critical point is that a previously

selected observation can be included in the sample population multiple times, and this is the reason why bootstrap is called resampling [106].

Two parameters must be specified before running a bootstrap algorithm: sample size and repetitions. The sample size represents the sample population, which will randomly be selected by the algorithm. The sample size should be selected based on population size and the performance of the environment in which calculations are to be done. It is possible to reduce the effects caused by the random sampling errors, naturally found in the bootstrap procedure by increasing the number of samples. The maximum sample size can be equal to the number of data in the test set. However, the increased number of samples does not increase the amount of information that comes from the original data [108]. Repetition represents the repetition number to be performed. When selecting the number of repetitions, it is necessary to be noticed that the amount should be large enough to allow the calculation of the statistics. The low number of repetitions will cause deviations in statistical calculations. Therefore, it is recommended to do it hundreds or even thousands of times in the literature [106]. Figure 5.11 shows the sampling methodology of Bootstrapping.

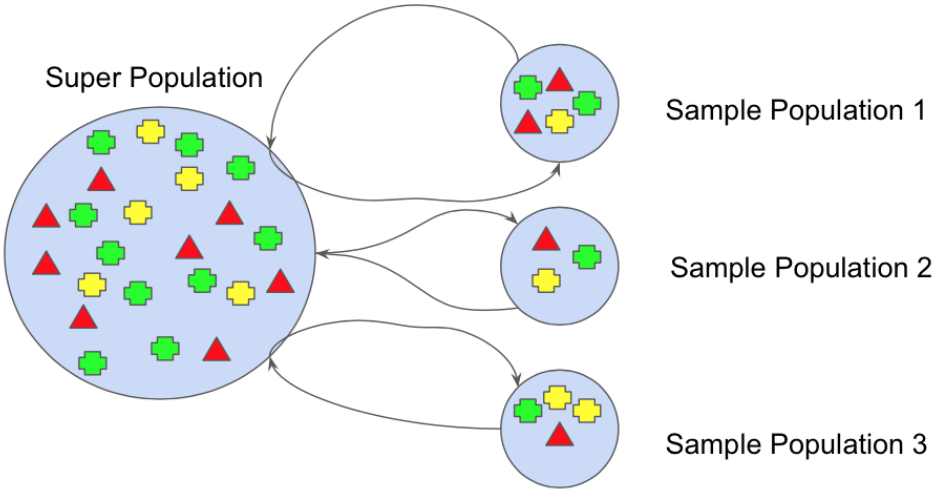


**Figure 5.11 :** Sampling methodology of Bootstrapping [109].

Bootstrap is an advantageous method that is frequently used in statistics. It is almost unbiased due to the way it develops, but it may have a considerable level of variance [110]. Bootstrapping is based on that repeating the sample continuously for the same data set makes the data closer to the real population [107]. Since it creates its

own sample sets required for continuous repetition, it is a time-saving and a handy method by eliminating the weight of re-preparing a data set and re-obtaining the results [106]. Bootstrap prediction results are usually in the Gauss distribution and give the model's prediction ability within a confidence interval. These intervals are matched quite closely to exact confidence intervals, and the results are trustworthy in all situations [110]. Variance measurements, such as standard deviation, standard error, and some other measures, might be obtained [106]. Bootstrap is suitable for checking the consistency of results. While the real confidence interval is unknown in most cases, bootstrap is comparatively (asymptotically) more accurate than the standard intervals achieved using sample variance and normality assumptions [111].

# 6. APPLICATION AND RESULTS

In this thesis, it is aimed to detect the tomato cultivated fields and calculate their areas by RF classification. As a first step, fieldwork was conducted to collect ground-truth data for creating training and test data. Meanwhile, pre-processing steps were applied to Planet images [47] with 4-band and 3-m spatial resolution, and image features (spectral indices and GLCM textures) were prepared for use in classification. Then, RF classifications and accuracy assessments were performed with different methods and image feature combinations were used to determine which features increased tomato classification accuracy. Figure 6.1 shows the flowchart used in the study.

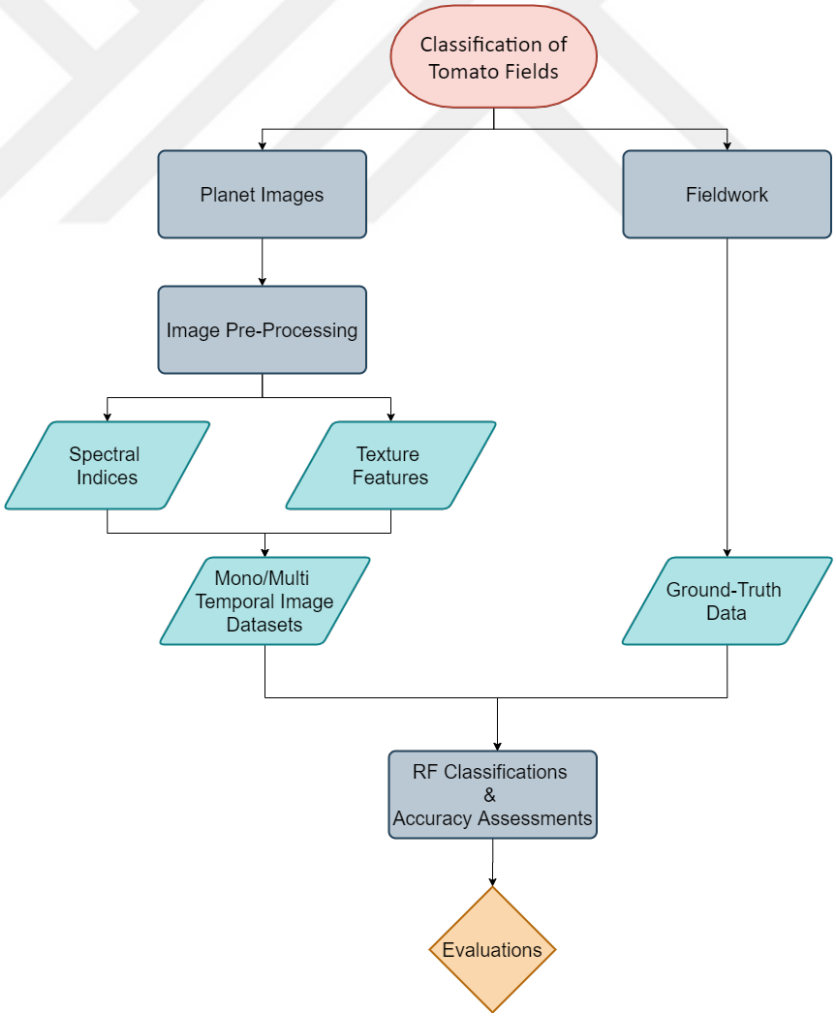


**Figure 6.1 :** Flowchart used in the study.

## 6.1 Study Area

The study area is in Karacabey, which is a district of Bursa province and located in the southern Marmara Region of Turkey. It is surrounded by Mudanya and Bursa from the East, Mustafakemalpaşa, and Susurluk from the South, Manyas from the Southwest, Balıkesir, and Bandırma from the West, and Marmara Sea from the North. Karacabey plain is located to the southeast of the district center and was formed during the collapse of the 4th geological time [112]. The two most important natural beauties of Turkey, Ulubat Lake, and Manyas (Kuş) Lake, are located in the eastern and western parts of the plain, respectively.

Karacabey's climate is a mixture of Mediterranean and Black Sea climates. Due to warm and rainy winters, precipitation is mostly seen as rain. Usually, summers are dry. According to 5-year temperature observations, the highest is 38.5 ° C in August, the lowest is -9.7 ° C in February, and the average annual temperature is 14 ° C. The average annual rainfall of Karacabey, obtained from 29 years of observations, is 562 mm [112].

Continuing drought in autumn and postponing autumn rains have been a significant concern for farmers in recent years [112]. In the meantime, heavy rains and hailstones in the summer months, which are considered as a result of climate change, cause damage to agricultural areas.

Agricultural activities are common and intensive in Karacabey plain. Wheat, tomato, barley, corn, beans, peas, sugar beet, cotton, sunflower, and tobacco are the most commonly cultivated crops in Karacabey plain. [113]. Meanwhile, crop pattern varies according to the changes of climate and soil conditions and the support provided to farmers.

Today, Karacabey is shown as both agricultural and agricultural industry production area in 1/100.000 scale plans of Bursa. The region covers 35% of field crops, 46% of vegetable products, and 28% of agricultural income grown in Bursa. Karacabey is fourth in the ranking of industrial tomato cultivation by supplying Turkey's %40 of tomato needs with 140.000 da area of industrial tomato cultivation, and tomato paste production factories producing annually 181.651-ton tomato paste. Besides, due to the favorable conditions of the region for seed production, Karacabey is on the way to

become the center of the seed sector with the increasing investments of domestic and foreign companies [114].

Due to the rapidly growing interest in agricultural production in the region, the study area was chosen as the Karacabey plain (Figure 6.2). The study area is located approximately at the center of the plain (40°09'55.75" N and 28°13'14.51" E) and has an area of 22.97 ha. Karacabey plain is located 25 km north of the 40th parallel and 20 km east of the 28th meridian [112].

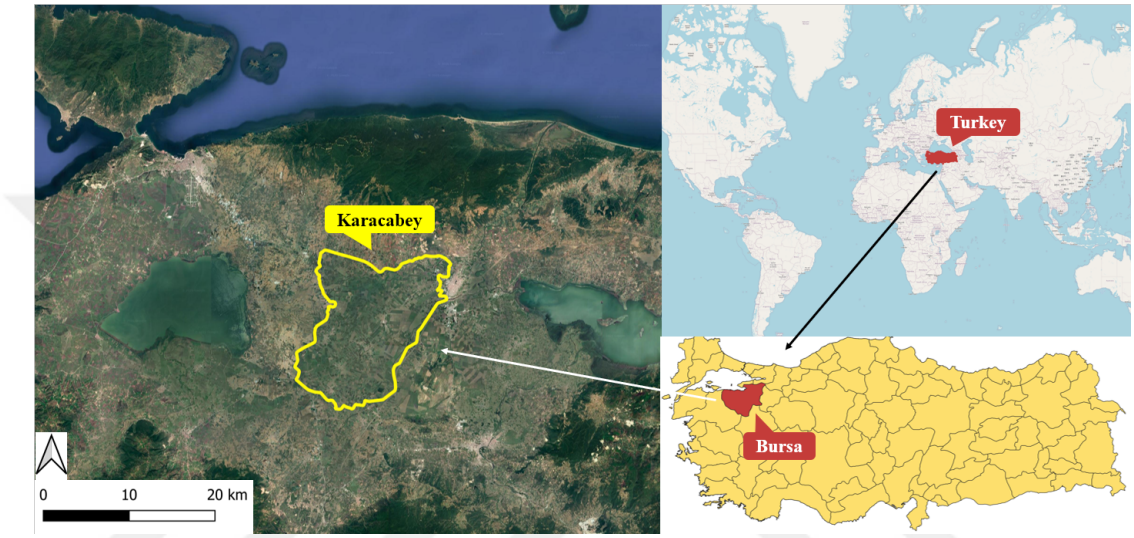


**Figure 6.2 :** The map of the study area located in Karacabey, Bursa, Turkey.

## 6.2 Dataset Used

### 6.2.1 Satellite images

In order to map tomato crop areas, satellite images of PS were used in this study. As explained previously, Ortho Scene products, which are served to the user with geometric and radiometric calibrations [115], were used. Although these images can be downloaded as atmospherically corrected (SR) or ToA corrected, in this study, SR images were preferred for better performance in crop type identification.

According to the tomato cultivation period, 18 different dated cloud- and haze-free PS images were downloaded from Planet Explorer, an online platform that provides easy browsing opportunities on Planet's imagery catalog. In the Planet Explorer, subscribers may search for images over time, have a look at low-resolution satellite image previews, view metadata, and download the types of full-resolution images

[116]. The dates of satellite images used in the study are given in Table 6.1. In some images, two different dates were combined to cover the study area fully.

**Table 6.1 :** Dates of used satellite images used.

| Index | Image Dates | Index | Image Dates |
|---|---|---|---|
| 1 | 18 March 2019 | 10 | 24 June 2019 |
| 2 | 25-26 March 2019 | 11 | 30 June 2019 |
| 3 | 5 April 2019 | 12 | 3-4 July 2019 |
| 4 | 22 April 2019 | 13 | 8-9 July 2019 |
| 5 | 29-30 April 2019 | 14 | 13 July 2019 |
| 6 | 12-13 May 2019 | 15 | 16 July 2019 |
| 7 | 26-28 May 2019 | 16 | 19-21 July 2019 |
| 8 | 30 May 2019 | 17 | 21-23 July 2019 |
| 9 | 31 May 2019 | 18 | 27 July 2019 |

### 6.2.2 Ground truth data

Ground truth data were collected in two ways: fieldwork and visual interpretation. Fieldwork was conducted one time to create a dataset before classification. Visual interpretation was also made only in the office to increase the number of polygons in the test set, but these data were not used for the training set. 70% of the total data set was divided as a training set and 30% as a test set. All of the training data comes from fieldwork; however, 75% of the test set comes from fieldwork and 25% from visual interpretation.

Fieldwork was done with two engineers: an agricultural engineer on-site and a geomatics engineer in the office to plan the fieldwork and arrange the samples to be obtained from the field. In order to conduct fieldwork and collect samples by systematically sampling, the study area was divided into grids of equally sized by using GIS software before the field visits. Grids were implemented into the maps so that the agricultural engineer could use it during the fieldwork. Also, a mobile application was used for the agricultural engineer to draw a polygon in the field and share it with colleagues in the office. Each polygon was checked by up-to-date satellite images and Google Earth Pro. Suspicious polygons were removed from the datasets to prevent misleading results.

Visually interpreted data was obtained by the geomatics engineer using Google Earth Pro based on the samples collected from the fieldwork. The procedure is based on the

recognizable appearances of parcels where different crops are cultivated. The image in Google Earth Pro used was on July 16, 2019, showing the appropriate maturity time to distinguish different crops with their appearance.

The number of parcels for each crop collected by fieldwork and visual interpretation is shown in Table 6.2.

**Table 6.2 :** The number of polygons in both training and test sets.

| Index | Class | Number of Polygons in Training Set | Number of Polygons in Test Set | |
|---|---|---|---|---|
| | | By Fieldwork | by Fieldwork | by Visual Interpretation |
| 1 | Winter Cultivation | 56 | 18 | 6 |
| 2 | Sunflower | 42 | 14 | 4 |
| 3 | Capia Pepper | 65 | 21 | 7 |
| 4 | Paddy | 56 | 18 | 6 |
| 5 | Tomato | 162 | 53 | 17 |
| 6 | Watermelon | 59 | 19 | 6 |
| 7 | Melon | 11 | 4 | 1 |
| 8 | Corn | 95 | 31 | 10 |
| 9 | Orchards | 22 | 8 | 2 |
| 10 | Alfalfa | 48 | 15 | 5 |
| | Total | 616 | 201 | 64 |

## 6.3 Pre-Processing

To obtain more accurate classification results, necessary pre-processing steps were applied to the satellite images. The atmospheric correction step has not been applied because SR products, which are atmospherically corrected images, have been downloaded as described in Section 4.

Image mosaic was required due to the size of both Planet Otho Scene Products and the study area. During the mosaicking of scenes, the attention was paid to the radiometric color balance in the image mosaic. The cutline selection was made considering the minimum difference between cutting regions. Statistics were then calculated for overlapping regions of the scenes, and anomalous values due to various atmospheric conditions such as clouds and haze were eliminated. Color adjustments (i.e., brightness and contrast) were made to minimize the differences between overlapping regions.

## 6.4 Spectral Indices

Widespread and effective VI, NDVI was included in the study to minimize variations caused by different topographic and illumination conditions. [62, 117, 118]. On the

other hand, by adding NDVI images to the classification, it is aimed to obtain more accurate classification results as the size of the feature space increases more.

NDVI was calculated for all dated images. NDVI is the ratio of the differences of 2 spectral bands to the sum. As shown in Equation 6.1, NDVI uses the NIR and red bands in its formula.

$$NDVI = \frac{NIR - RED}{NIR + RED} \tag{6.1}$$

The range of NDVI values is [-1, +1]. NDVI values closer to 1 represents dense vegetation, and closer to -1 represents little or no vegetation. General NDVI values for land surface are given in Table 6.3.

**Table 6.3 :** General NDVI values for various land surface features.

| Land Surface Features | NDVI Ranges |
|---|---|
| Water, snow, built-up areas | $\leq$0 |
| Barren Land | 0 - 0.2 |
| Shrub and Grasslands | 0.2 - 0.3 |
| Sparse Vegetation | 0.3 - 0.5 |
| Dense Vegetation | $\geq$0.5 |

NDVI was calculated for each 18 different dated mosaicked images. Figure 6.3 shows examples of NDVI images of the beginning, mid and late periods of the crop growth cycle. As can be seen, higher values appear brighter, and lower values appear darker. It is clear that in most fields, NDVI values are higher in the period when vegetables are cultivated and grown, that is, in July.

Following the NDVI calculation, NDVI signatures were extracted from the representative field selected for each class (Figure 6.4).

The figure clearly shows that most of the cultivated crops have similar NDVI characteristics over time. The period considered is a typical growth period for mixed horticultural products. Different image features, such as texture explained in the next section, can be integrated into the classification to handle the mixing problem.

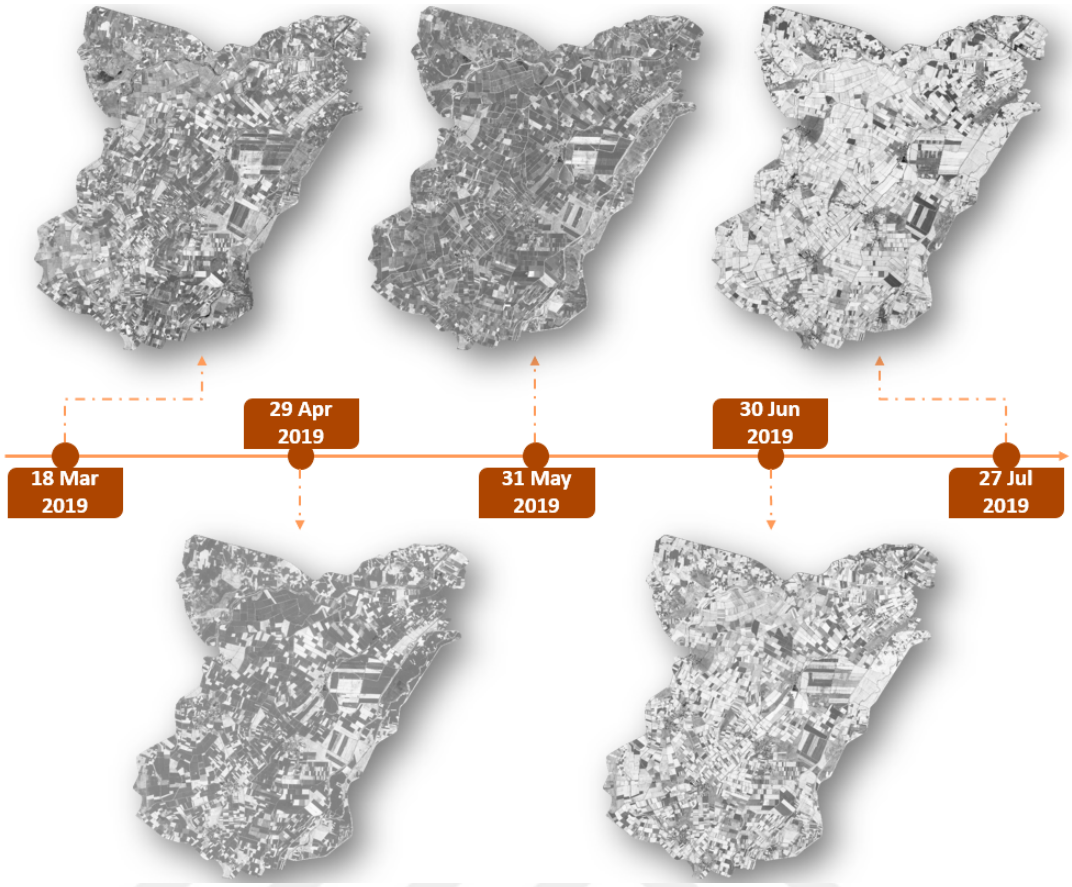


**Figure 6.3 :** Multi-temporal NDVI images.

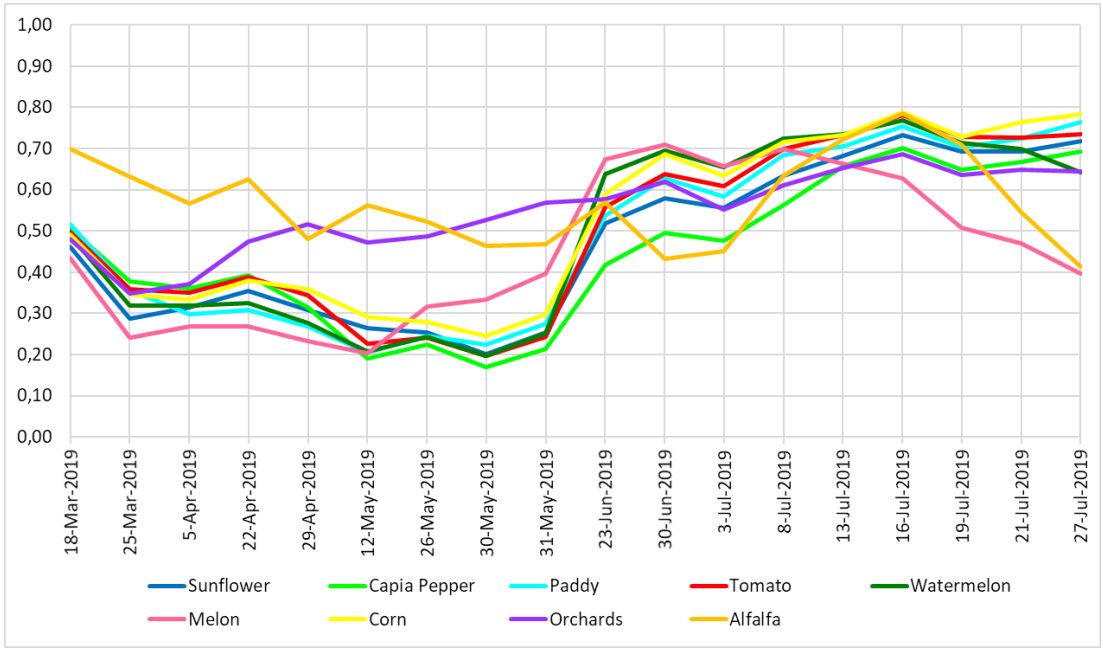


**Figure 6.4 :** NDVI signatures of nine different crops growing in the study area.

## 6.5 Texture Feature Selection

Various textures were analyzed, but three texture features that could contribute to the best discrimination of tomato plants were selected since the use of all texture features would increase data size and computational capacity (Table 6.4).

**Table 6.4 :** An example of the texture features used in the image of 30 July (Red parcels tomato, greens capia pepper, yellows corn, and light blues paddy) [76, 77].

| Textures | Formula | Image Examples | Explanation |
|---|---|---|---|
| ASM | $\sum_{i=1}^{Ng}\sum_{j=1}^{Ng}(p(i,j))^2$<br>p(i, j) is the co-occurance matrix, Ng is the number of discrete intensity levels of the image | 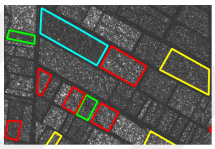 | The homogeneity and the local uniformity of an image is measured by ASM. If the values of the co-occurrence matrix are very similar, ASM values will be higher. |
| Entr | $-\sum_{i=1}^{Ng} p(i)log_2(p(i)+\varepsilon)$<br>e is the arbitrarily small positive number |  | The randomness of an image is measured with Entropy. If the values of the co-occurrence matrix are unequal, the same and small, Entropy values will be higher. |
| MOC2 | $\sqrt{1-e^{-2(HXY_2-HXY)}}$ |  | MOC2 evaluates the correlation between the probability distribution functions. It also measures the complexity of a texture. The result 0 represents independent distributions, which means no mutual information. The maximum value represents entirely dependent distributions, which means utterly dependent information. |

To select the best performing textures, temporal textural changes of each type of crop were plotted in a graph and evaluated considering their possible contribution to the classification. At this point, corn, capia pepper, and watermelon with high mixing potential with tomato class were taken into consideration. As a result of the evaluations, it was determined that the tomato had different texture values from other crops at certain dates for these three textural features (shown in Table 6.4). For

example, as seen in Figure 6.4, tomatoes have had very similar, sometimes even the same “Contrast” values, especially with corn and watermelon. For this reason, the "Contrast" feature has been neglected, as it cannot provide the expected contribution to the classification and may even lead to the mixing of crop classes. Similar analyses were applied to all calculated features, and most of them (shown in Appendix-A.1 and Figure 6.5) were not taken into account because it was thought that they would not improve the classification results.

Meanwhile, textures calculated from NDVI images were found to be more distinctive than those made with individual NIR and red bands. Thus, the texture calculations were applied to NDVI images.

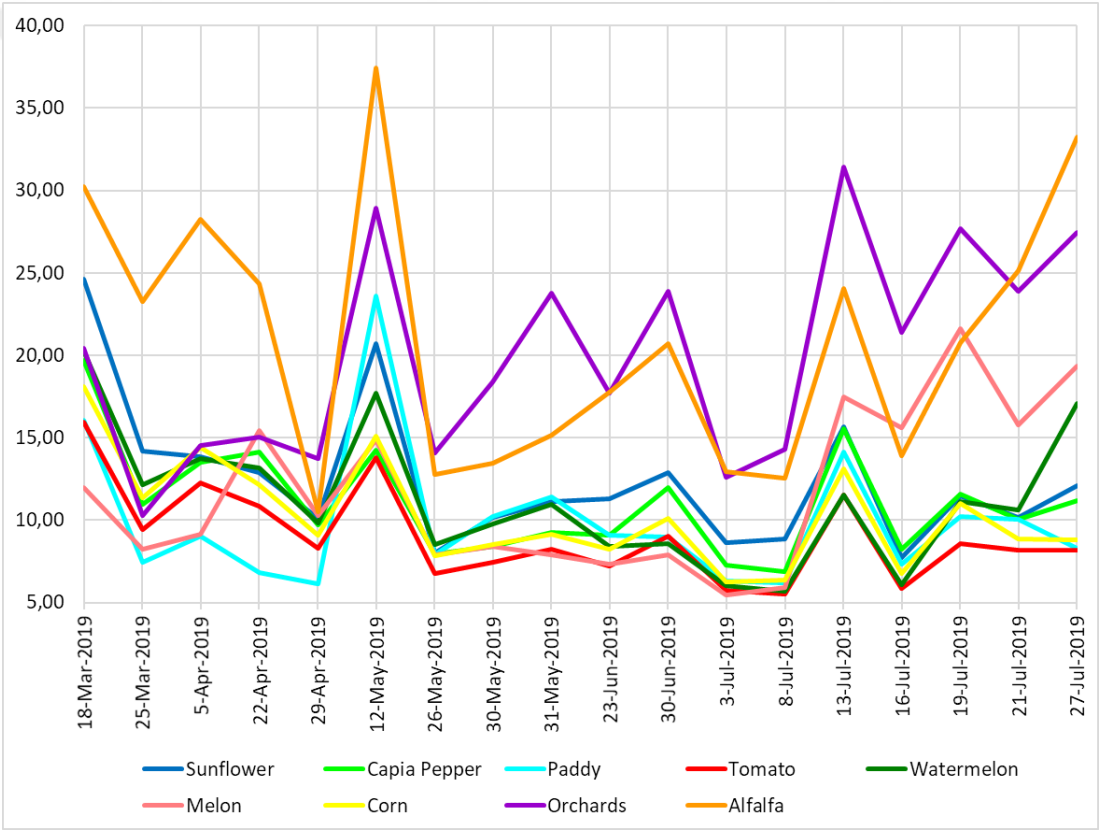


**Figure 6.5 :** Time-series of the “Contrast” feature.

The temporal textural changes of the selected ASM, Entropy, and MOC2 features are shown in Figures 6.6, 6.7, and 6.8. As can be seen in these graphs, the tomato has significantly different ASM, Entropy, and MOC2 values from all other crops, commonly on June 30, 2019, July 3, 2019, and July 27, 2019. Meanwhile, corn, watermelon, and capia pepper appear to be different from tomatoes on three dates.

Especially on May 31, 2019, ASM, Entropy, and MOC2 values of most crop classes are very similar. The reason might be that most of the crops have not yet reached a noticeable plant size and canopy. Plants do not cover the soil before reaching a certain maturity, and therefore soil reflectance may affect pixel values or be dominant. Meanwhile, up to a specific phenological stage, leaves may not have the required size and form to distinguish various plant species.

It can be seen in Figure 6.6 that the ASM values are close to 0. Since ASM represents the homogeneity, low values of ASM indicate that the crop samples are not uniform in themselves. In other words, parcels have complex and dissimilar textures.

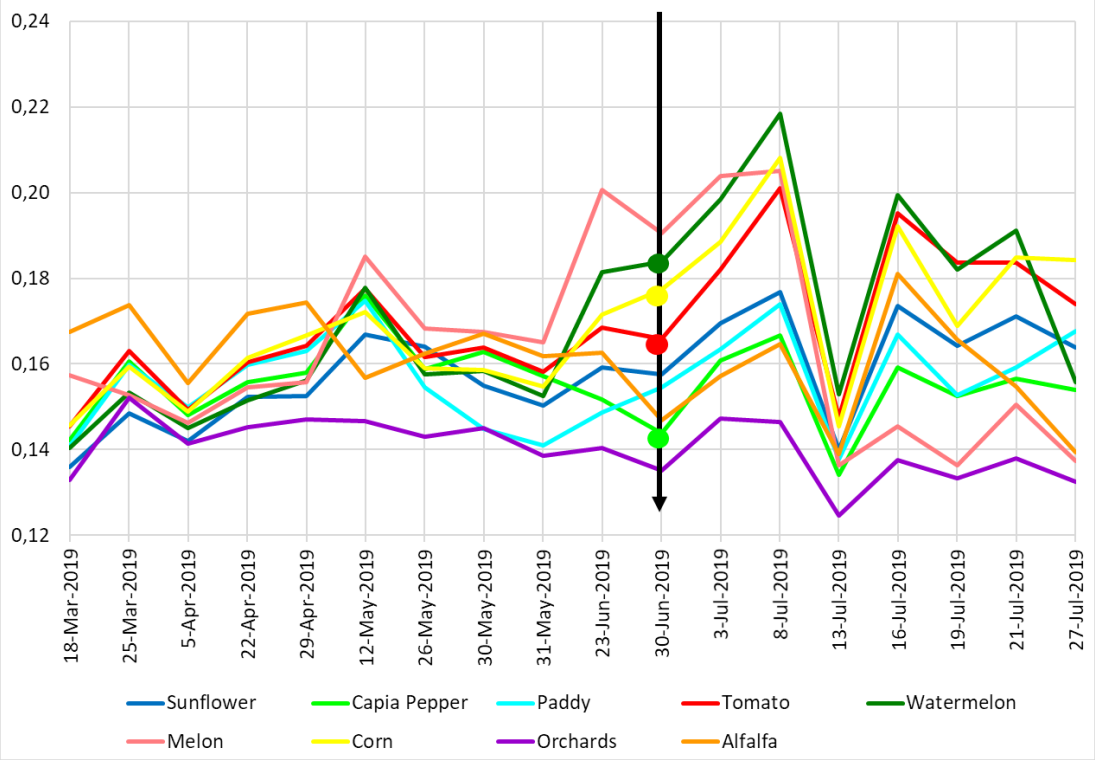


**Figure 6.6 :** Time-series of the "ASM" feature.

As seen in Figure 6.7, relatively high Entropy values strengthen the arguments from low ASM values; in other words, sample polygons show random and inhomogeneous structures in themselves because Entropy is a measure of complexity and randomness. Also, similar texture values of crops observed on the ASM graph before the date May 31, 2019, are also noticeable on the Entropy graph.

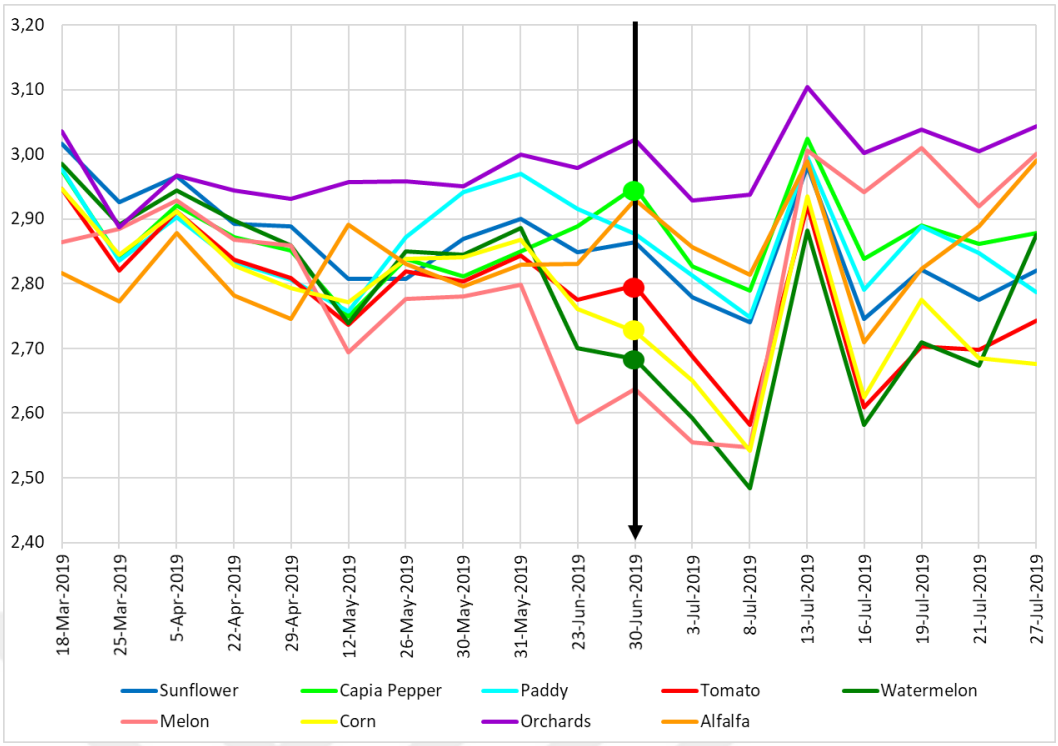


**Figure 6.7 :** Time-series of the “Entropy” feature.

As shown in Figure 6.8, the MOC2 values that indicate non-mutual information in each product are relatively close to zero. It is also difficult to distinguish different crops on May 31, 2019, as MOC2 values were close, as in ASM and Entropy.

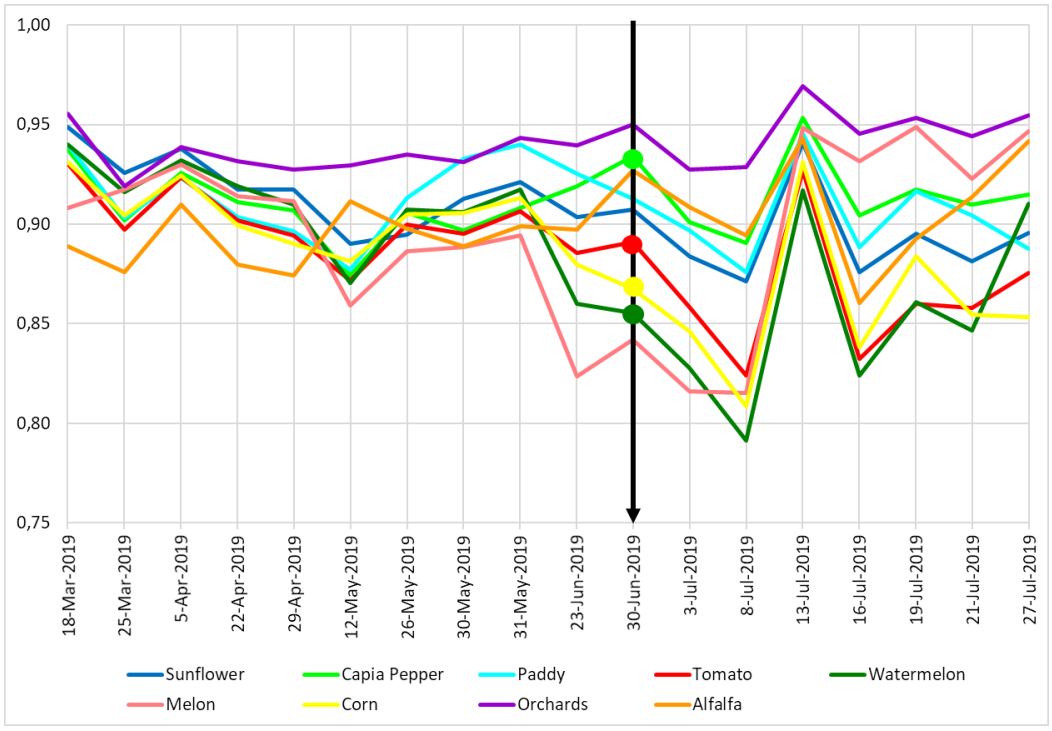


**Figure 6.8 :** Time-series of the “MOC2” feature.

Time series textural features were also used to determine images to be used in mono-temporal classification and also to compare the mono-temporal and multi-temporal classification results. Based on the time-series analyses, one date for mono-temporal classification (June 30, 2019) was selected. In the selection, it was assumed that the two close dates would not yield different classification results.

Therefore, although both dates were considered eligible for mono-temporal classification, the image of 3 July 2019 was discarded due to several days between 30 June 2019. Another reason for the preference is that the image of June 30, 2019, has more significant differences in texture values.

### 6.6 Classification

Image classification is the most critical part of digital image analysis, and many image classification techniques use different approaches. In this study, besides crop mapping, it is also aimed to find answers to particular issues that might be encountered in the classification. One of them is to determine the appropriate image dates to be used the tomato classification. To this end, image classifications were carried out for both the mono-temporal image covering a critical stage of crop growth and multi-temporal images covering certain stages of crop growth. The image dated 30 June 2019 was used in mono-temporal classifications, and 18 multi-date images (Table 6.1) were used in multi-temporal classifications.

Another issue is to determine the effects of different image features on the detection of tomato fields. Thus, NDVI and three textures (i.e., ASM, Entropy, and MOC2) were considered as additional features, and these textures were calculated for the 18 NDVI images. As a final step, all these features were added as a new band to mono-temporal and multi-temporal images, and classifications were made with different band combinations. Thus, as shown in Table 6.5, 18 different combinations were considered in the classification.

Another critical issue in satellite image classification is to determine the reliability of test data and sampling methodology. For this purpose, Bootstrapping was performed to the test data separated from the data collected in the field study and the data collected

**Table 6.5 :** Details of all classifications performed.

| Case # | Image Dates | Features 1 to 4 | Feature 5 | Feature 6 | Feature 7 | Feature 8 |
|---|---|---|---|---|---|---|
| 1 | Mono-Temporal | B/G/R/NIR | | | | |
| 2 | Mono-Temporal | B/G/R/NIR | NDVI | | | |
| 3 | Mono-Temporal | B/G/R/NIR | NDVI | ASM | | |
| 4 | Mono-Temporal | B/G/R/NIR | NDVI | Entropy | | |
| 5 | Mono-Temporal | B/G/R/NIR | NDVI | MOC2 | | |
| 6 | Mono-Temporal | B/G/R/NIR | NDVI | ASM | Entropy | |
| 7 | Mono-Temporal | B/G/R/NIR | NDVI | ASM | MOC2 | |
| 8 | Mono-Temporal | B/G/R/NIR | NDVI | Entropy | MOC2 | |
| 9 | Mono-Temporal | B/G/R/NIR | NDVI | ASM | Entropy | MOC2 |
| 10 | Multi-Temporal | B/G/R/NIR | | | | |
| 11 | Multi-Temporal | B/G/R/NIR | NDVI | | | |
| 12 | Multi-Temporal | B/G/R/NIR | NDVI | ASM | | |
| 13 | Multi-Temporal | B/G/R/NIR | NDVI | Entropy | | |
| 14 | Multi-Temporal | B/G/R/NIR | NDVI | MOC2 | | |
| 15 | Multi-Temporal | B/G/R/NIR | NDVI | ASM | Entropy | |
| 16 | Multi-Temporal | B/G/R/NIR | NDVI | ASM | MOC2 | |
| 17 | Multi-Temporal | B/G/R/NIR | NDVI | Entropy | MOC2 | |
| 18 | Multi-Temporal | B/G/R/NIR | NDVI | ASM | Entropy | MOC2 |

from visual interpretation. At the end, the accuracy and reliability of the classification accuracy was evaluated.

In the meantime, how accurate the classification results can be evaluated without separate test data; that is, only training data is another research topic considered in this research. Training data is a requirement of RF classification. Ideally, reference data collected from fieldwork should be split independently into training and test data to evaluate accuracy more reliably. However, collecting the required amount of data reliably and quickly from the field is a costly and challenging task.

In this study, after collecting ground-truth data for the different crops grown in the region, the training set to be used in the classification and the test set to be used in the accuracy assessment are handled independently to obtain a more accurate classification result. However, considering the challenges of fieldwork, a second approach has been evaluated based on the assumption that it may not be possible to create such extensive data sets under all circumstances. In this approach, it was assumed that there was no separate test data; that is, both classification and accuracy evaluation were made with a single data set.

Based on these assumptions, three different classification and accuracy assessment scenarios were considered using 18 different data sets (Table 6.4), and the methodology used in these three scenarios is given in the flow chart shown in Figure 6.9. In the first scenario, traditional RF classification was performed with the training data, and the results were evaluated with separate test data. In the second scenario, the same procedure was applied with the first scenario; then, the sampling methodology was evaluated with Bootstrapping. Finally, in the third scenario, the data collected from the field were not separated as training and test, but are combined into a single set. Using the Stratified K-Fold CV, RF was both trained and evaluated with the combined dataset. 18 classification results were compared for each scenario.

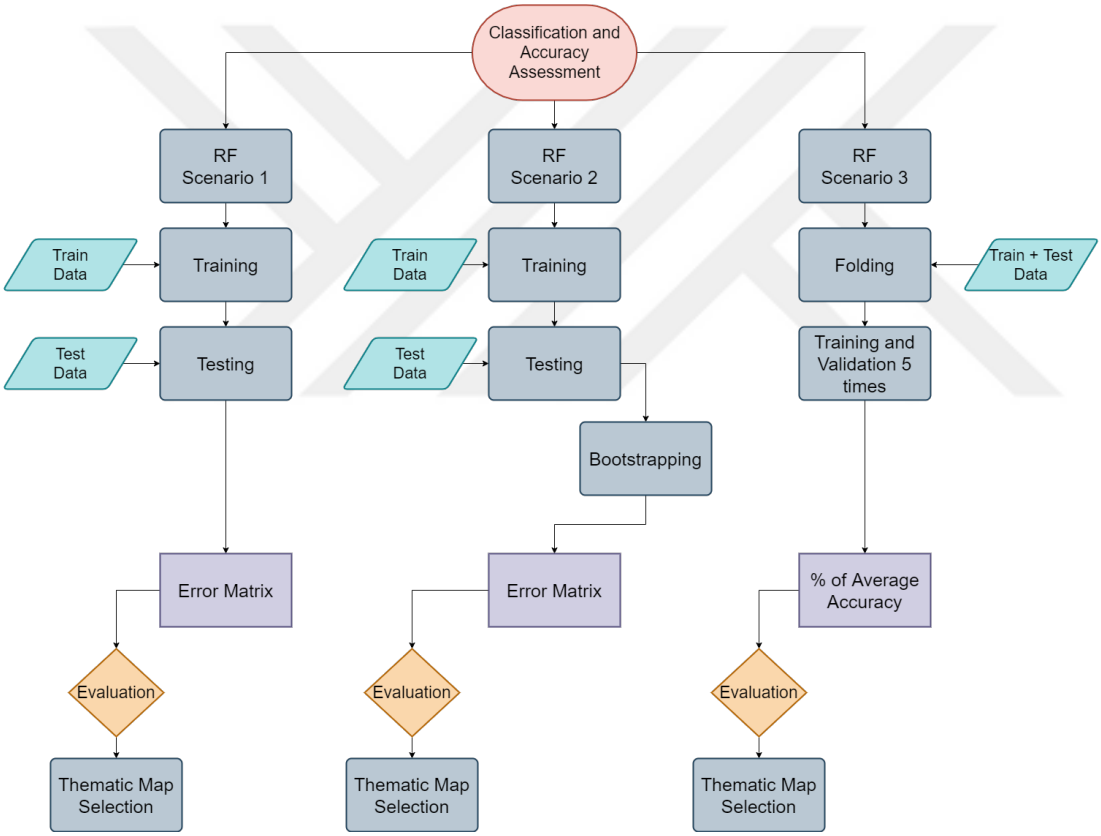


**Figure 6.9 :** The methodology used in three types of classification & accuracy assessment scenarios.

### 6.6.1 RF classification scenario 1

For the first analysis, pixel-based and supervised RF classification was performed for each classification cases given in Table 6.5 with the training data collected from the fieldwork. The input parameters of the algorithm are given in Table 6.6.

**Table 6.6 :** Input parameters of the RF algorithm.

| RF Input Parameters | Values |
|---|---|
| Prediction Variables | Variables given in Table 6.6 |
| Response Variables | 762 Polygons for 13 Land Cover Class |
| No of Trees | 1000 |
| Balanced Subsample | True |
| Random State | 1773 |

Then, the results were traditionally evaluated for tomato and not-tomato by using the separate test dataset. The accuracy results for each classification of scenario 1 are shown in Table 6.7 graphically in Figure 6.10.

**Table 6.7 :** The accuracy results for each classification of Scenario 1.

| Case # | Image Dataset | Features 1 to 4 | Feature 5 | Feature 6 | Feature 7 | Feature 8 | Mean |
|---|---|---|---|---|---|---|---|
| 1 | Mono-Temporal | B/G/R/NIR | | | | | 0,824 |
| 2 | Mono-Temporal | B/G/R/NIR | NDVI | | | | 0,824 |
| 3 | Mono-Temporal | B/G/R/NIR | NDVI | ASM | | | 0,827 |
| 4 | Mono-Temporal | B/G/R/NIR | NDVI | Entropy | | | 0,827 |
| 5 | Mono-Temporal | B/G/R/NIR | NDVI | MOC2 | | | 0,827 |
| 6 | Mono-Temporal | B/G/R/NIR | NDVI | ASM | Entropy | | 0,828 |
| 7 | Mono-Temporal | B/G/R/NIR | NDVI | ASM | MOC2 | | 0,827 |
| 8 | Mono-Temporal | B/G/R/NIR | NDVI | Entropy | MOC2 | | 0,827 |
| 9 | Mono-Temporal | B/G/R/NIR | NDVI | ASM | Entropy | MOC2 | 0,827 |
| 10 | Multi-Temporal | B/G/R/NIR | | | | | 0,924 |
| 11 | Multi-Temporal | B/G/R/NIR | NDVI | | | | 0,926 |
| 12 | Multi-Temporal | B/G/R/NIR | NDVI | ASM | | | 0,928 |
| 13 | Multi-Temporal | B/G/R/NIR | NDVI | Entropy | | | 0,927 |
| 14 | Multi-Temporal | B/G/R/NIR | NDVI | MOC2 | | | 0,928 |
| 15 | Multi-Temporal | B/G/R/NIR | NDVI | ASM | Entropy | | 0,929 |
| 16 | Multi-Temporal | B/G/R/NIR | NDVI | ASM | MOC2 | | 0,928 |
| 17 | Multi-Temporal | B/G/R/NIR | NDVI | Entropy | MOC2 | | 0,928 |
| 18 | Multi-Temporal | B/G/R/NIR | NDVI | ASM | Entropy | MOC2 | 0,929 |

Mono-temporal RF results showed that the addition of GLCM features increased the accuracy, but NDVI did not. The combination of NDVI, ASM, and Entropy yielded the best mono-temporal classification in Scenario 1, with a slight increase of 0.004. The thematic map of case 6 is shown in Figure 6.11.

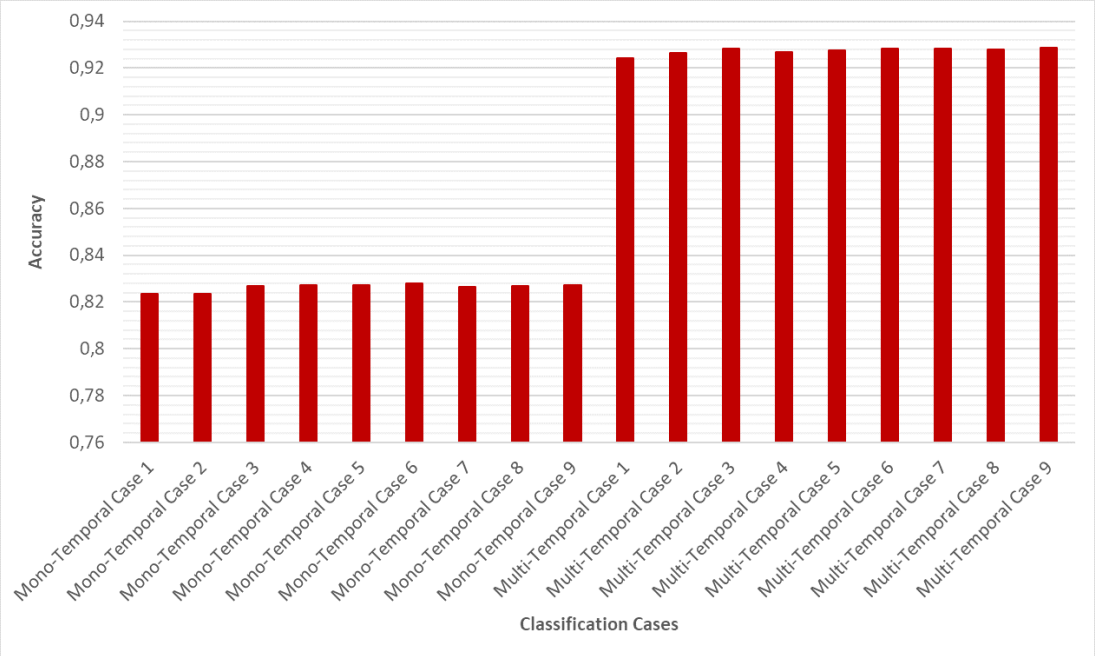


**Figure 6.10 :** Graphic representation of RF classification scenario 1 results.

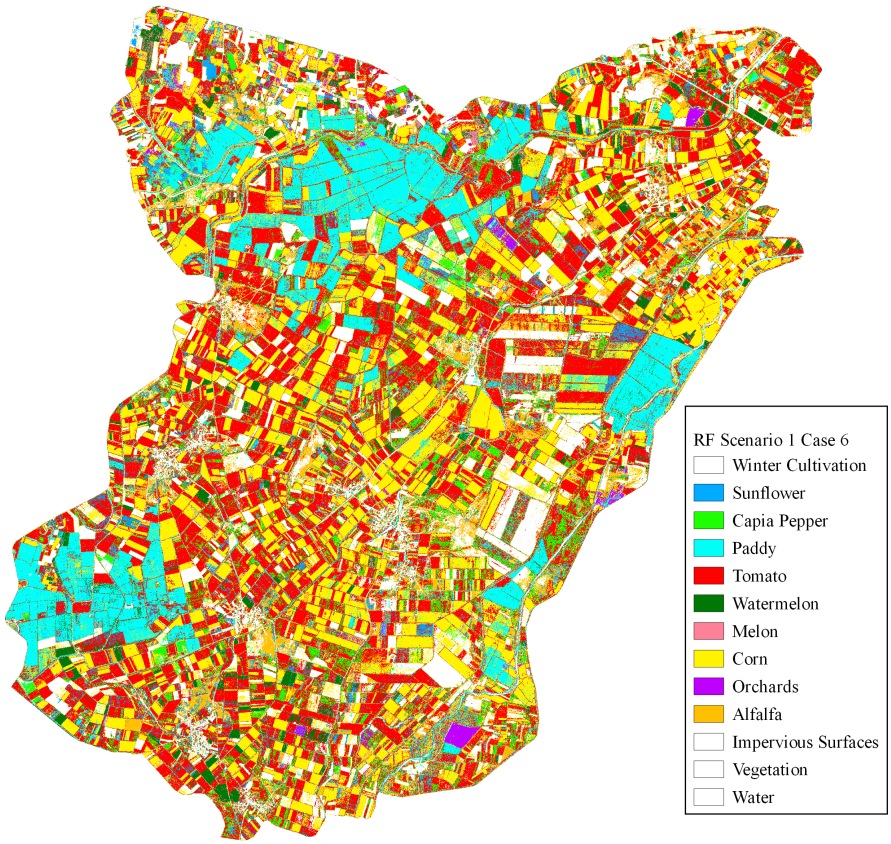


**Figure 6.11 :** The best mono-temporal RF classification case for scenario 1.

On the other hand, similar results were observed in the multi-temporal RF classification. The best accuracy was obtained in combination with NDVI, ASM, and Entropy, again with an increase of 0.005. However, the same accuracy value is also seen in the 18th classification. This indicates that MOC2 does not provide any valuable information to the multi-temporal classification in scenario 1. The thematic map of case 15 is shown in Figure 6.12.

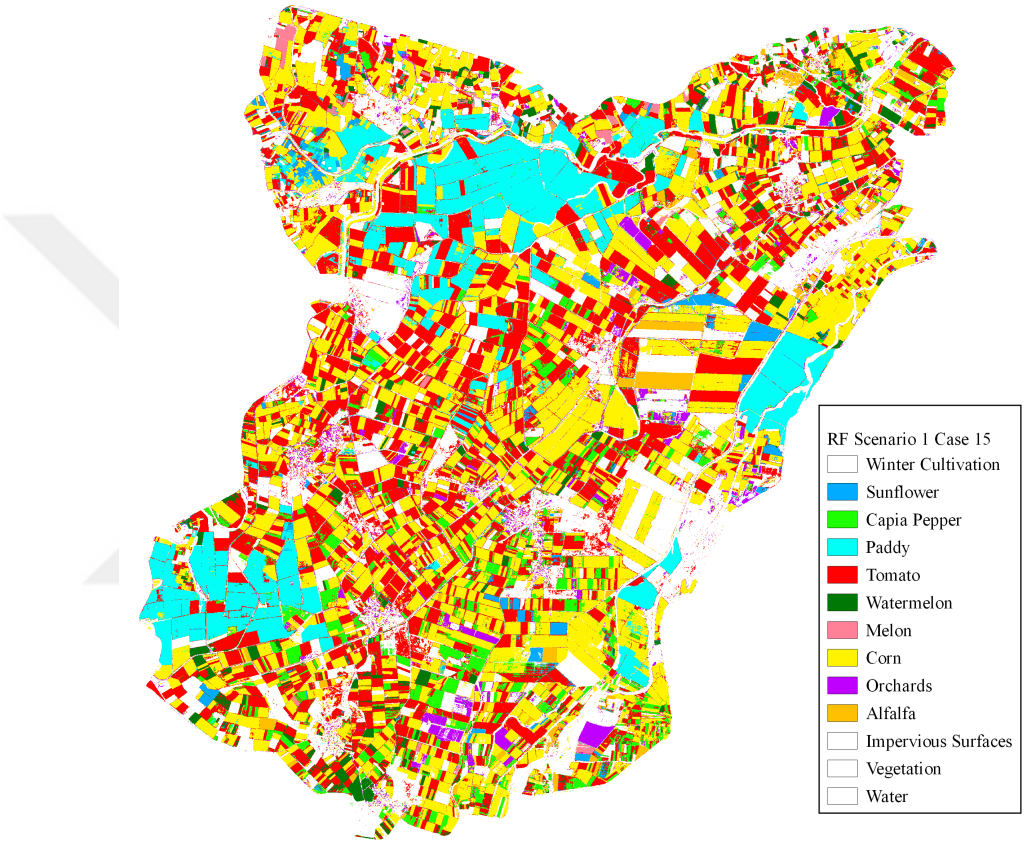


**Figure 6.12 :** The best multi-temporal RF classification case for scenario 1.

Finally, when mono- and multi-temporal classifications are compared (Figure 6.9), the accuracy of the multi-temporal RF classification appears to be 0.100 higher. Also, a multi-temporal classification map has less salt and pepper effect than a mono-temporal classification map and therefore looks smoother and clearer. Therefore, it is concluded that multi-temporal data should be preferred for high accuracy tomato classification with conventional RF.

### 6.6.2 RF classification scenario 2

The same procedure, parameters, and data used in the first scenario was also used in the second scenario. However, the Bootstrapping process was performed to test data as an additional step. This process was applied to determine how much the test data represents the whole region and the compatibility of classification accuracy with the real world. Before the Bootstrapping, two parameters were determined: sample size and repetition number. When the sample size increases, the algorithm can eliminate errors caused by random sampling. The sample size can be equal to the test size as a maximum. In the meantime, the lower number of repetitions may cause deviations. Accordingly, the sample size is determined as its maximum, which equals the number of polygons in the test set. However, since it is a pixel-based application, individual pixels were taken into account in Bootstrapping. Thus, the number of pixels used was changed depending on the number of pixels in the selected polygons. Besides, the number of repeats was selected as 1000.

In some studies, the increase in the number of parameters may be a problem as it increases the required processing capacity of computers, but the hardware/software used in this study was appropriately selected to handle all scenarios. The properties of the computer units used in this study are given in Table 6.8.

**Table 6.8 :** The properties of the computer units used in this study.

| Computer Units | Properties |
|---|---|
| Motherboard Memory | 128 GB |
| Central Processing Unit (CPU) Generation | 9th |
| Number of Processor Cores | 10 |
| Max. Processor Memory | 128 GB |
| RAM Capacity | 32 GB |
| Graphics Processing Unit (GPU) Memory | 11 GB |
| GPU Bits | 352 bit |
| CPU Freezer | Used |

Table 6.9 shows the Bootstrapping results with 1000 repetitions of the RF classification with the confidence intervals.

**Table 6.9 :** The accuracy results for each classification of Scenario 2.

| Case # | Image Dataset | Features 1 to 4 | Feature 5 | Feature 6 | Feature 7 | Feature 8 | Confidence Interval | |
|---|---|---|---|---|---|---|---|---|
| | | | | | | | Lowest | Highest |
| 1 | Mono-Temporal | B/G/R/NIR | | | | | 0,786 | 0,860 |
| 2 | Mono-Temporal | B/G/R/NIR | NDVI | | | | 0,786 | 0,860 |
| 3 | Mono-Temporal | B/G/R/NIR | NDVI | ASM | | | 0,789 | 0,863 |
| 4 | Mono-Temporal | B/G/R/NIR | NDVI | Entropy | | | 0,790 | 0,863 |
| 5 | Mono-Temporal | B/G/R/NIR | NDVI | MOC2 | | | 0,789 | 0,863 |
| 6 | Mono-Temporal | B/G/R/NIR | NDVI | ASM | Entropy | | 0,790 | 0,864 |
| 7 | Mono-Temporal | B/G/R/NIR | NDVI | ASM | MOC2 | | 0,789 | 0,863 |
| 8 | Mono-Temporal | B/G/R/NIR | NDVI | Entropy | MOC2 | | 0,788 | 0,863 |
| 9 | Mono-Temporal | B/G/R/NIR | NDVI | ASM | Entropy | MOC2 | 0,789 | 0,863 |
| 10 | Multi-Temporal | B/G/R/NIR | | | | | 0,893 | 0,950 |
| 11 | Multi-Temporal | B/G/R/NIR | NDVI | | | | 0,896 | 0,953 |
| 12 | Multi-Temporal | B/G/R/NIR | NDVI | ASM | | | 0,899 | 0,954 |
| 13 | Multi-Temporal | B/G/R/NIR | NDVI | Entropy | | | 0,897 | 0,953 |
| 14 | Multi-Temporal | B/G/R/NIR | NDVI | MOC2 | | | 0,897 | 0,953 |
| 15 | Multi-Temporal | B/G/R/NIR | NDVI | ASM | Entropy | | 0,899 | 0,954 |
| 16 | Multi-Temporal | B/G/R/NIR | NDVI | ASM | MOC2 | | 0,898 | 0,954 |
| 17 | Multi-Temporal | B/G/R/NIR | NDVI | Entropy | MOC2 | | 0,897 | 0,954 |
| 18 | Multi-Temporal | B/G/R/NIR | NDVI | ASM | Entropy | MOC2 | 0,898 | 0,955 |

In the mono-temporal classification, the narrowest confidence interval is observed in the 4th classification, with a difference of 0.073. Generally, in the mono-temporal classifications of the second scenario, RF results are in the confidence interval of approximately 7%. For example, in the 6th classification case, which is the best result selected in scenario 1, the confidence interval is 7.4%, and its Bootstrapping histogram is shown in Figure 6.13. Close confidence intervals of the mono-temporal RF results indicate that the test data are consistent within themselves, and the accuracy results are significant and reliable.

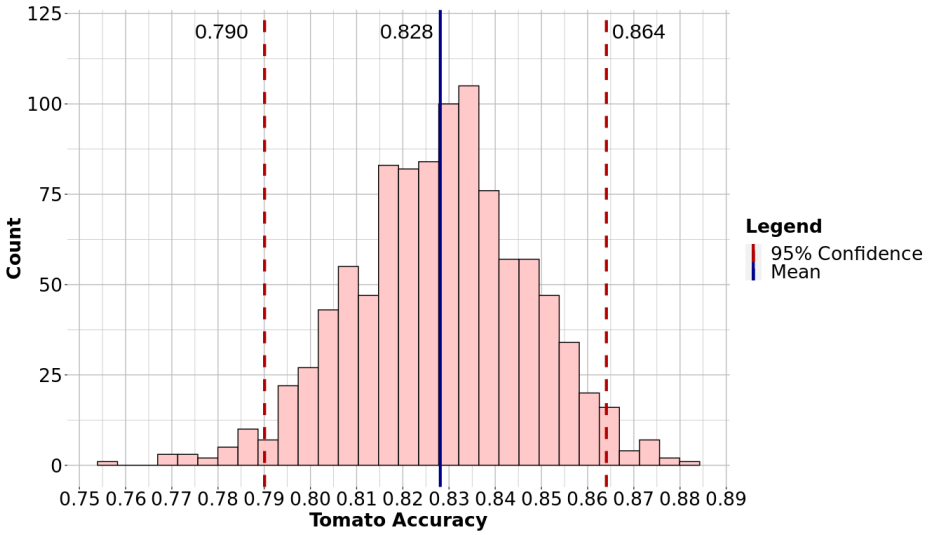


**Figure 6.13 :** Bootstrapping histogram with average accuracy and confidence intervals for the 6th classification case.

An alluvial diagram is used to visualize changes between classified and actual types of crops in network structure over time. In this type of flow diagram, variables are assigned to parallel vertical axes, and values are represented in each axis by blocks. As an example, an alluvial diagram of case 6 is shown in Figure 6.14. In the diagram, left and right vertical axes represent classification results and actual crop types, respectively. As seen in the figure, tomato was mostly mixed with capia pepper and sunflower. In other words, fields that are actually tomatoes were mostly classified as capia peppers and sunflowers. It then mixed with corn, watermelon and winter cultivation parcels.

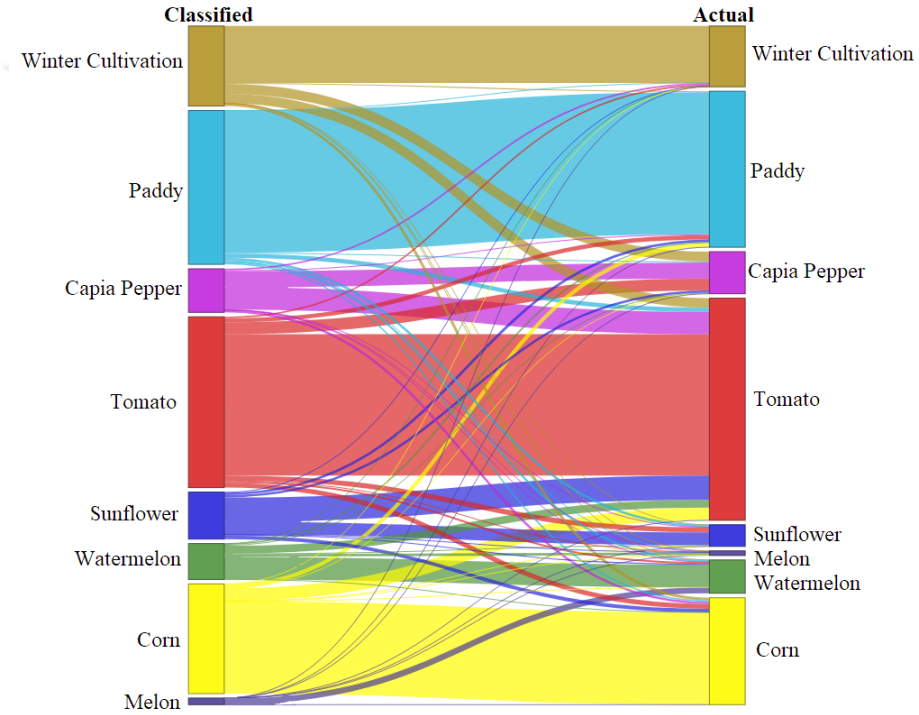


**Figure 6.14 :** Alluvial diagram of case 6.

Multi-temporal RF results of scenario 2 verify the multi-temporal RF results of scenario 1, i.e., the narrowest confidence interval was obtained for the 15th classification, and its histogram is shown in Figure 6.15. However, the difference between the 15th classification and other multi-temporal classifications is 0.001-0.002. All other Bootstrapping histograms are given in Appendix-B.2. However, when the mono-temporal RF and multi-temporal RF are compared, it appears that the confidence interval has shrunk by about 2%, thereby increasing the consistency and reliability of the results.

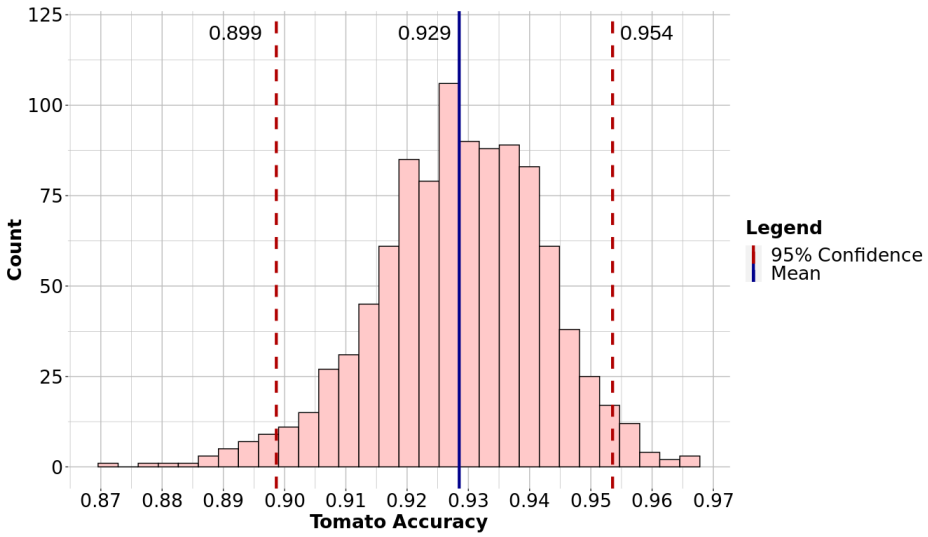


**Figure 6.15 :** Bootstrapping histogram with average accuracy and confidence intervals for the 15th classification case.

Figure 6.16 shows the alluvial diagram of case 15. In this case, the most mixed crops with tomato were sunflower, capia pepper, and watermelon. Compared with the results of the mono-temporal classification, the crop mixing problem appears to be significantly reduced. At the same time, the multi-temporal classification alluvial diagram shows that the misclassifications between tomato, corn, and winter cultivation parcels observed in mono-temporal classification have almost disappeared.

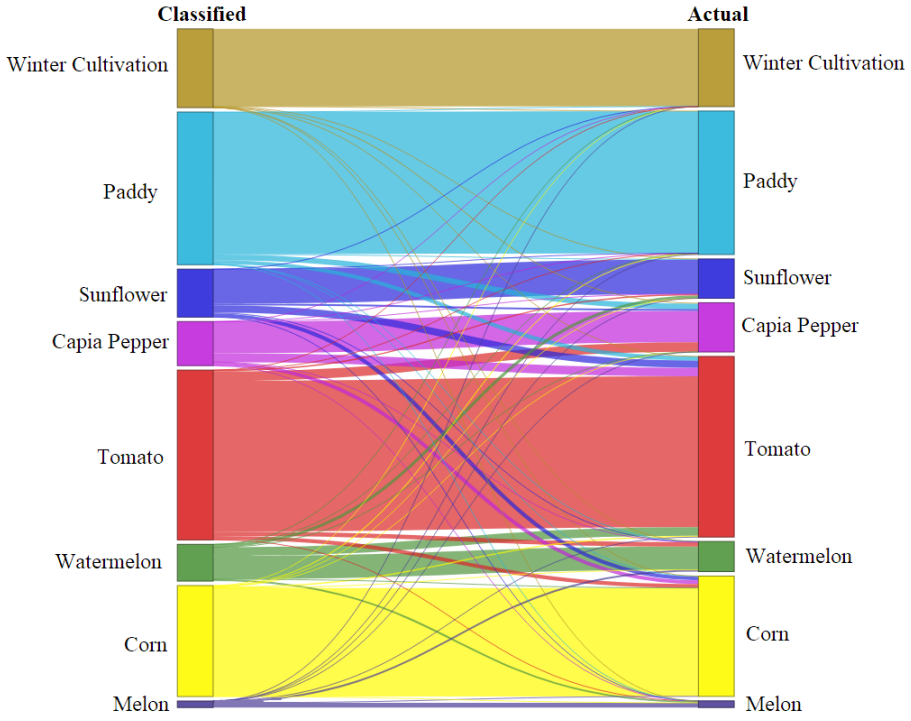


**Figure 6.16 :** Alluvial diagram of case 15.

In conclusion, it is possible to say that using multi-temporal images improves classification accuracy and significantly prevents misclassification, according to accuracy results, confidence intervals, and alluvial diagrams.

### 6.6.3 RF classification scenario 3

In the third scenario, RF Classification and Stratified K-Fold CV for each classification given in Table 6.5 was performed with the combination of training and test sets. In this analysis, the model was both trained and validated simultaneously using only a composite data set, assuming no test data.

First, a fold value was assigned to each polygon in the dataset. By setting the fold number to five, each class is divided into five with equal weights. Then, pixel samples were taken from each class. The locations of the sample pixels were saved, and the same pixels were selected for each classification. Thus, the RF was forced only once to make a random selection, thereby preventing the results from affecting the different samples taken.

Afterward, each fold was excluded, respectively, and the model was trained with the selected pixels in the remaining fours. Classification was performed with sample pixels from four-folds, and the validation was evaluated with the sampled pixels from the excluded fold. This process was repeated five times until the verification was done with all the folds, and the average of their accuracies was obtained to get the final CV accuracy result. Results of mono- and multi-temporal classifications are given in Table 6.10.

Mono-temporal CV results showed that all RF accuracies were approximately the same. It can easily be seen in Table 6.10 that there is a difference between 0.001-0.005 that can be neglected between all the accuracies. However, the most significant difference was found with the addition of Entropy texture.

Producer's and User's Accuracies show a maximum of 0.010 variation across all multi-temporal classifications. The difference is higher in multi-temporal classification than the difference in mono-temporal. However, the highest Overall Accuracy was achieved in the15th classification when NDVI, ASM, and Entropy were added.

**Table 6.10 :** The accuracy results for each classification of Scenario 3.

| Case # | Image Dataset | Features 1 to 4 | Feature 5 | Feature 6 | Feature 7 | Feature 8 | Producer's Accuracy | User's Accuracy | Overall Accuracy | Tomato Specificity |
|---|---|---|---|---|---|---|---|---|---|---|
| 1 | Mono-Temporal | B/G/R/NIR | | | | | 0,724 | 0,559 | 0,782 | 0,841 |
| 2 | Mono-Temporal | B/G/R/NIR | NDVI | | | | 0,722 | 0,560 | 0,782 | 0,843 |
| 3 | Mono-Temporal | B/G/R/NIR | NDVI | ASM | | | 0,721 | 0,565 | 0,783 | 0,846 |
| 4 | Mono-Temporal | B/G/R/NIR | NDVI | Entropy | | | 0,722 | 0,567 | 0,784 | 0,847 |
| 5 | Mono-Temporal | B/G/R/NIR | NDVI | MOC2 | | | 0,721 | 0,565 | 0,783 | 0,846 |
| 6 | Mono-Temporal | B/G/R/NIR | NDVI | ASM | Entropy | | 0,721 | 0,566 | 0,784 | 0,847 |
| 7 | Mono-Temporal | B/G/R/NIR | NDVI | ASM | MOC2 | | 0,721 | 0,566 | 0,784 | 0,846 |
| 8 | Mono-Temporal | B/G/R/NIR | NDVI | Entropy | MOC2 | | 0,721 | 0,566 | 0,784 | 0,847 |
| 9 | Mono-Temporal | B/G/R/NIR | NDVI | ASM | Entropy | MOC2 | 0,722 | 0,566 | 0,784 | 0,847 |
| 10 | Multi-Temporal | B/G/R/NIR | | | | | 0,852 | 0,799 | 0,896 | 0,941 |
| 11 | Multi-Temporal | B/G/R/NIR | NDVI | | | | 0,857 | 0,796 | 0,898 | 0,939 |
| 12 | Multi-Temporal | B/G/R/NIR | NDVI | ASM | | | 0,862 | 0,791 | 0,899 | 0,937 |
| 13 | Multi-Temporal | B/G/R/NIR | NDVI | Entropy | | | 0,863 | 0,793 | 0,900 | 0,937 |
| 14 | Multi-Temporal | B/G/R/NIR | NDVI | MOC2 | | | 0,862 | 0,791 | 0,899 | 0,936 |
| 15 | Multi-Temporal | B/G/R/NIR | NDVI | ASM | Entropy | | 0,863 | 0,794 | 0,901 | 0,938 |
| 16 | Multi-Temporal | B/G/R/NIR | NDVI | ASM | MOC2 | | 0,862 | 0,790 | 0,899 | 0,936 |
| 17 | Multi-Temporal | B/G/R/NIR | NDVI | Entropy | MOC2 | | 0,861 | 0,787 | 0,898 | 0,936 |
| 18 | Multi-Temporal | B/G/R/NIR | NDVI | ASM | Entropy | MOC2 | 0,862 | 0,789 | 0,899 | 0,936 |

Meanwhile, it can be seen in Appendix-C.1 that thematic maps of each fold are different for 4th and 15th classification cases. Small differences showed that some polygons are important to train the model and change the results. Accordingly, it was concluded that CV can be used to detect critical parcels and most mixed crops for sample selection and more accurate classification results.

The alluvial diagram of case 4 is shown in Figure 6.17. The diagram shows that the crop most mixed with tomato is capia pepper in CV. Then comes sunflower and corn.

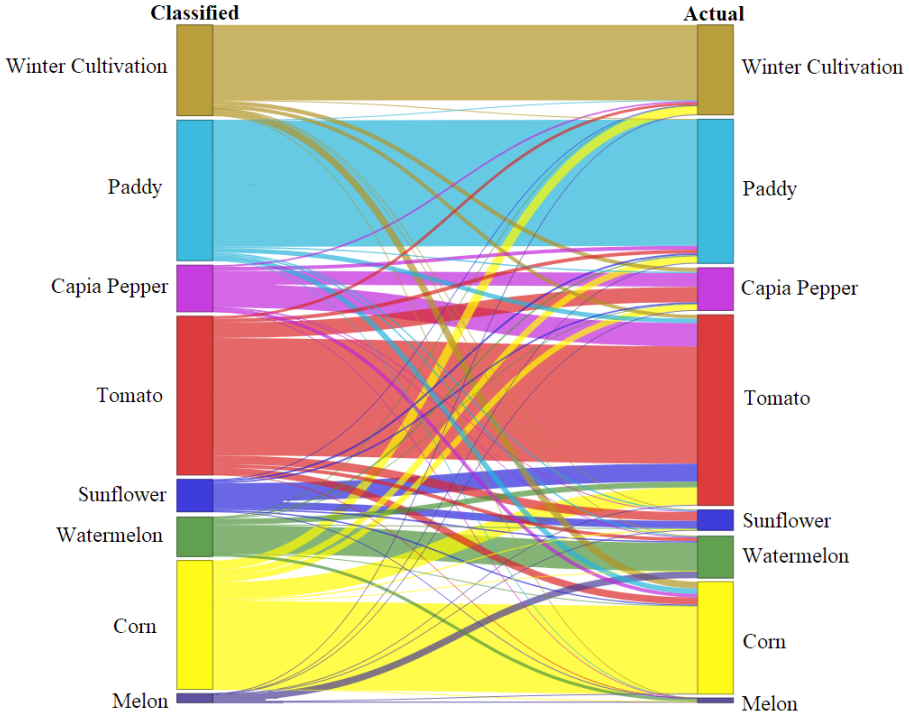


**Figure 6.17 :** Alluvial diagram of scenario 3, case 4.

The alluvial diagram of case 15 is shown in Figure 6.18. In the diagram, it can be seen that when compared to mono-temporal classification, misclassifications decrease with multi-temporal classification. In addition, it was once again confirmed that the use of multi-temporal images improved classifications.

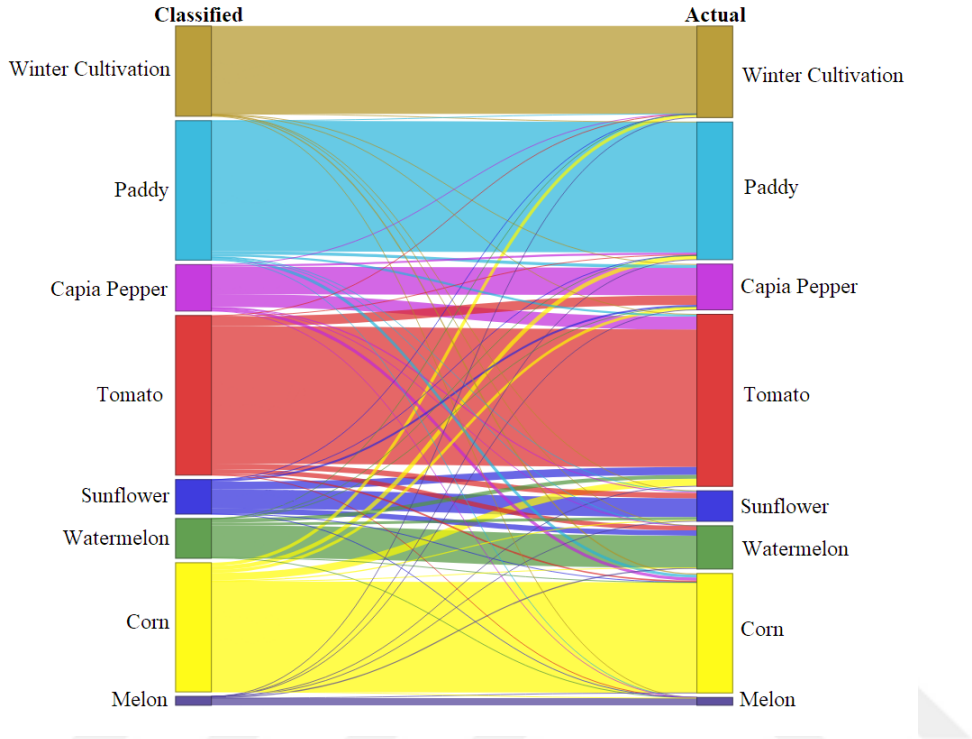


**Figure 6.18 :** Alluvial diagram of RF classification scenario 3, case 15.

# 7. CONCLUSIONS

Agriculture, which is associated with the production of essential food crops, plays a vital role in the growth of each country. Given its role in both fresh consumption and industrial production, one of these basic products is tomato; hence accurate mapping of the tomatoes cultivated areas is crucial for agriculture-based countries such as Turkey. For this reason, in this study, it was aimed to determine tomato cultivation areas with high accuracy in which there are not many studies in the literature. Undoubtedly, detection and mapping of the tomato cultivation areas before harvest will provide ministries and agricultural stakeholders with a perspective that enables appropriate agricultural planning in the actions to be taken.

Since the agricultural activities are intense in the Karacabey plain, Karacabey, a district of Bursa, was selected as the study area. Karacabey is fourth in the ranking of industrial tomato cultivation by supplying Turkey's %40 of tomato needs with 140.000 da area of industrial tomato cultivation, and tomato paste production factories producing annually 181.651-ton tomato paste. Besides tomato, other crops such as wheat, barley, corn, beans, peas, sugar beet, cotton, sunflower, and tobacco are the most commonly cultivated crops in Karacabey plain. However, it is still challenging to identify and map tomato-cultivated parcels using satellite images, because the spectral reflection of various plants appears to be similar because they have all green plant parts, and these similarities cause spectral overlaps. In other words, since it is challenging to distinguish crops from each other using only multi-spectral information, thematic mapping was done using multi-temporal data, along with additional features such as spectral indices and textures.

In addition to detecting and mapping of tomato cultivated areas, this study aims to clarify particular issues encountered during classification. The first one is to determine the best performing period of tomato for the classification in Karacabey. For this purpose, RF classifications were performed with mono-temporal and multi-temporal PS images that representing a particular stage of tomato growth and covering a

specified period of tomato growth, respectively. 30 June 2019 was selected for mono-temporal, and 18 dates were chosen for multi-temporal classifications. The second issue is to evaluate the contributions and the necessity of image features used in tomato classification, which are NDVI and ASM, Entropy, MOC2 textures. Therefore, all the features were calculated and added as a new band to both mono- and multi-temporal image classifications with different band combinations. Thus, 18 combinations were considered in the classifications performed. The last issue is to discover the reliability of test data and sampling methodology. To achieve this, three different classification and accuracy assessment scenarios were implemented using 18 combinations of mono- and multi-temporal images, which are briefly i) RF classifications with training data, ii) RF classification and then Bootstrapping for test data, iii) a Stratified K-Fold CV to train and validate RF.

The main results obtained in this study are summarized as follows:

- The use of multi-temporal data provided a 10-14% increase in the classification results. Also, it has been observed that the use of multi-temporal data shrinks the confidence interval and provides more consistent and reliable results. Therefore, the use of multi-temporal data covering the phenological growth cycle has yielded more accurate results than mono-temporal data.

- Almost all the results of mono- and multi-temporal classification scenarios were shown that using NDVI, ASM, and especially Entropy increases the classification accuracy between 0,002-0,005 and shrinks the confidence interval by 0,004. The classification process used in this thesis, when applied to wider tomatoes cultivated areas throughout Turkey, it is thought that this small increase will lead to major improvements in crop mapping. On the other hand, MOC2, another texture parameter used in the study, did not contribute much to the classification results as expected; in other words, it was found ineffective in most cases. NDVI, on the other hand, has generally improved the results, but it did not increase accuracies in all cases. In conclusion, using NDVI and GLCM features increased the accuracy gradually by 1-2% as expected. However, although some image features positively affect all results in this study, it should not be generalized.

- In three different classification and accuracy assessment scenarios performed, it was observed that the test data were consistent, and the classification results were reliable in the assessment made with Bootstrapping. Therefore, it has been concluded that the use of Bootstrapping, which has become a popular method, is particularly useful in thematic mapping. In addition, no changes were observed in the combination of different features selected when applying the CV, but the accuracy of the best result was reduced by 3-5%. Although there are differences in accuracy results, it is seen that CV does not give misleading results and can be preferred when there is not enough data to be divided for testing.

In conclusion, considering all the applications made within the scope of this study, the tomato cultivation area was determined with a maximum accuracy of 93% within the 5% confidence interval by using multi-temporal PS satellite images.

Findings from this thesis may lead to some valuable suggestions below for similar applications in the future.

- In this study, Planet images with 4 spectral (B/G/R/NIR) band and 3m spatial resolution were used. However, the use of higher spectral/spatial resolution (for example Worldview-4 image with 8 spectral band and 30cm spatial resolution) or hyperspectral images (for example Hyperion EO1 image with 220 spectral band and 30m spatial resolution) should be considered and tested in estimating tomato cultivation areas for higher accuracy.

- Secondly, radar data can also be integrated into the classification to prevent reduction in the number of optical images to be used, especially in areas where cloud statistics are dense. In other words, radar data is also vital for filling the data gaps that cannot be obtained on some critical dates related to its dynamic nature (i.e., growth cycle). In addition, radar data with different system parameters, such as polarization, frequency, look angle, can provide distinctive information to thematic classification.

- Alternatively, object-based classification methods can be used and compared, where spatial information is added, and problems in pixel-based classification such as salt and pepper effect are reduced. On the other hand, contextual image classification

based on the relationships of adjacent pixels can also be considered as an alternative way.

- SAVI (Soil Adjusted Vegetation) can be integrated into the classification with other bands as an additional image feature, as it reduces the effects of soil that may predominate, especially in the early stages of crop growth.
- Even though RF is a frequently preferred method, different machine learning or deep-learning algorithms methods can be tested to better understand the reliability of ground-truth data and satellite images used.

Undoubtedly due to having extremely fertile soil structures, Turkey has a vital role across the world in agricultural production, especially in tomato production. This study showed that remote sensing technology can be used effectively in mapping tomato cultivated areas. Therefore, this thesis may lead to two important applications in the future. The first is to generalize the procedure to other tomato cultivated areas in different regions. The second is to evaluate the overall classification accuracy by applying the procedure used in this study to different crops, especially mixed ones. Thus, the reliability and applicability of the procedure can be significantly improved, and models for different products can be revised.

## REFERENCES


[1] **Brasesco, F.**, **Asgedom, D. and Casari, G.** (2019). Strategic analysis and intervention plan for fresh and industrial tomato in the Agro-Commodities Procurement Zone of the pilot Integrated Agro-Industrial Park in Central-Eastern Oromia, Ethiopia, **Technical Report**, Food and Agriculture Organizations of the United Nations, Addis, Ababa.

[2] **Vaglio Laurin, G.**, **Belli, C.**, **Bianconi, R.**, **Laranci, P. and Papale, D.** (2018). Early mapping of industrial tomato in Central and Southern Italy with Sentinel 2, aerial and RapidEye additional data, *Journal of Agricultural Science*, 1–12.

[3] **Ok, A.O.**, **Akar, O. and Gungor, O.** (2012). Evaluation of random forest method for agricultural crop classification, *European Journal of Remote Sensing*, *45*(1), 421–432.

[4] **Tatsumi, K.**, **Yamashiki, Y.**, **Torres, M.A.C. and Taipe, C.L.R.** (2015). Crop classification of upland fields using Random forest of time-series Landsat 7 ETM+ data, *Computers and Electronics in Agriculture*, *115*, 171–179, `http://dx.doi.org/10.1016/j.compag.2015.05.001`.

[5] **Hao, P.**, **Wang, L. and Niu, Z.** (2015). Comparison of hybrid classifiers for crop classification using normalized difference vegetation index time series: A case study for major crops in North Xinjiang, China, *PLoS ONE*, *10*(9).

[6] **Conrad, C.**, **Dech, S.**, **Dubovyk, O.**, **Fritsch, S.**, **Klein, D.**, **Löw, F.**, **Schorcht, G. and Zeidler, J.** (2014). Derivation of temporal windows for accurate crop discrimination in heterogeneous croplands of Uzbekistan using multitemporal RapidEye images, *Computers and Electronics in Agriculture*, *103*, 63–74, `http://dx.doi.org/10.1016/j.compag.2014.02.003`.

[7] **Maponya, M.G.**, **Van Niekerk, A. and Mashimbye, Z.E.** (2020). Pre-harvest classification of crop types using a Sentinel-2 time-series and machine learning, *Computers and Electronics in Agriculture*, *169*(December 2019), 105164, `https://doi.org/10.1016/j.compag.2019.105164`.

[8] **Inglada, J.**, **Arias, M.**, **Tardy, B.**, **Hagolle, O.**, **Valero, S.**, **Morin, D.**, **Dedieu, G.**, **Sepulcre, G.**, **Bontemps, S.**, **Defourny, P. and Koetz, B.** (2015). Assessment of an Operational System for Crop Type Map Production Using High Temporal and Spatial Resolution Satellite Optical Imagery,

*Remote Sensing*, *7*(9), 12356–12379, http://www.mdpi.com/2072-4292/7/9/12356.

[9] **Balasubramanian, K.I.** (2017). Identifying the Most Important Spectral and Textural Features to Map Specific Crops with Very High Resolution Images, *Ph.D. Dissertation*, University of Twente, https://webapps.itc.utwente.nl/librarywww/papers{_}2017/msc/gfm/balasubramanian.pdf.

[10] **Gallaun, H.**, **Steinegger, M.**, **Wack, R.**, **Schardt, M.**, **Kornberger, B. and Schmitt, U.** (2015). Remote sensing based two-stage sampling for accuracy assessment and area estimation of land cover changes, *Remote Sensing*, *7*(9), 11992–12008.

[11] **Campbell, J.B.** (2002). *Introduction to Remote Sensing*, Taylor & Francis, New York, 3rd edition.

[12] **Url-1**, <*https://earthobservatory.nasa.gov*, date retrieved: 28.03.2020.

[13] **National Research Council** (1998). *People and Pixels: Linking Remote Sensing and Social Science*, The National Academies Press, Washington, DC.

[14] **Url-2**, <*https://earthdata.nasa.gov*>, date retrieved: 28.03.2020.

[15] **Url-3**, <*https://www.usgs.gov*>, date retrieved: 28.03.2020.

[16] **Jensen, J.R.** (2016). *Introductory Digital Image Processing: A Remote Sensing Perspective*, Pearson Education, Glenview.

[17] **Url-4**, <*https://www.nrcan.gc.ca*>, date retrieved: 28.03.2020.

[18] **Smith, R.B.** (2012). *Introduction to Remote Sensing of Environment (RSE)*, MicroImages Inc.

[19] **Url-5**, <*https://sites.google.com/site/chempendix/em-spectrum*>, date retrieved: 28.03.2020.

[20] **Sunar, F.**, **Özkan, C. and Osmanoğlu, B.** (2016). *Uzaktan Algılama*, Anadolu University, Eskişehir, fourth edition.

[21] **Bondada, B.R.** (2011). Anomalies in structure, growth characteristics, and nutritional composition as induced by 2,4-dichlorophenoxy acetic acid drift phytotoxicity in grapevine leaves and clusters, *Journal of the American Society for Horticultural Science*, *136*(3), 165–176.

[22] **Url-6**, <*https://www.seos-project.eu*>, date retrieved: 28.03.2020.

[23] **Chuvieco, E. and Huete, A.** (2010). *Fundamentals of Satellite Remote Sensing*, CRC Press Taylor & Francis Group, New York.

[24] **Gates, D.M.**, **Keegan, H.J.**, **Schleter, J.C. and Weidner, V.R.** (1965). Spectral properties of plants, *Applied Optics*, *4*, 11–20.

[25] **Url-7**, <*http://gsp.humboldt.edu*>, date retrieved: 28.03.2020.

[26] **Shamshiri, R.R.**, **Jones, J.W.**, **Thorp, K.R.**, **Ahmad, D.**, **Man, H.C. and Taheri, S.** (2018). Review of optimum temperature, humidity, and vapour pressure deficit for microclimate evaluation and control in greenhouse cultivation of tomato: A review, *International Agrophysics*, *32*(2), 287–302.

[27] **Url-8**, <*http://tomatosphere.letstalkscience.ca*>, date retrieved: 25.04.2020.

[28] **Url-9**, <*http://www.geo-informatie.nl*>, date retrieved: 28.03.2020.

[29] **Li, B.**, **Lecourt, J. and Bishop, G.** (2018). Advances in non-destructive early assessment of fruit ripeness towards defining optimal time of harvest and yield prediction—a review, *Plants*, *7*(3), 1–20.

[30] **Lu, J.**, **Ehsani, R.**, **Shi, Y.**, **De Castro, A.I. and Wang, S.** (2018). Detection of multi-tomato leaf diseases (late blight, target and bacterial spots) in different stages by using a spectral-based sensor, *Scientific REpoRtS* |, *8*, 2793, `www.nature.com/scientificreports/`.

[31] **Xie, C.**, **Shao, Y.**, **Li, X. and He, Y.** (2015). Detection of early blight and late blight diseases on tomato leaves using hyperspectral imaging, *Scientific Reports*, *5*(16564), `http://dx.doi.org/10.1038/srep16564`.

[32] **Bodirwa, K.B.** (2009). Nitrogen Variability Assessmnet in Tomatoes Using the Remote Sensing Technique for Precision Farming, Dissertation, University of Limpopo.

[33] **Url-10**, <*https://www.cleantechconcepts.com*>, date retrieved: 25.04.2020.

[34] **Calvão, T. and Fernanda Pessoa, M.** (2015). Remote sensing in food production - a review, *Emirates Journal of Food and Agricuture*, *27*(2), 138–151, `http://www.ejfa.info/138`.

[35] **Atzberger, C.** (2013). Advances in Remote Sensing of Agriculture: Context Description, Existing Operational Monitoring Systems and Major Information Needs, *Remote Sensing*, *5*(2), 949–981, `http://www.mdpi.com/2072-4292/5/2/949`.

[36] **Url-11**, <*https://grindgis.com/remote-sensing*>, date retrieved: 28.03.2020.

[37] **Steven, M.D. and Clark, J.A.** (1990). *Applications of remote sensing in agriculture*, University Press, Cambridge, Great Britain.

[38] **FAO** (2005). A system of integrated agricultural censuses and surveys: world programme for census of agriculture 2010, **Technical Report**, Food and Agriculture Organization of the United Nations.

[39] **Url-12**, <*http://www.fao.org/faostat/en/#country/223*>, date retrieved: 28.03.2020.

[40] **TAGEM and T.C. Gıda Tarım ve Hayvancılık Bakanlığı** (2018). Tarım Ürünleri Piyasaları, **Technical Report**.

[41] **Planet Labs Inc.** (2019). Planet Imagery Product Spesifications, **Technical Report**, Planet Labs Inc., https://assets.planet.com/docs/combined-imagery-product-spec-april-2019.pdf.

[42] **Url-13**, <*https://gisgeography.com/planet-labs-imagery/*>, date retrieved: 19.05.2020.

[43] **Url-14**, <*https://www.planet.com/pulse/firehose/*>, date retrieved: 28.03.2020.

[44] **Url-15**, <*https://www.spatialsource.com.au*>, date retrieved: 19.05.2020.

[45] **Collison, A. and Wilson, N.** (2018). Planet Surface Reflectance Product, **Technical ReportFebruary**.

[46] **Url-16**, <*http://6s.ltdri.org/index.html*>, date retrieved: 19.05.2020.

[47] **Planet Team**, (2018), Planet Application Program Interface: In Space for Life on Earth, https://api.planet.com.

[48] **GFOI** (2013). Integrating remote-sensing and ground-based observations for estimation of emissions and removals of greenhouse gases in forests, **Technical Report**, Methods and Guidance from the Global Forest Observations Initiative, Geneva, Switzerland, https://www.reddcompass.org/mgd-content-v1/dita-webhelp/en/d0e11.html{#}d0e11.

[49] **Japan Association of Remote Sensing** (1999). *Remote Sensing Notes*.

[50] **Schwering, P.B.W.**, **Kemp, R.A.W. and Schutte, K.** (2013). Image enhancement technology research for army applications, *Infrared Imaging Systems: Design, Analysis, Modeling, and Testing XXIV*, *8706*.

[51] **Baghdadi, N.**, **Mallet, C. and Zribi, M.** (2018). *QGIS and Applications in Agriculture and Forest*, ISTE Ltd and John Wiley & Sons, Inc., London and Hoboken.

[52] **Jackson, R.D. and Huete, A.R.** (1991). Interpreting vegetation indices, *Preventive Veterinary Medicine*, *11*(3-4), 185–200.

[53] **Url-17**, <*http://www.dronedynamics.com*>, date retrieved: 05.04.2020.

[54] **Xue, J. and Su, B.** (2017). Significant remote sensing vegetation indices: A review of developments and applications, *Journal of Sensors*, *2017*(June).

[55] **Schowengerdt, R.A.**, (2007). Spectral Transforms, Remote Sensing: Models and Methods for Image Processing, chapter 5, Elsevier Inc., 3 edition, pp.183–228.

[56] **Bannari, A.**, **Morin, D.**, **Bonn, F. and Huete, A.R.** (1995). A review of vegetation indices, *Remote Sensing Reviews*, *13*(1-2), 95–120.

[57] **Mróz, M. and Sobieraj, A.** (2004). Comparison of several vegetation indices calculated on the basis of a seasonal SPOT XS time series, and their suitability for land cover and agricultural crop identification, *Technical Sciences*, *7*, 39–66.

[58] **Url-18**, <*https://wiki.landscapetoolbox.org*>, date retrieved: 23.05.2020.

[59] **Pearson, R.L. and Miller, L.D.** (1972). Remote mapping of standing crop biomass for estimation of the productivity of the shortgrass prairie, Pawnee National Grasslands, Colorado, *Proceedings of the 8th International Symposium on Remote Sensing of the Environment*, pp.1355–1379.

[60] **Rouse, J.W.**, **Haas, R.W.**, **Schell, J.A.**, **Deering, D.W. and Harlan, J.C.** (1974). Monitoring the vernal advancement and retrogradation (Greenwave effect) of natural vegetation, **Technical Report**, NASA/GSFCT, Maryland.

[61] **Huete, A.R.** (1988). A soil-adjusted vegetation index (SAVI), *Remote Sensing of Environment*, *25*, 295–309.

[62] **Huete, A.**, **Didan, K.**, **Miura, T.**, **Rodriguez, E.**, **Gao, X. and Ferreira, L.** (2002). Overview of the radiometric and biophysical performance of the MODIS vegetation indices, *Remote Sensing of Environment*, *83*, 195–213.

[63] **Richardson, A.J. and Wiegand, C.L.** (1977). Distinguishing vegetation from soil background informa- tion, *Photogrammetric Engineering and Remote Sensing*, *43*(12), 1541–1552.

[64] **Foerster, S.**, **Kaden, K.**, **Foerster, M. and Itzerott, S.** (2012). Crop type mapping using spectral – temporal profiles and phenological information, *Computers and Electronics in Agriculture*, *89*, 30–40, `http://dx.doi.org/10.1016/j.compag.2012.07.015`.

[65] **Li, C.**, **Li, H.**, **Li, J.**, **Lei, Y.**, **Li, C.**, **Manevski, K. and Shen, Y.** (2019). Using NDVI percentiles to monitor real-time crop growth, *Computers and Electronics in Agriculture*, *162*(April), 357–363, `https://doi.org/10.1016/j.compag.2019.04.026`.

[66] **Kanke, Y.**, **Tubaña, B.**, **Dalen, M. and Harrell, D.** (2016). Evaluation of red and red-edge reflectance-based vegetation indices for rice biomass and grain yield prediction models in paddy fields, *Precision Agriculture*, *17*, 507–530.

[67] **Sun, Y.**, **Qin, Q.**, **Ren, H.**, **Zhang, T. and Chen, S.** (2020). Red-Edge Band Vegetation Indices for Leaf Area Index Estimation from Sentinel-2/MSI Imagery, *IEEE Transactions on Geoscience and Remote Sensing*, *58*(2), 826–840.

[68] **Xie, Q.**, **Dash, J.**, **Huang, W.**, **Peng, D.**, **Qin, Q.**, **Mortimer, H.**, **Casa, R.**, **Pignatti, S.**, **Laneve, G.**, **Pascucci, S.**, **Dong, Y. and Ye, H.**

(2018). Vegetation Indices Combining the Red and Red-Edge Spectral Information for Leaf Area Index Retrieval, *IEEE Journal of Selected Topics in Applied Earth Observations and Remote Sensing*, *11*(5), 1482–1493.

[69] **Peña-Barragán, J.M.**, **Ngugi, M.K.**, **Plant, R.E. and Six, J.** (2011). Object-based crop identification using multiple vegetation indices, textural features and crop phenology, *Remote Sensing of Environment*, *115*(6), 1301–1316, http://dx.doi.org/10.1016/j.rse.2011.01.009.

[70] **Sun, C.**, **Bian, Y.**, **Zhou, T. and Pan, J.** (2019). Using of Multi-Source and Multi-Temporal Remote Sensing Data Improves Crop-Type Mapping in the Subtropical Agriculture Region, *Sensors*, *19*(10), 2401–2424.

[71] **Haralick, R.M.**, **K, S. and Dinstein, I.** (1973). Textural Features for Image Classification, *IEEE Transactions on Systems, Man and Cybernetics*, *SMC-3*(6), 610–621.

[72] **Fagan, C.C.**, **Du, C.J.**, **O'Donnell, C.P.**, **Castillo, M.**, **Everard, C.D.**, **O'Callaghan, D.J. and Payne, F.A.** (2008). Application of image texture analysis for online determination of curd moisture and whey solids in a laboratory-scale stirred cheese vat, *Journal of Food Science*, *73*(6), 250–258.

[73] **Hall-Beyer, M.**, (2017). GLCM Texture: A Tutorial v. 3.0.

[74] **Url**, <*https://www.mathworks.com/help/images/specify-offset-used-in-glcm-calculation.html*>, date retrieved: 28.03.2020.

[75] **Url-19**, <*https://github.com/cerr/CERR/wiki/GLCM_global_features*>, date retrieved: 28.03.2020.

[76] **Url-20**, <*https://pyradiomics.readthedocs.io/en*>, date retrieved: 28.03.2020.

[77] **Zayed, N. and Elnemr, H.A.** (2015). Statistical Analysis of Haralick Texture Features to Discriminate Lung Abnormalities, *International Journal of Biomedical Imaging*, *2015*.

[78] **Li, M.**, **Zang, S.**, **Zhang, B.**, **Li, S. and Wu, C.** (2014). A review of remote sensing image classification techniques: The role of spatio-contextual information, *European Journal of Remote Sensing*, *47*(1), 389–411.

[79] **Belgiu, M. and Dra˘gut, L.** (2016). Random forest in remote sensing: A review of applications and future directions, *ISPRS Journal of Photogrammetry and Remote Sensing*, *114*, 24–31, http://dx.doi.org/10.1016/j.isprsjprs.2016.01.011.

[80] **Horning, N.** (2010). Random Forests: An algorithm for image classification and generation of continuous fields data sets, *International Conference on Geoinformatics for Spatial Infrastructure Development in Earth and Allied Sciences 2010*, pp.1–6, 1609-3631.

[81] **Sunar, F.**, **Özkan, C.**, **Ok, A.Ö.**, **Osmanoğlu, B.**, **Uça Avcı, D. and Berberoğlu, S.** (2017). *Dijital Görüntü İşleme*, Anadolu University, Eskişehir, first edition.

[82] **Jia, X.** (2017). Supervised Classification, *International Encyclopedia of Geography: People, the Earth, Environment and Technology*, 1–3.

[83] **Url-21**, <*https://medium.com/@Synced*>, date retrieved: 28.03.2020.

[84] **Louppe, G.** (2014). Understanding Random Forests From Theory to Practice, Phd dissertation, University of Liège, `arXiv:1407.7502v2`.

[85] **Pal, M.** (2005). Random forest classifier for remote sensing classification, *International Journal of Remote Sensing*, *26*(1), 217–222, `arXiv:1011.1669v3`.

[86] **Sá, J.A.S.**, **Almeida, A.C.**, **Rocha, B.R.P.**, **Mota, M.A.S.**, **Souza, J.R.S. and Dentel, L.M.** (2011). Lightning Forecast Using Data Mining Techniques On Hourly Evolution Of The Convective Available Potential Energy, *10th Brazilian Congress on Computational Intelligence (CBIC'2011)*, November, Fortaleza, Ceará Brazil, pp.1–5.

[87] **Horning, N.** Introduction to decision trees and random forests.

[88] **Minitab** (2018). Introduction to Random Forests ®, **Technical Report**.

[89] **Breiman, L.** (2001). Random Forests, *Machine Learning*, *45*, 5–32, `https://link.springer.com/content/pdf/10.1023{%}2FA{%}3A1010933404324.pdf`.

[90] **Url-22**, <*https://towardsdatascience.com*>, date retrieved: 28.03.2020.

[91] **Liaw, A. and Wiener, M.** (2002). Classification and Regression by randomForest, *R News*, *2*(3), 18–22.

[92] **Url-23**, <*https://www.displayr.com*>, date retrieved: 23.05.2020.

[93] **Url-24**, <*https://www.causeweb.org/usproc/eusrc/2018/program/1*>, date retrieved: 09.05.2020.

[94] **Dinov, I.D.** (2018). *Prediction and Internal Statistical Cross Validation. In: Data Science and Predictive Analytics*, Springer, Cham.

[95] **Url-25**, <*https://www.statisticshowto.com/cross-validation-statistics/*>, date retrieved: 13.06.2020.

[96] **Valavi, R.**, **Elith, J.**, **Lahoz-Monfort, J.J. and Guillera-Arroita, G.** (2019). blockCV: An r package for generating spatially or environmentally separated folds for k-fold cross-validation of species distribution models, *Methods in Ecology and Evolution*, *10*(2), 225–232.

[97] **Url-26**, <*https://towardsdatascience.com*>, date retrieved: 07.06.2020.

[98] **Url-27**, <*https://scikit-learn.org/stable/modules/cross_validation.html*>, date retrieved: 09.06.2020.

[99] **Congalton, R.G.** (1991). A review of assessing the accuracy of classifications of remotely sensed data, *Remote Sensing of Environment*, *37*(1), 35–46.

[100] **Lunetta, R.S. and Lyon, J.G.** (2004). *Remote sensing and GIS accuracy assessment*, CRC Press.

[101] **Url-28**, <*https://machinelearningmastery.com*>, date retrieved: 17.05.2020.

[102] **Congalton, R.G. and Green, K.** (2019). *Assessing the accuracy of remotely sensed data: principles and practices*, CRC Press Taylor & Francis Group, Florida, third edition, `https://books.google.com.tr/books?id=yTmDDwAAQBAJ{&}printsec=frontcover{&}hl=tr{#}v=onepage{&}q{&}f=false`.

[103] **Hsiao, L.H. and Cheng, K.S.** (2016). Assessing uncertainty in LULC classification accuracy by using bootstrap resampling, *Remote Sensing*, *8*(9), 705.

[104] **Raschka, S.** (2018). Model Evaluation, Model Selection, and Algorithm Selection in Machine Learning, *ArXiv*, *abs/1811.12808*, `http://arxiv.org/abs/1811.12808`, `1811.12808`.

[105] **Weber, K.T. and Langille, J.** (2007). Improving classification accuracy assessments with statistical bootstrap resampling techniques, *GIScience and Remote Sensing*, *44*(3), 237–250.

[106] **Url-29**, <*https://machinelearningmastery.com*>, date retrieved: 10.05.2020.

[107] **Url-30**, <*https://www.statisticshowto.com/bootstrap-sample/*>, date retrieved: 10.05.2020.

[108] **Goodhue, D.L.**, **Lewis, W. and Thompson, R.** (2012). Does PLS have advantages for small sample size or non-normal data?, *MIS Quarterly*, *36*(3), 981–1001.

[109] **Url-31**, <*https://medium.com/better-programming*>, date retrieved: 16.05.2020.

[110] **Efron, B. and Tibshirani, R.J.** (1994). *An Introduction to the Bootstrap. Chapman & Hall/CRC Monographs on Statistics & Applied Probability*, CRC Press LLC, Florida, `https://books.google.com.tr/books?id=gLlpIUxRntoC{&}printsec=frontcover{&}hl=tr{&}source=gbs{_}ge{_}summary{_}r{&}cad=0{#}v=onepage{&}q{&}f=false`.

[111] **DiCiccio, T.J. and Efron, B.** (1996). Bootstrap Confidence Intervals, *Statistical Science*, *11*(3), 189–228.

[112] **Url-32**, <*https://bursa.ktb.gov.tr/TR-94929/karacabey.html*>, date retrieved: 24.05.2020.

[113] **Köksal, E.S.**, **Çetin, S.**, **Demir, A.O.**, **Tunca, E.**, **Candoğan, B.N. and Akkaya Aslan, .T.** (2018). Bursa Karacabey Ovasında Son 25 Yılda Değişen Bitkisel Üretim Deseni ve Sulama Uygulamalarının Uzaktan Algılama ve ET Haritalama Tekniği ile Değerlendirilmesi, *Bursa Uludağ Üniversitesi Ziraat Fakültesi Dergisi*, *32*(2), 31–43, http://dergipark.gov.tr/bursauludagziraat;http://www.uludag.edu.tr/ziraatdergi{%}0AAraşt\T1\irma.

[114] **Url-33**, <*https://www.tarim.bayer.com.tr*>, date retrieved: 26.04.2020.

[115] **Planet Labs Inc.** (2018). Planet Imagery Product Spesification, **Technical ReportAugust**, https://www.planet.com/products/planet-imagery/.

[116] **Planet Labs Inc.** (2018). Planet Explorer User Guide, https://www.planet.com/products/explorer/.

[117] **Belgiu, M. and Csillik, O.** (2018). Sentinel-2 cropland mapping using pixel-based and object-based time- weighted dynamic time warping analysis, *Remote Sensing of Environment*, *204*(September 2017), 509–523, https://doi.org/10.1016/j.rse.2017.10.005.

[118] **El-Gammal, M.I.**, **Ali, R.R. and R. M. Abou Samra** (2014). NDVI Threshold Classification for Detecting Vegetation Cover in Damietta Governorate, Egypt, *Journal of American Science*, *10*(8), 108–113.

## APPENDICES

**APPENDIX A :** Time-series of all other calculated image features
**APPENDIX B :** All other Bootstrapping histograms of the second scenario
**APPENDIX C :** Thematic maps of each fold for 4th and 15th cases in the third scenario

## APPENDIX A

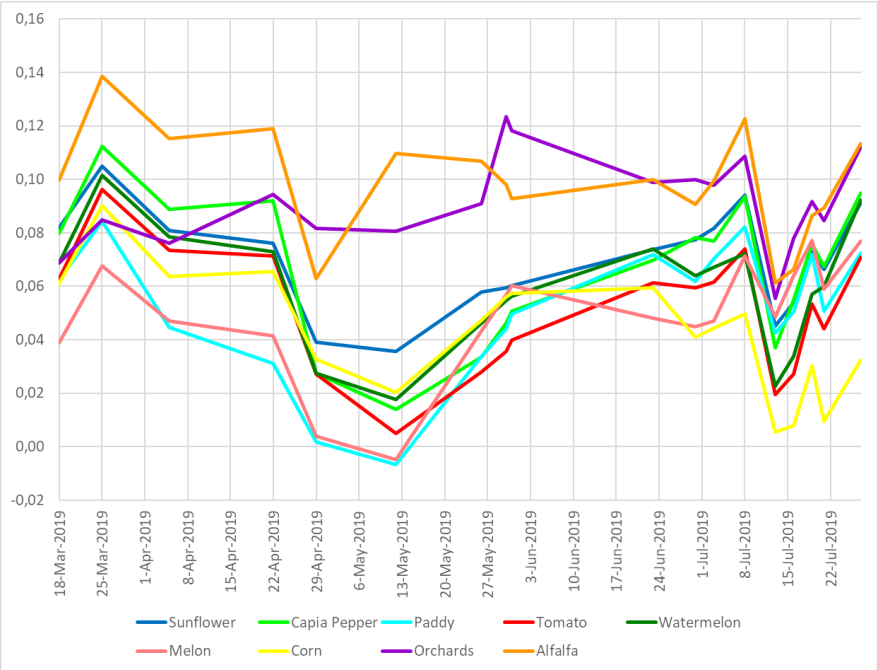


**Figure A.1 :** Time-series of the "Correlation" feature.

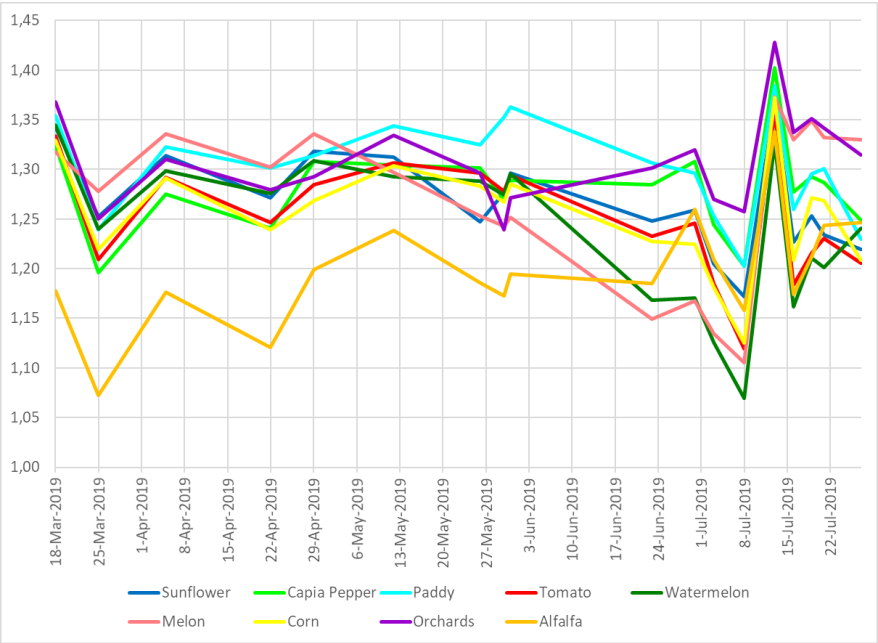


**Figure A.2 :** Time-series of the "Difference Entropy" feature.

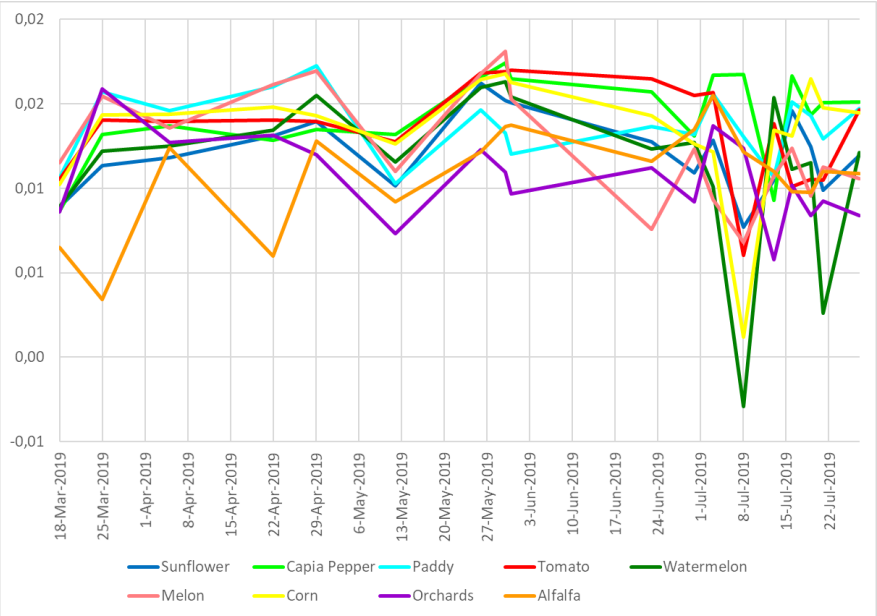


**Figure A.3 :** Time-series of the "Difference Variance" feature.

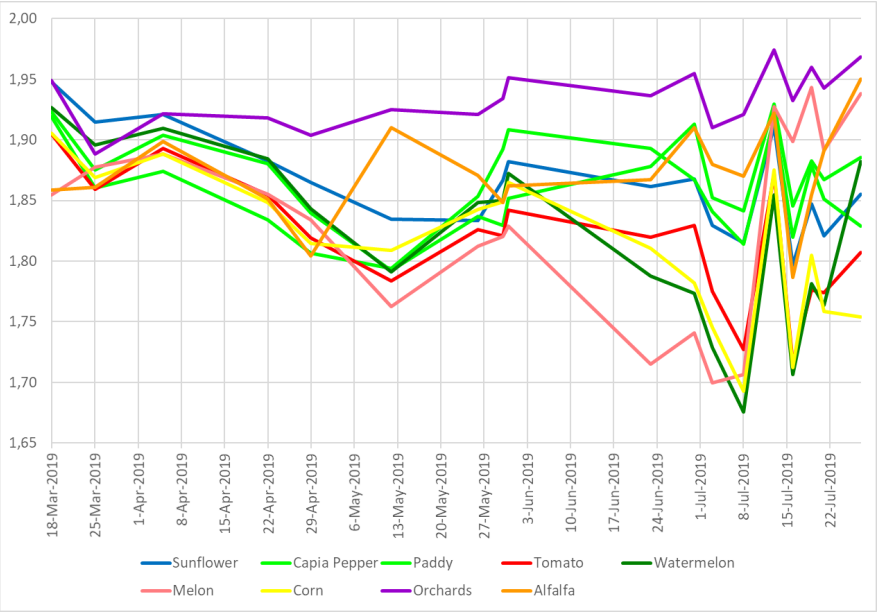


**Figure A.4 :** Time-series of the "Sum Entropy" feature.

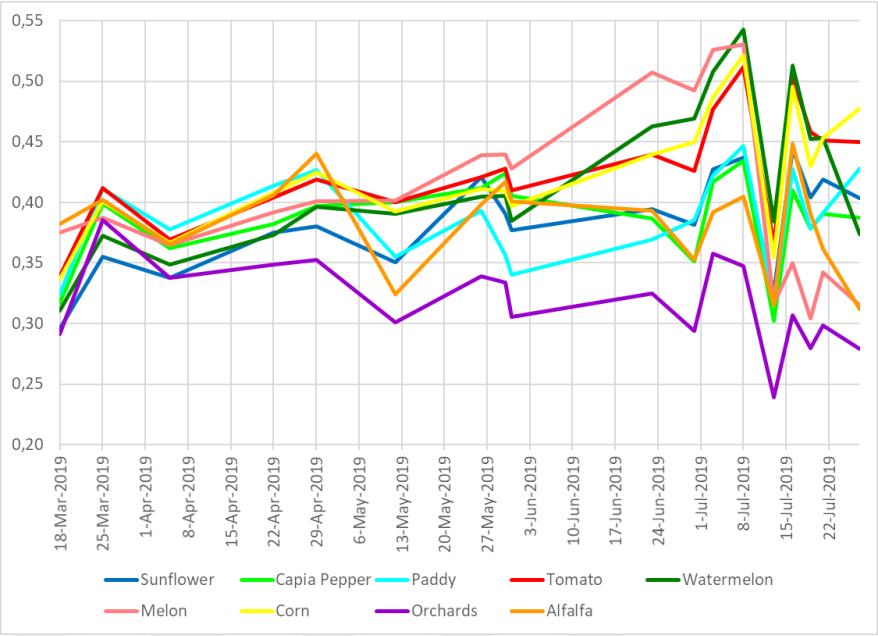


**Figure A.5 :** Time-series of the "Inverse Difference Moment" feature.

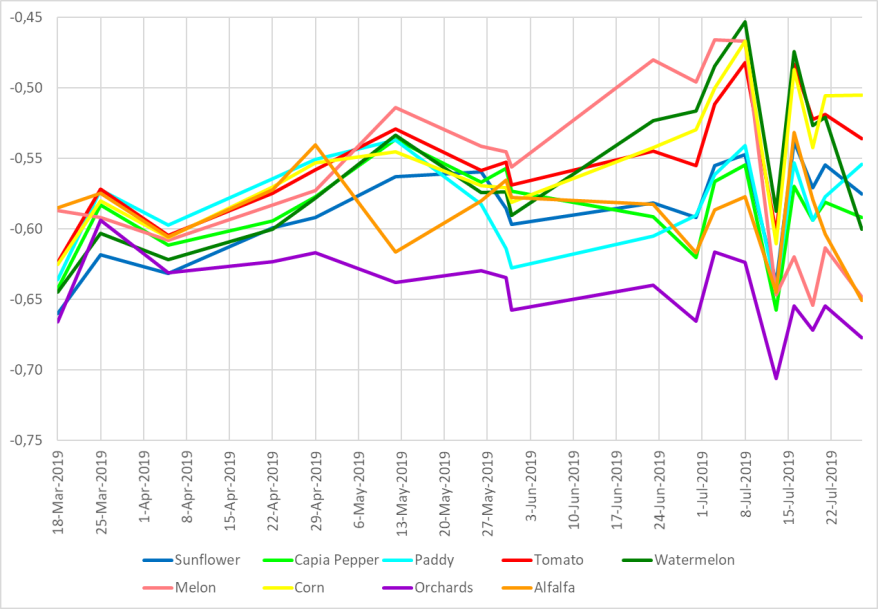


**Figure A.6 :** Time-series of the "Information Measures of Correlation 1" feature.

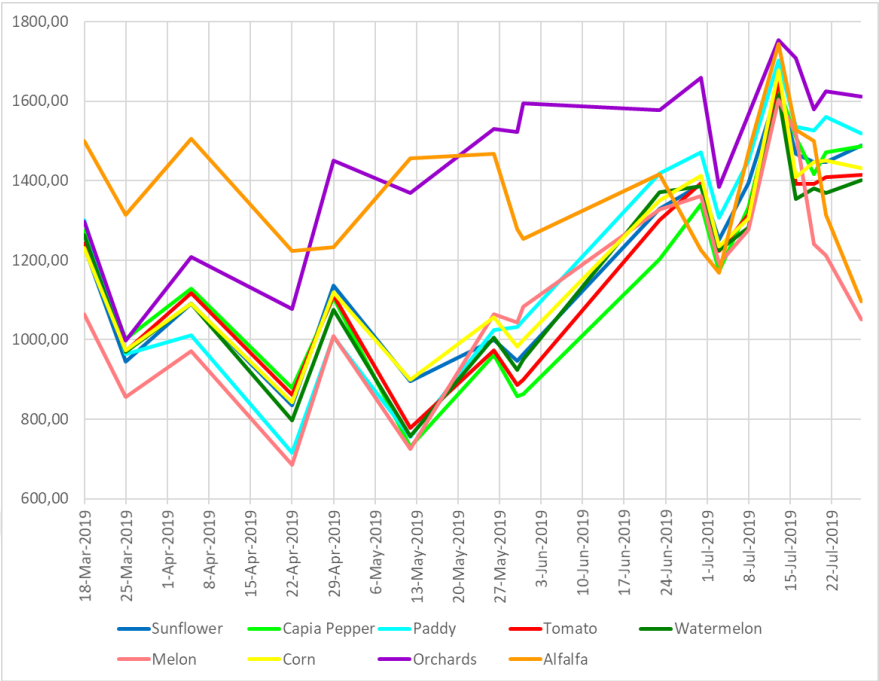


**Figure A.7 :** Time-series of the "Sum Average" feature.

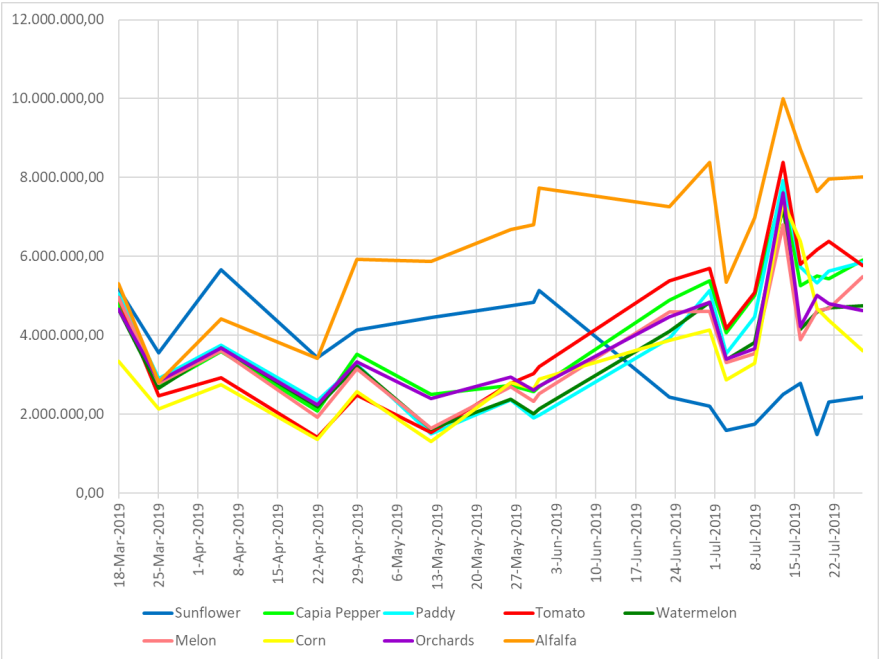


**Figure A.8 :** Time-series of the "Sum Variance" feature.

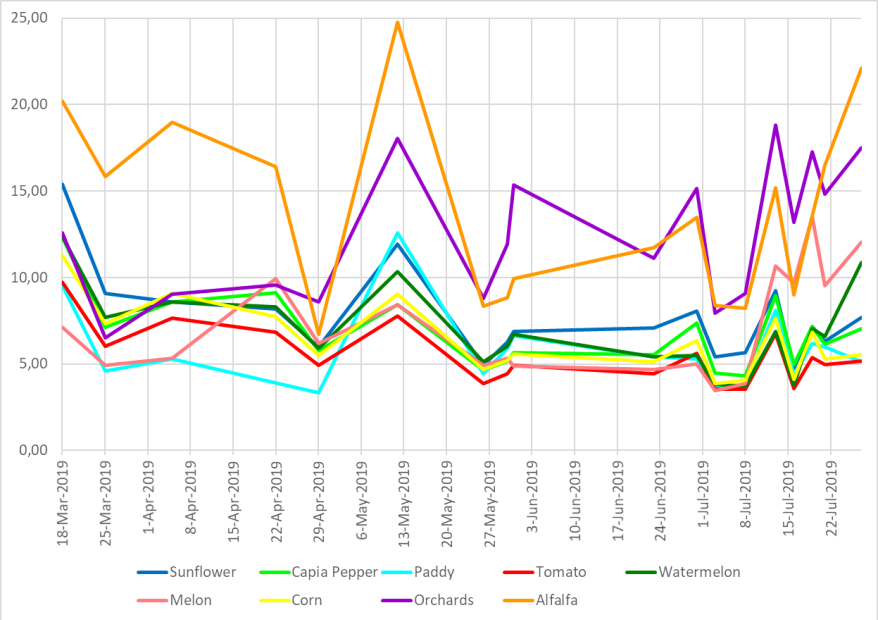


**Figure A.9 :** Time-series of the “Variance” feature.

## APPENDIX B

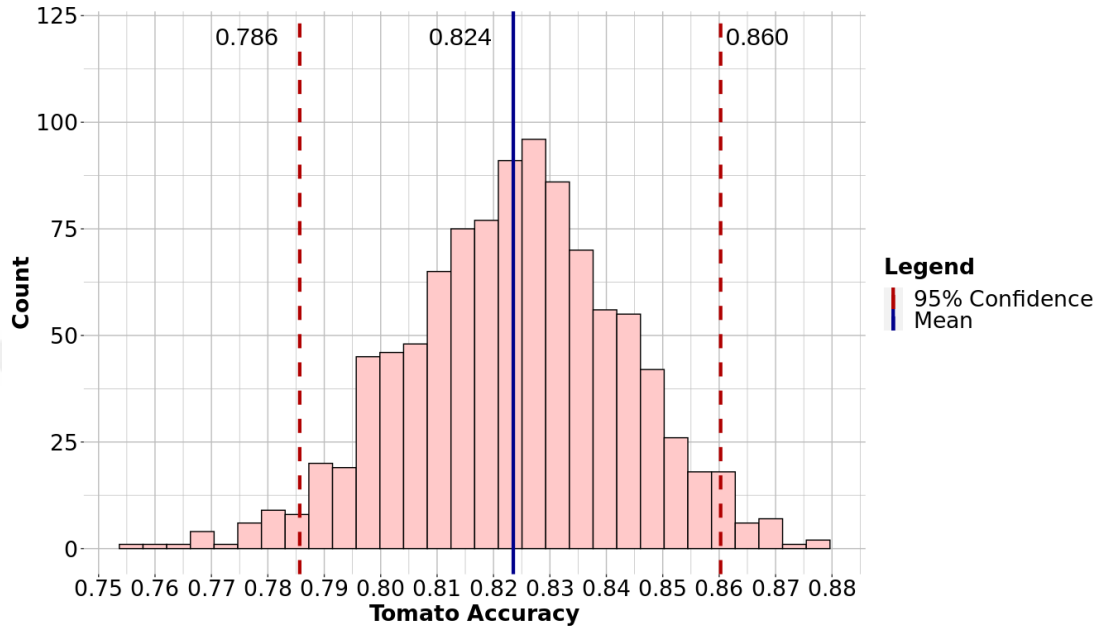


**Figure B.1 :** Bootstrapping histogram with average accuracy and confidence intervals for the 1st classification case.

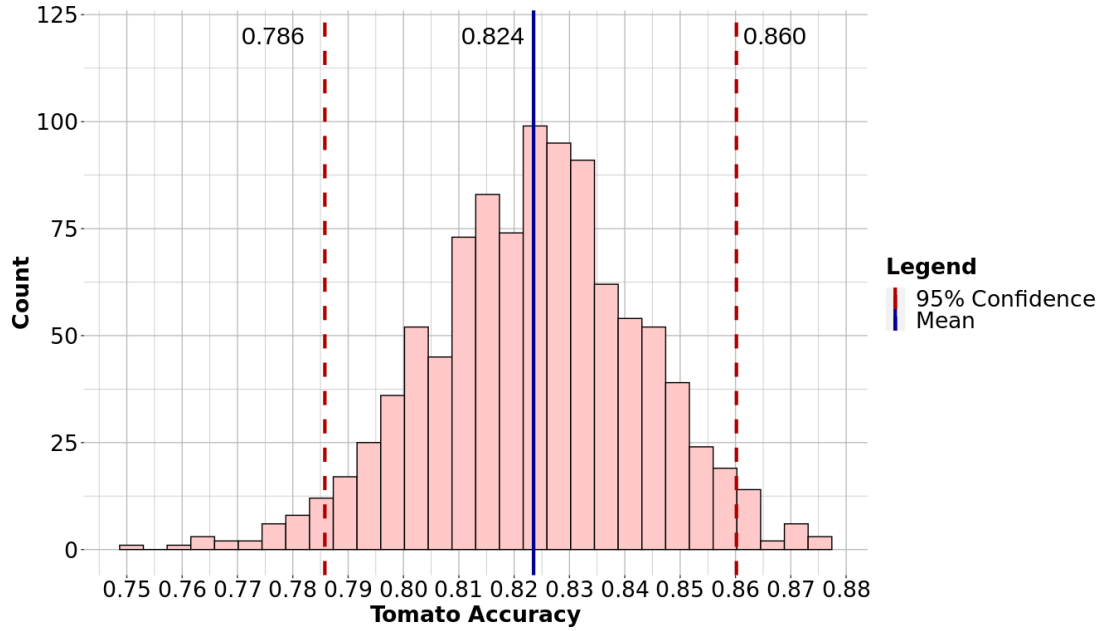


**Figure B.2 :** Bootstrapping histogram with average accuracy and confidence intervals for the 2nd classification case.

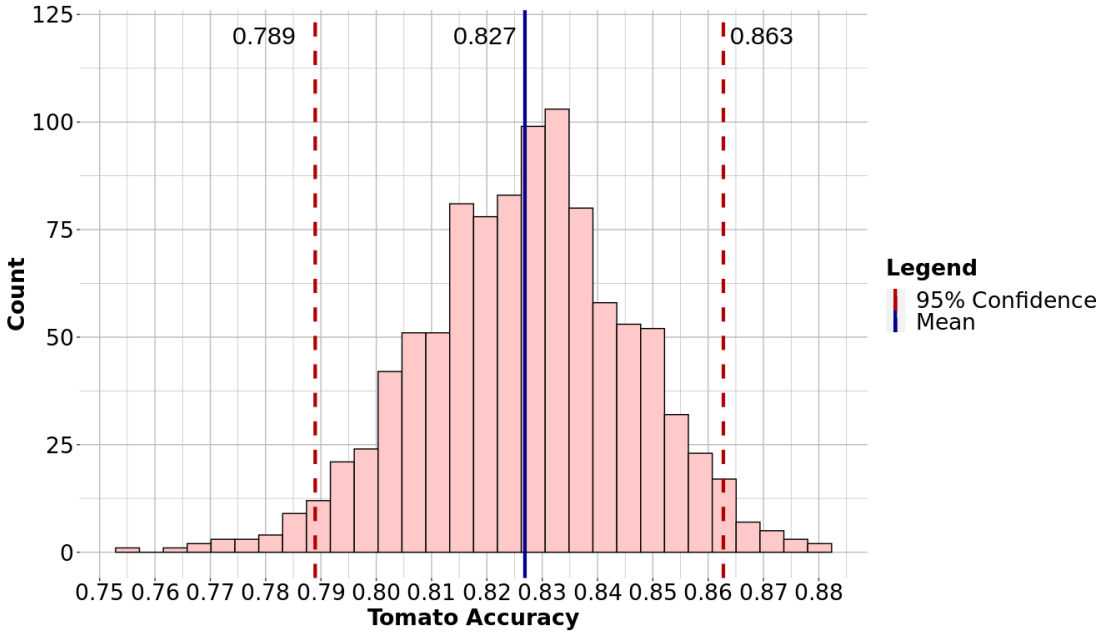


**Figure B.3 :** Bootstrapping histogram with average accuracy and confidence intervals for the 3rd classification case.

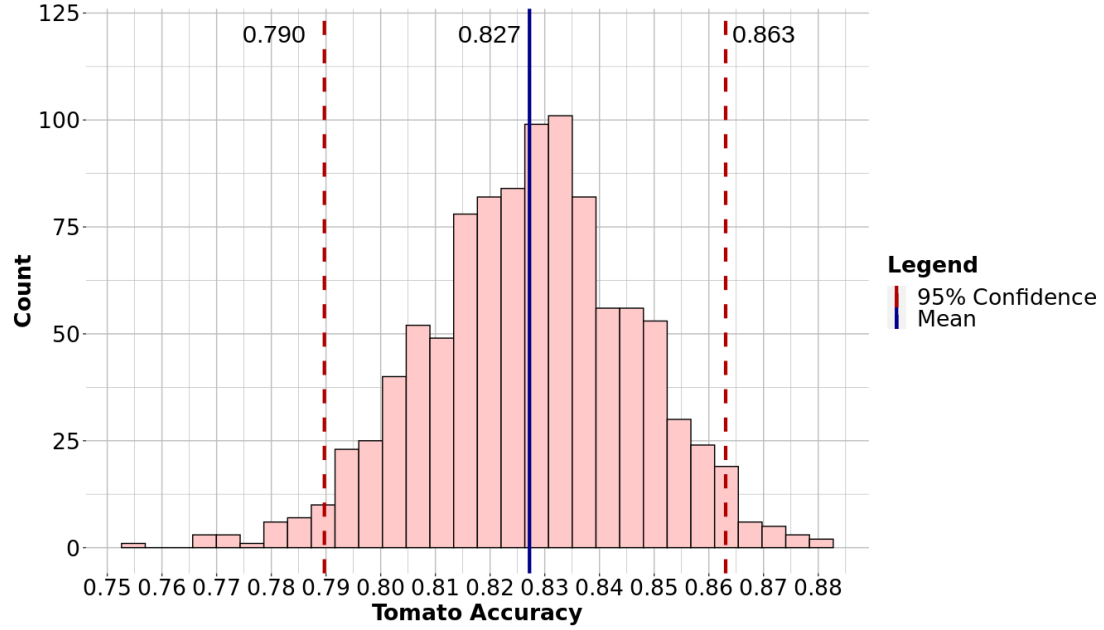


**Figure B.4 :** Bootstrapping histogram with average accuracy and confidence intervals for the 4th classification case.

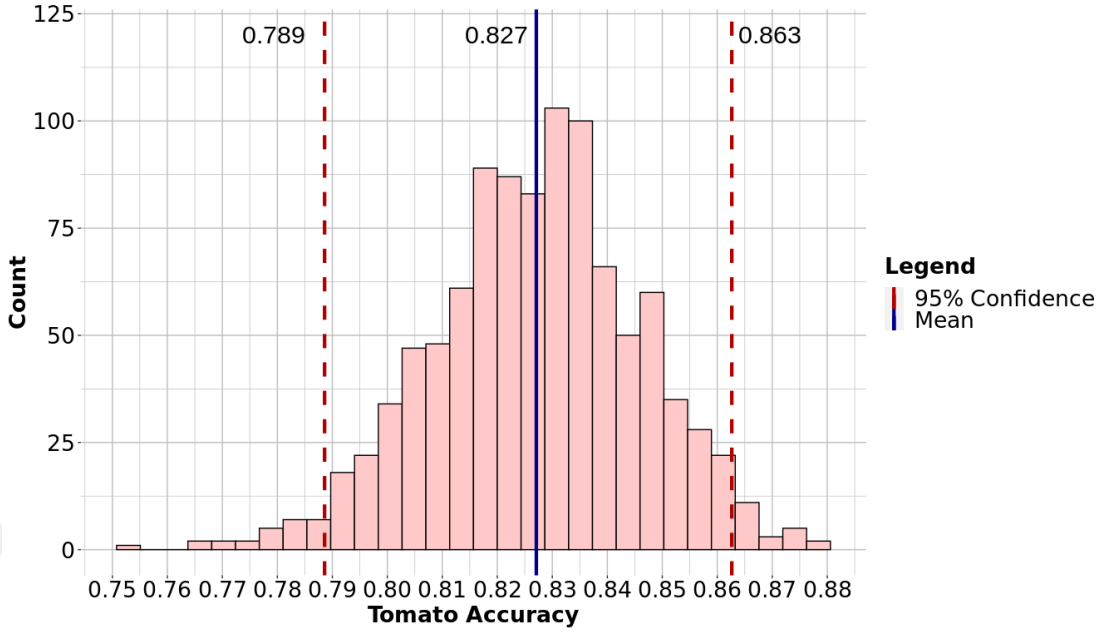


**Figure B.5 :** Bootstrapping histogram with average accuracy and confidence intervals for the 5th classification case.

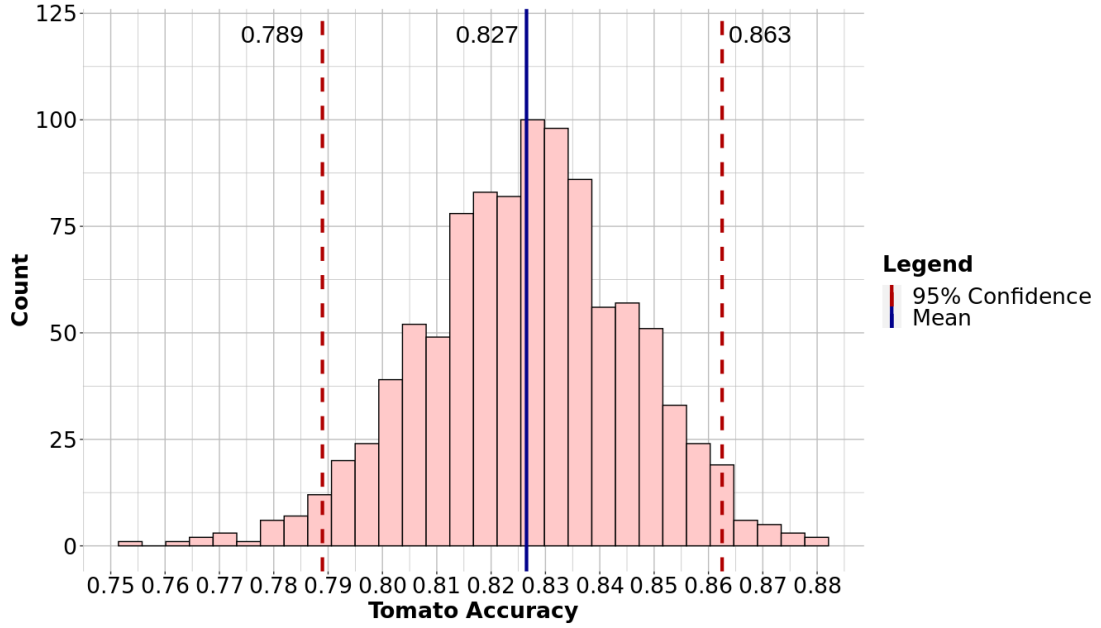


**Figure B.6 :** Bootstrapping histogram with average accuracy and confidence intervals for the 7th classification case.

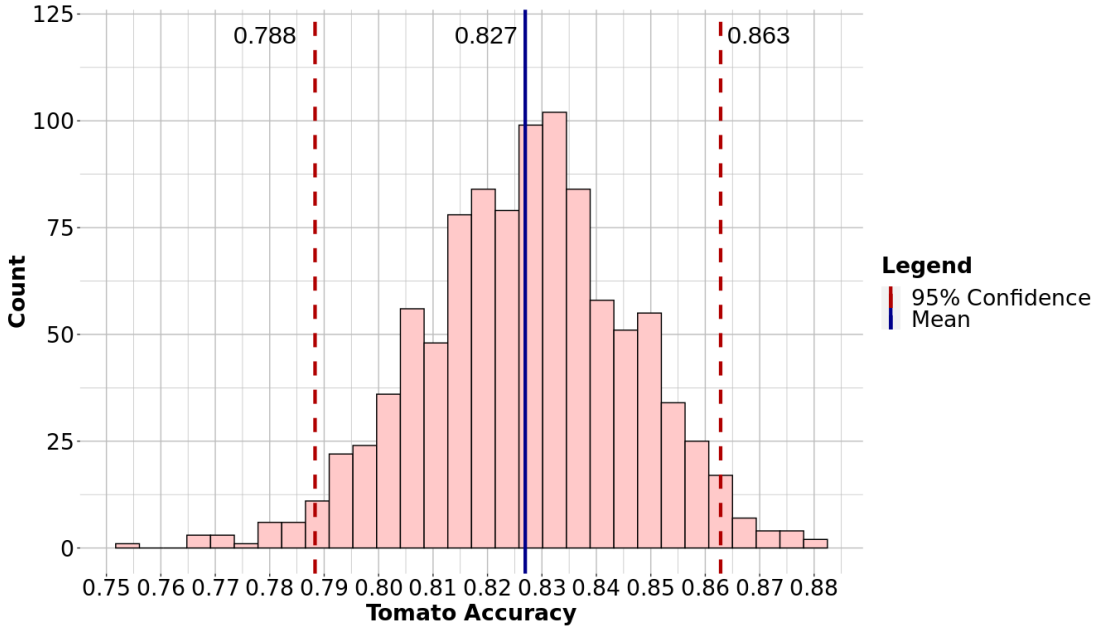


**Figure B.7 :** Bootstrapping histogram with average accuracy and confidence intervals for the 8th classification case.

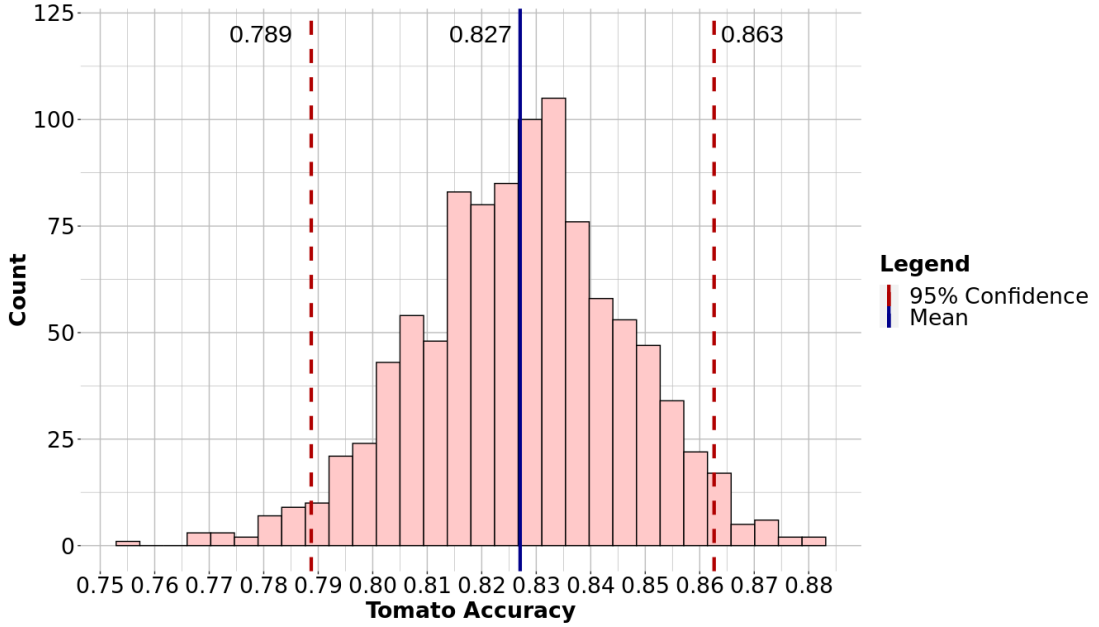


**Figure B.8 :** Bootstrapping histogram with average accuracy and confidence intervals for the 9th classification case.

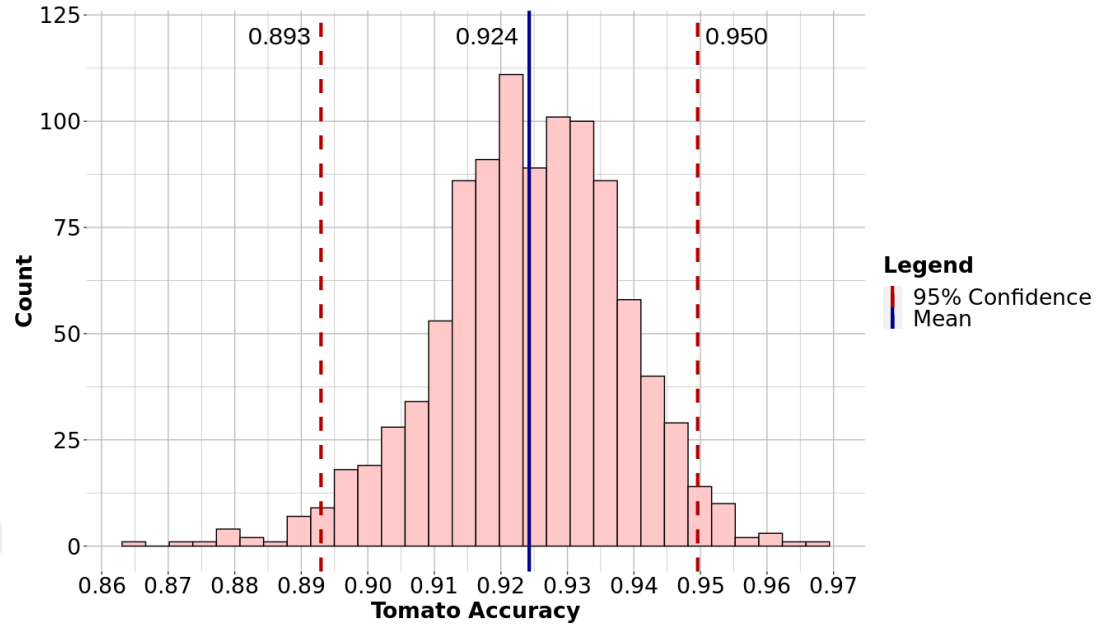


**Figure B.9 :** Bootstrapping histogram with average accuracy and confidence intervals for the 10th classification case.

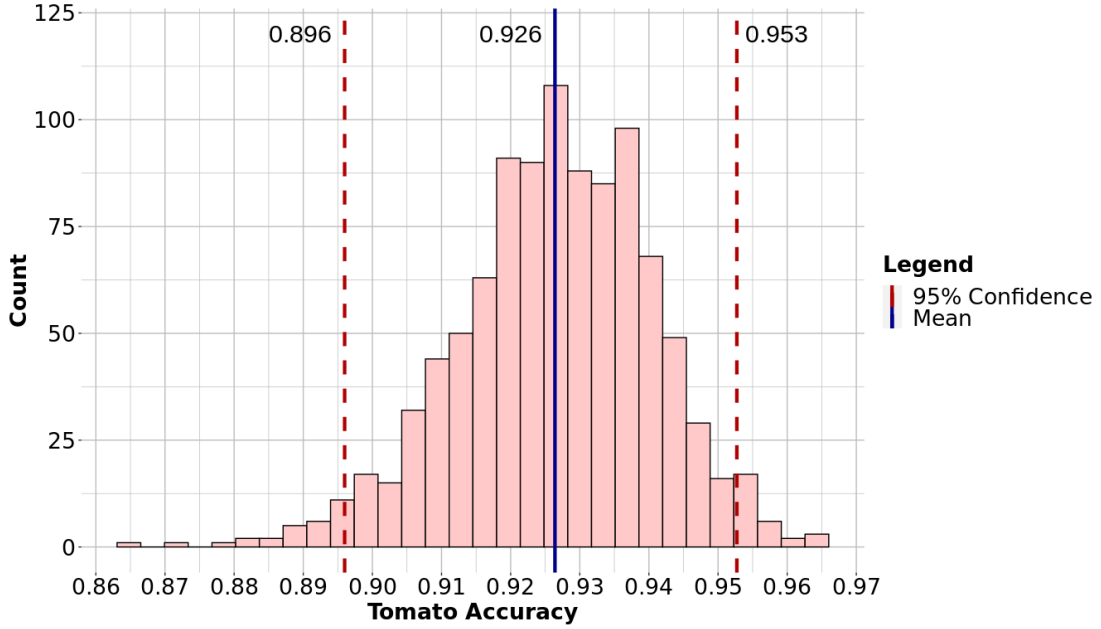


**Figure B.10 :** Bootstrapping histogram with average accuracy and confidence intervals for the 11th classification case.

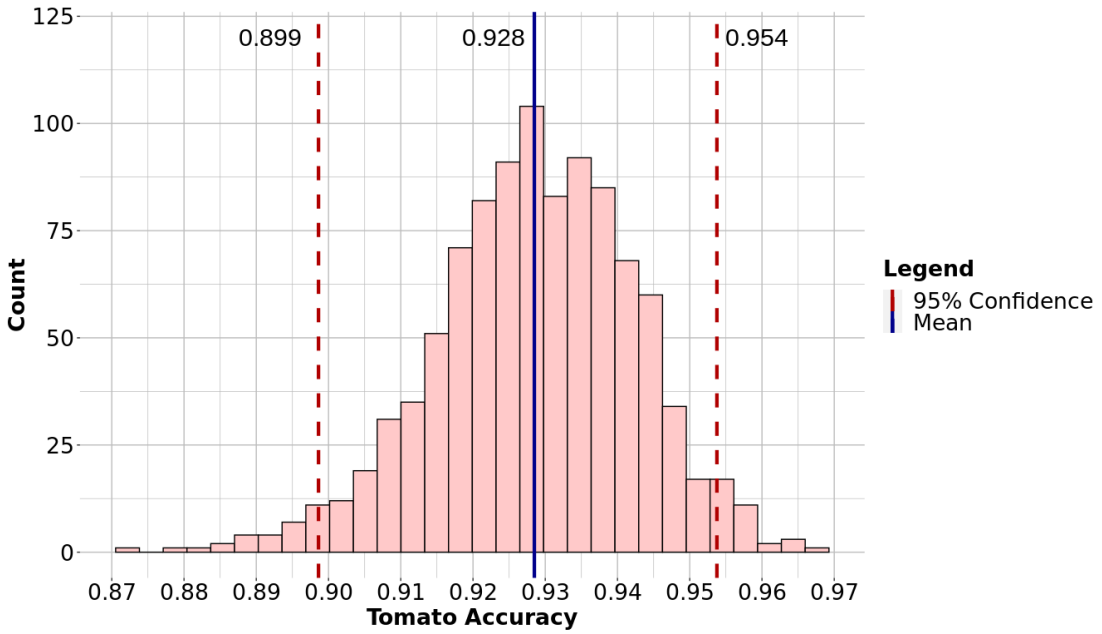


**Figure B.11 :** Bootstrapping histogram with average accuracy and confidence intervals for the 12th classification case.

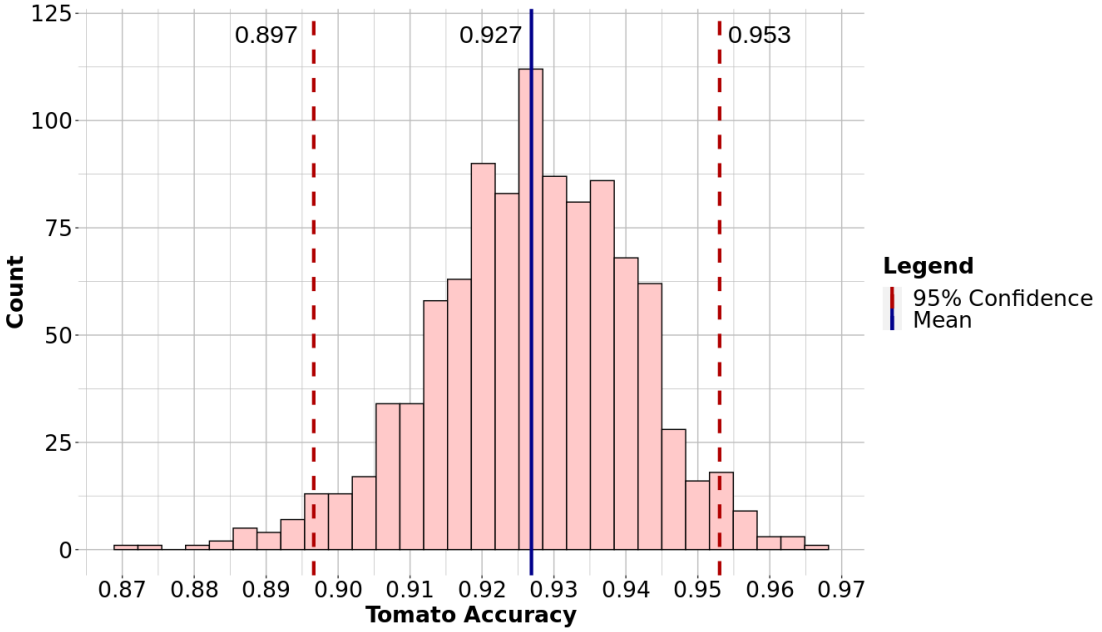


**Figure B.12 :** Bootstrapping histogram with average accuracy and confidence intervals for the 13th classification case.

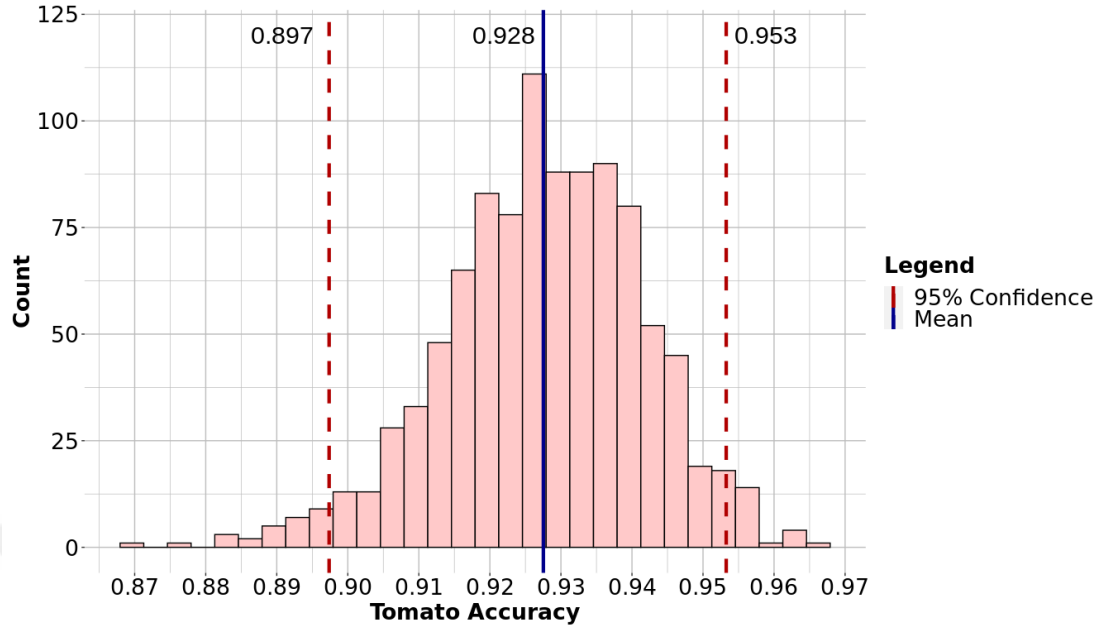


**Figure B.13 :** Bootstrapping histogram with average accuracy and confidence intervals for the 14th classification case.

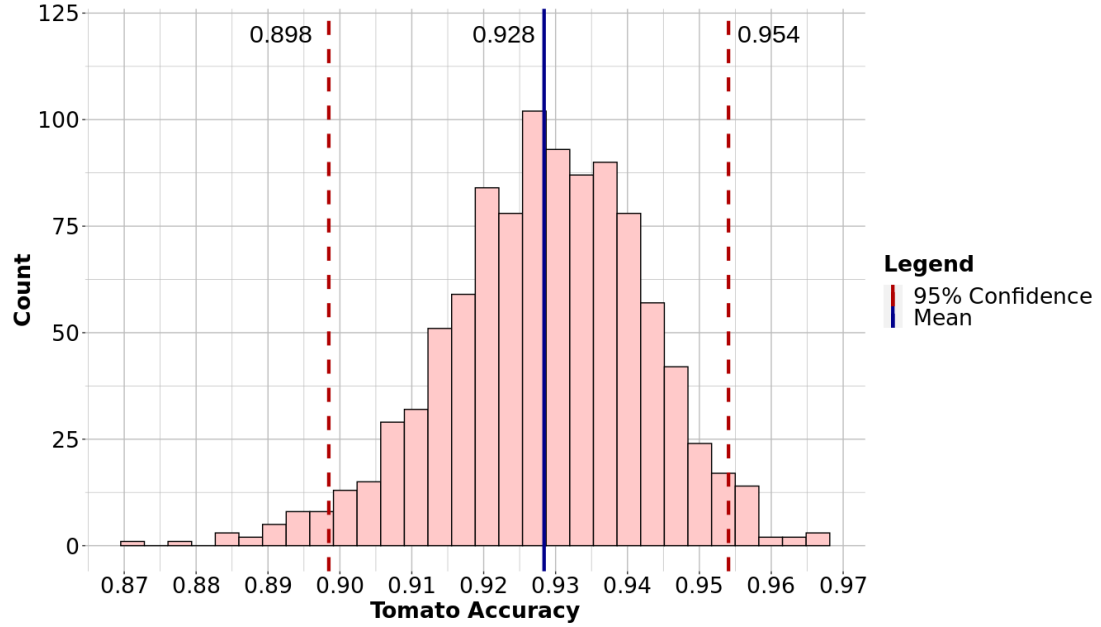


**Figure B.14 :** Bootstrapping histogram with average accuracy and confidence intervals for the 16th classification case.

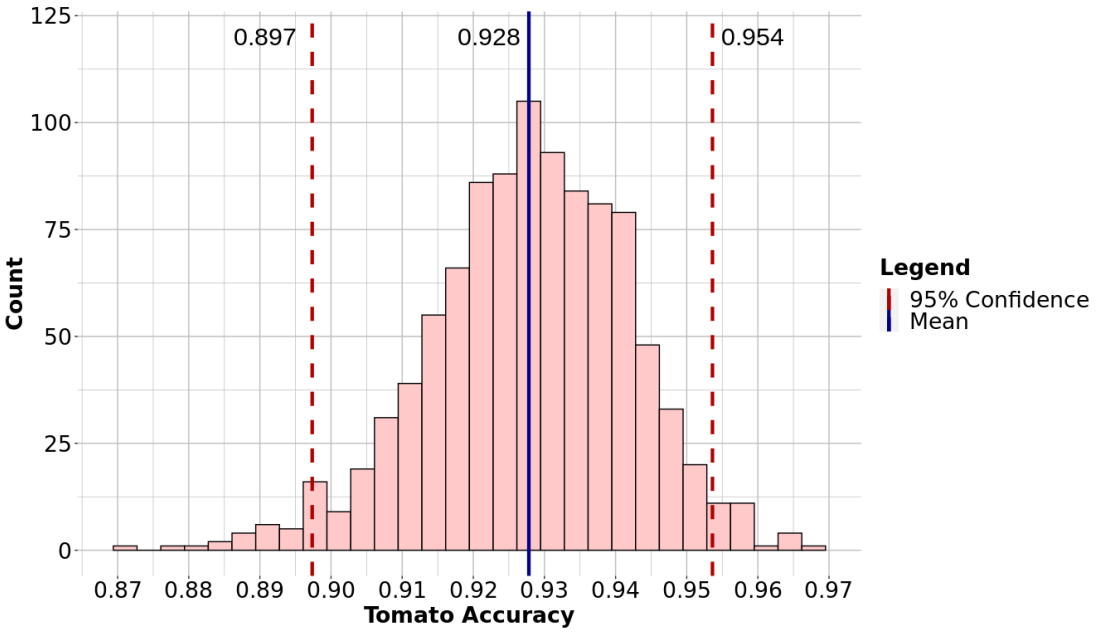


**Figure B.15 :** Bootstrapping histogram with average accuracy and confidence intervals for the 17th classification case.

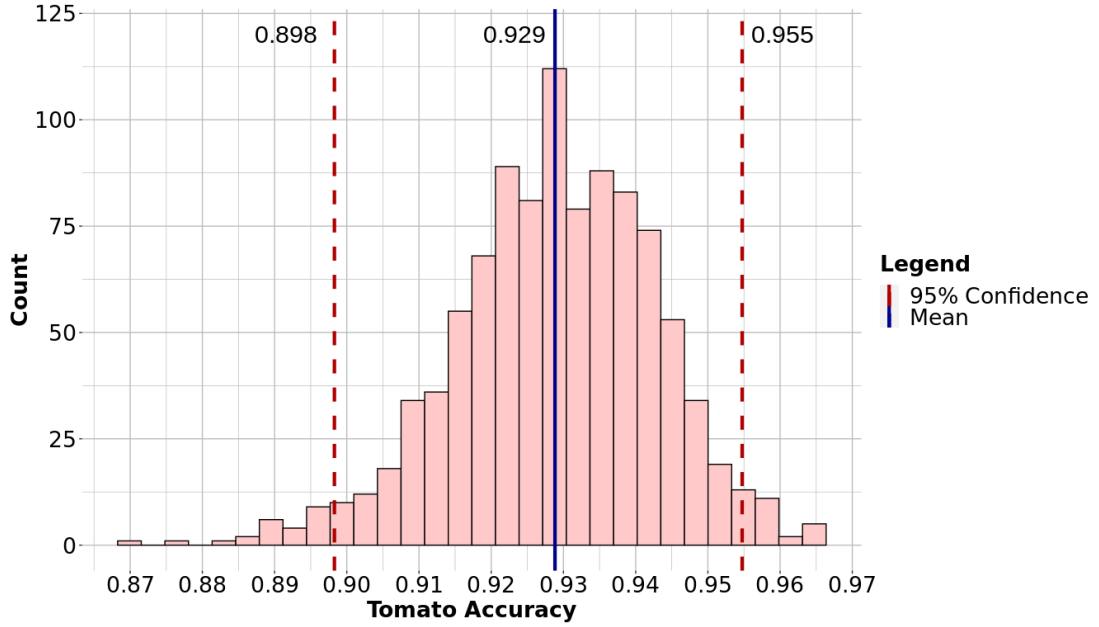


**Figure B.16 :** Bootstrapping histogram with average accuracy and confidence intervals for the 18th classification case.

## APPENDIX C

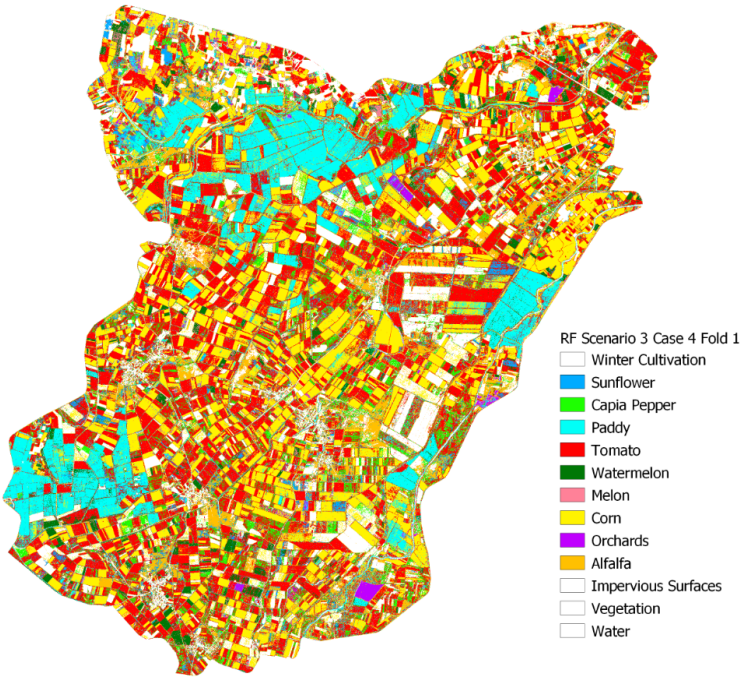


**Figure C.1 :** Thematic map of RF classification scenario 3, case 4, fold 1.

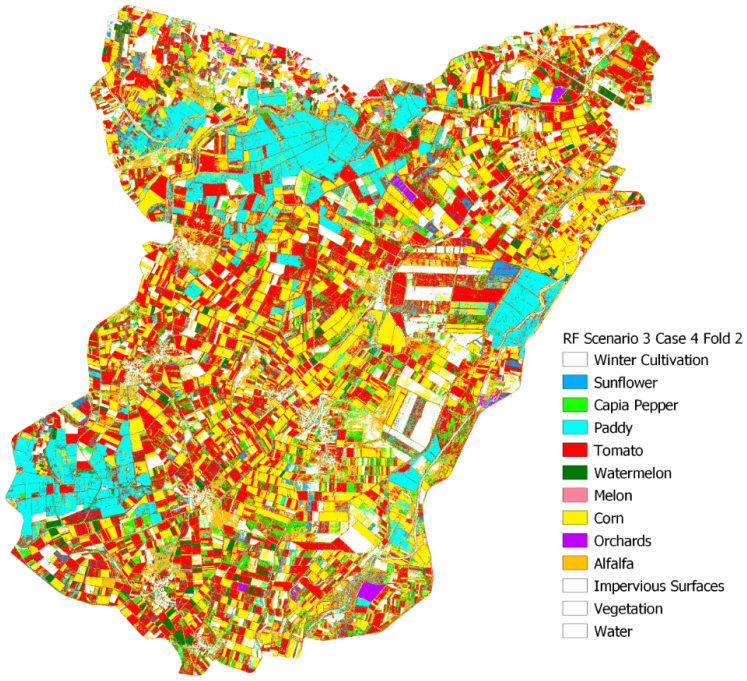


**Figure C.2 :** Thematic map of RF classification scenario 3, case 4, fold 2.

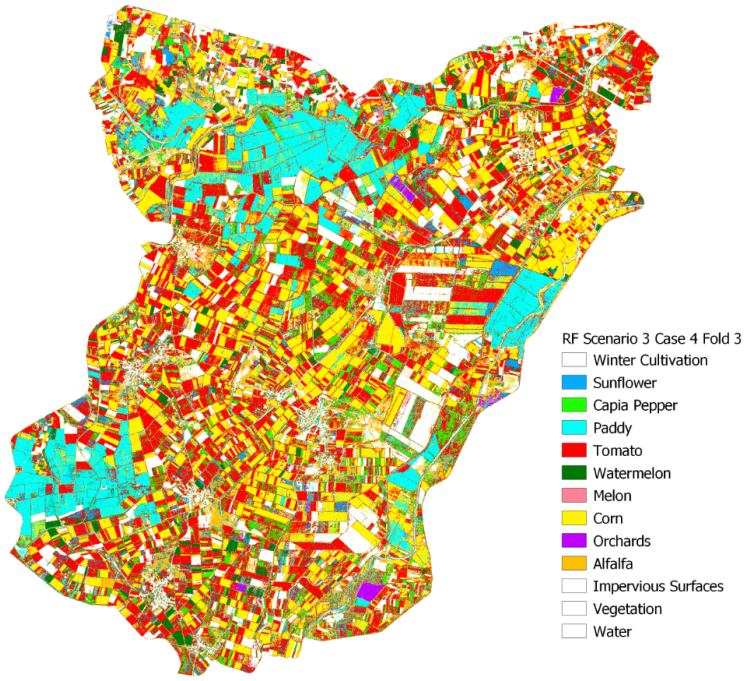


**Figure C.3 :** Thematic map of RF classification scenario 3, case 4, fold 3.

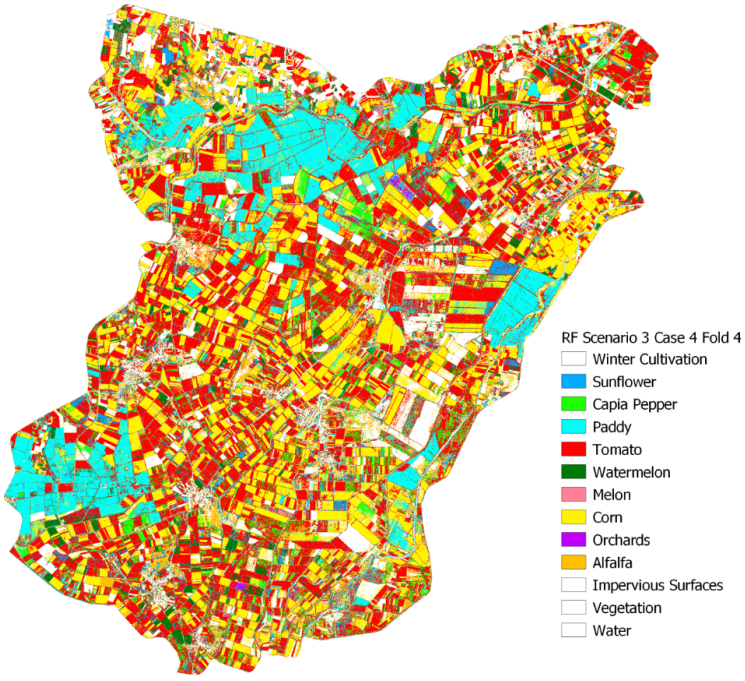


**Figure C.4 :** Thematic map of RF classification scenario 3, case 4, fold 4.

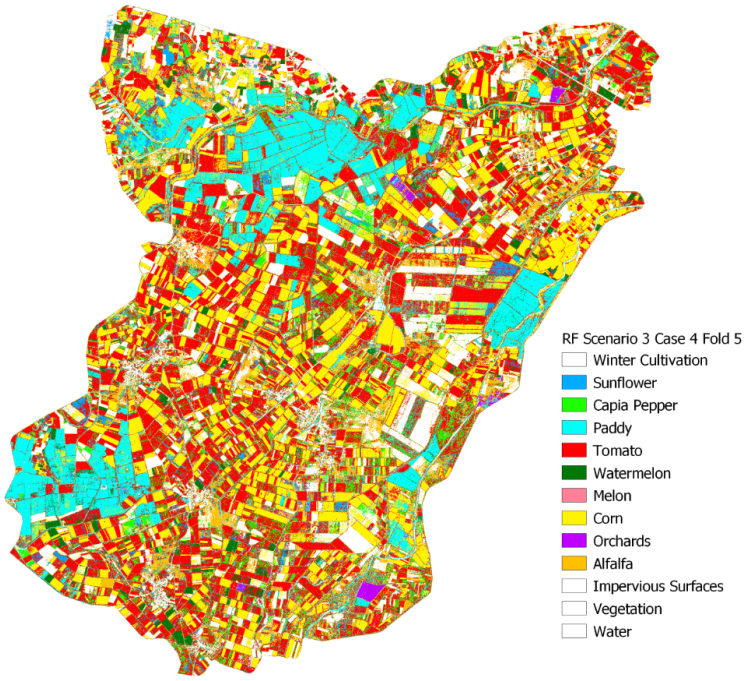


**Figure C.5 :** Thematic map of RF classification scenario 3, case 4, fold 5.

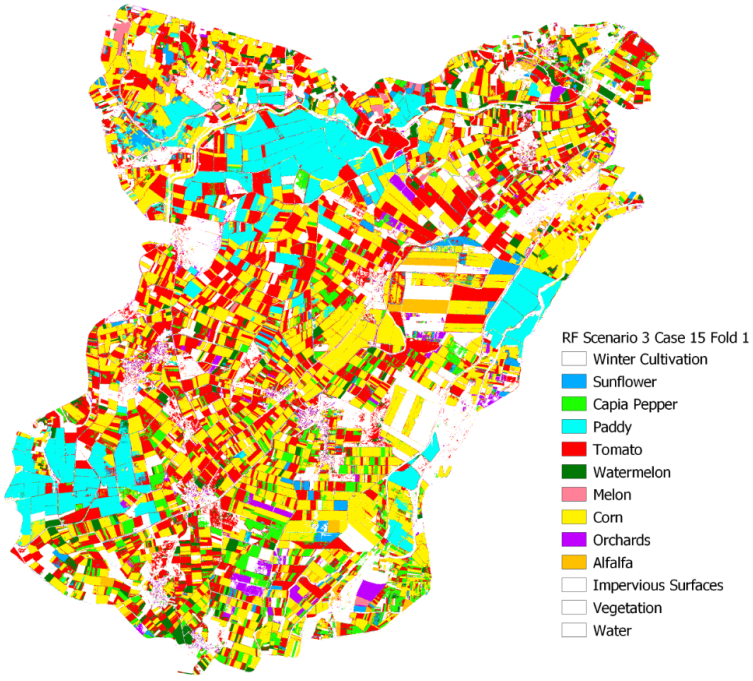


**Figure C.6 :** Thematic map of RF classification scenario 3, case 15, fold 1.

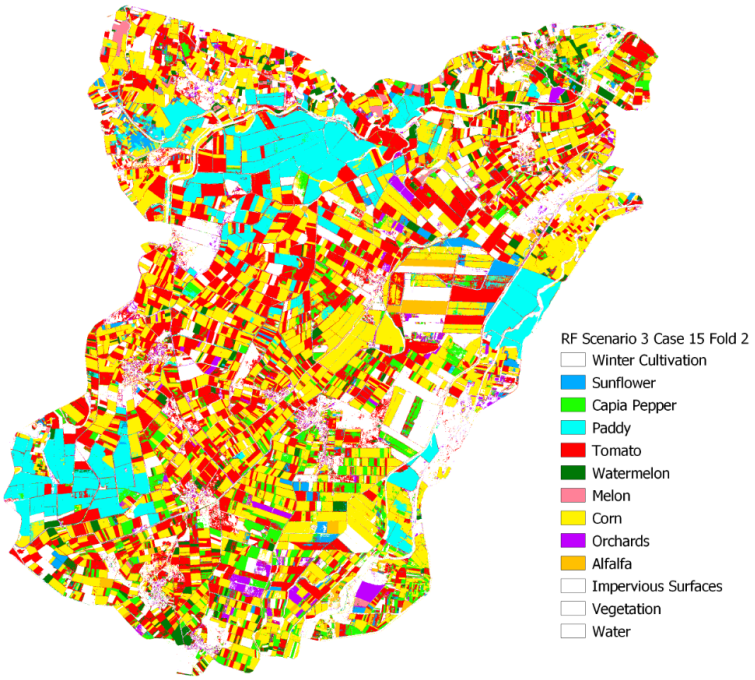


**Figure C.7 :** Thematic map of RF classification scenario 3, case 15, fold 2.

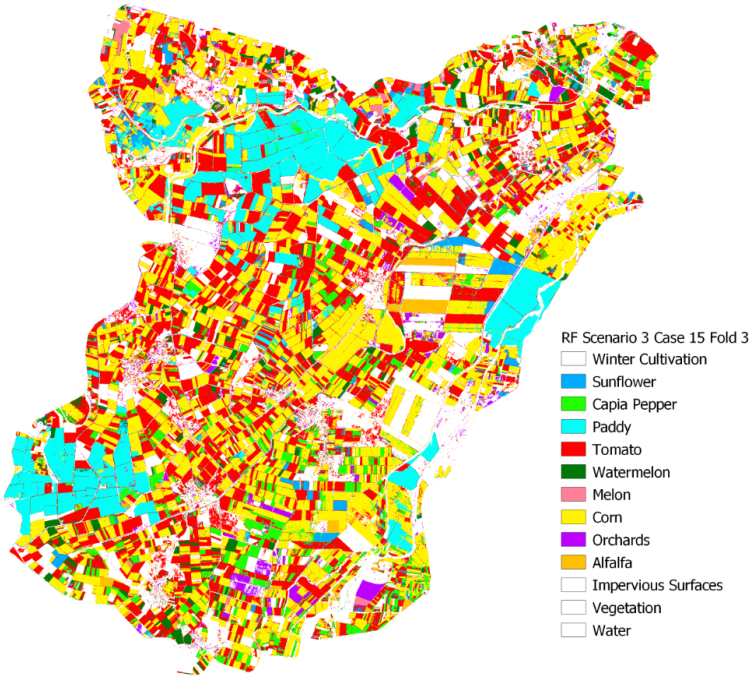


**Figure C.8 :** Thematic map of RF classification scenario 3, case 15 , fold 3.

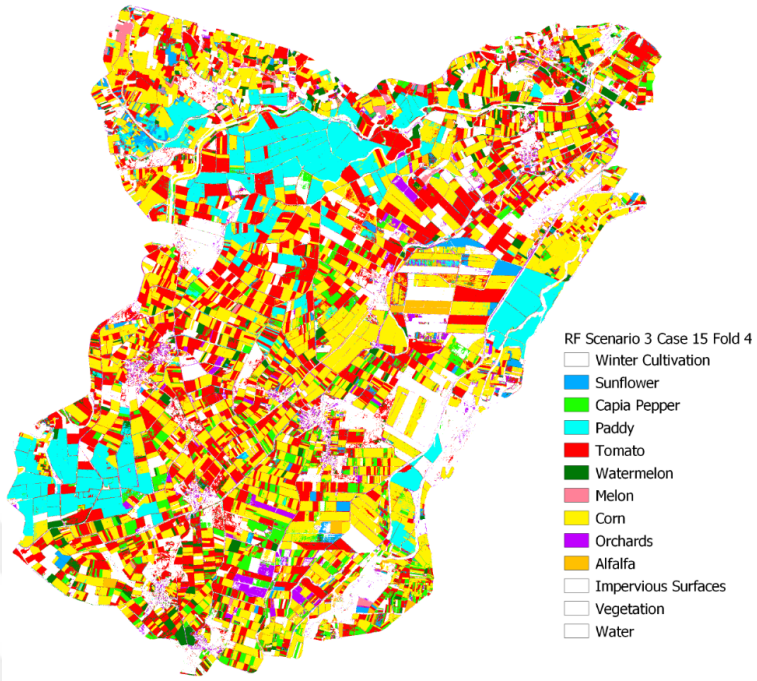


**Figure C.9 :** Thematic map of RF classification scenario 3, case 15, fold 4.

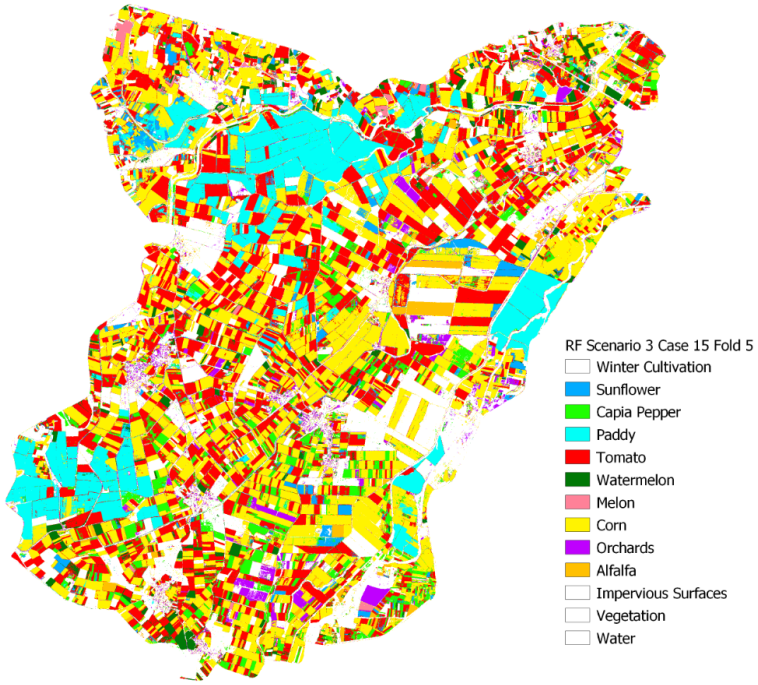


**Figure C.10 :** Thematic map of RF classification scenario 3, case 15, fold 5.

**CURRICULUM VITAE**

**Name Surname** : Betül Şallı

**Place and Date of Birth** : İstanbul, 03.03.1994

**E-Mail** : sallibetul@gmail.com

**EDUCATION** :

- **B.Sc.** : 2017, Istanbul Technical University, Faculty of Civil Engineering, Geomatics Engineering Department

**PROFESSIONAL EXPERIENCE AND REWARDS:**

- 2019 Doktar Digital Agricultural Solutions
- 2017-2019 Istanbul Technical University Center for Satellite Communications and Remote Sensing (ITU CSCRS)

**PUBLICATIONS, PRESENTATIONS AND PATENTS ON THE THESIS:**

- **Bahşi, K., Şallı, B., Kılıç, D., Sertel, E.** 2019. Estimation of emissions from crop residue burning using remote sensing data, *International Journal of Global Warming,* 19(1/2), 94–105.

- **Şallı, B., Bahşi, K., Sertel, E.** 2018. Determination of Burned Areas Using Multi-Sensor Satellite Images and Spectral Indices: Bayindir Forest Fire Case. *38th Annual EARSeL Symposium & 3rd Joint EARSeL LULC and NASA LCLUC Workshop*, July 9–12, 2018 Chania, Crete, Greece.

- **Sertel, E., Topaloğlu, R.H., Şallı, B., Yay Algan, I., Aksu, G.A.** 2018. Comparison of Landscape Metrics for Three Different Level Land Cover/Land Use Maps, *ISPRS Int. J. Geo-Inf,* 7, 408.

- **Şallı, B., Karadal, G., Topaloğlu, R. H., Sertel, E., Musaoğlu, N.** 2017. Comparison of Different Spectral Indices to Identify Vegetation Cover Using Landsat-8 OLI and Sentinel-2A MSI Data. *International Symposium on GIS Applications in Geography Geosciences*, October 18–21, 2018 Çanakkale, Turkey.

- **Karadal, G., Şallı, B., Topaloğlu, R. H., Sertel, E., Musaoğlu, N.** 2017. Spatio-Temporal Evaluation Of Built-Up Areas In Mediterranean Coastline Using Satellite Images. *MESAEP*, October 3–6, 2017 Rome, Italy.